MSc-thesis, Utrecht University, department Earth Sciences

Analysis of Rare Earth Element concentrations in barite ($BaSO_4$).

Determination of the environment of formation of Archean barites by Rare Earth Element fractionation measurements.

Korien Oostingh
MSc-student Petrology, Utrecht University
3021513

Supervisors: Paul Mason and Desiree Roerdink

September 2011

- Abstract -

Temperature and redox conditions during barite precipitation potentially provide information about levels of oxygen in the Archean (3.8-2.5 Ga) environment and the presence of early microbial life. Rare Earth Element (REE) abundances, especially the preservation of Ce and Eu anomalies, can provide this information, but little is known due to analytical difficulties in measuring trace elements in barite. In situ determination of REE in barite by Laser Ablation Inductively Coupled Plasma Mass Spectrometry (LA-ICP-MS) is a fast method to obtain these element abundances, but requires calibration to test for accuracy and precision. Here, we develop an Ion Exchange Chromatography technique to measure REE in solutions of dissolved barite while avoiding spectral interferences, such as $^{137}Ba^{16}O$ on ^{153}Eu. Barite was fused in a 1:10 ratio with Na_2CO_3 and subsequently dissolved in 6N HCl. More than 99% Of the Ba-ions were removed from this solution after Ion Exchange Chromatography using 2(ethylhexyl)-orthophosporic acid as binding fluid. ICP-MS analyses of solutions from Archean and Paleozoic barites from high- and low-temperature environments showed that REE concentrations are very low. Both solution and in situ techniques suffered from a number of problems including: 1) PrO interferences on Gd, 2) Ce contamination in Na_2CO_3 flux, 3) residula Ba in both methods resulting in Eu interferences, 4) absence of reliable internal and external standards, 5) presence of interfering accessory phases such as monazite and 6) poor detection limits. However, comparison of REE abundances with the geological settings of the analyzed deposits suggests that measured Ce and Eu anomalies are consistent with the temperature and redox conditions during barite formation. Data corresponds with earlier data on REE fractionation in barite by Guichard (1979) and Barrett et al (1990) with respect to REE abundances but differs with this earlier data with respect to Eu and Ce anomalies. Interpretation of the results in terms of possible microbial versus non-microbial processes and the oxidation state of the Archean environment is difficult and requires the improvement of the methods to overcome remaining questions on the factors controlling REE partitioning in barite.

I. Index.

1.1 Introduction.

Rare Earth Element (REE) abundances and distributions in barite ($BaSO_4$) can potentially serve as indicators of the physio-chemical environment of deposition in both Recent and Ancient Earth's systems. Barite is thought to serve as an ideal mineral for REE pattern studies since it is formed in a variety of environments (Hanor, 2000) such as hydrothermal vent systems, as stockwork vein filling in continental rocks and in the marine realm. Most existing research is focused towards barite precipitation in seawater. Barite directly precipitates from seawater; reflecting the REE seawater distribution and is thought to be highly insoluble and therefore less affected by alteration (Martin et al, 1995). REEs have already been extensively used as indicators of the conditions during precipitation of a variety of minerals because of the distinct differences between REE patterns of seawater and marine sediments and hydrothermal precipitates (e.g. Piper, 1974; Guichard et al, 1979; Elderfield, 1988 and Michard et al, 1989). Especially the capability of Eu^{3+} and Ce^{3+} to be reduced respectively oxidized in fluids resulting in anomalies in chemical precipitates such as barite are of importance in determining the redox state, the temperature, the f_{O2} and the pH of a system (e.g. Sverjensky, 1983; Elderfield et al; 1988; Lottermoser et al; 1991; Bau; 1991 and Bau and Moller; 1991). Knowledge of the temperature of formation is of importance while interpreting stable isotope data of Archean barites to distinguish between microbial (up to ~100°C and non-microbial (>100°C) redox processes. These stable isotope data are used by other workers to draw conclusions on early life in the presence of sulfur reducing bacteria as early as 3.47Ga (Shen et al, 2001; Ueno et al, 2008) and the evolution of Earth's atmosphere by microbial anaerobe methane oxidation (Ueno et al, 2006; Riedinger et al; 2005).

However, only limited research has been done towards the REE distribution in barite (Guichard et al, 1979; Barrett et al, 1990) probably because of the lack of knowledge of the factors controlling the REE partitioning in barite and the difficulties arising when trying to analyze REE concentrations. Because barite is very insoluble and ICP-MS REE analyses suffer from interferences of - amongst others - BaO on ^{153}Eu (Dulski, 1994), either the costly and slow Neutron Activation Analysis is performed (Guichard et al, 1979) or potentailly unreliable corrections are done to overcome the interference problems (Barrett et al, 1990). The results from these studies as well as preliminary research in our group (unpublished results) indicate (La/Lu)>1 patterns in barite, REE depletion and a +ve Eu anomaly in hydrothermally formed barite (Barrett et al, 1990) and the presence of a –ve Eu anomaly but the unexpected absence of a –ve Ce anomaly in marine barites (Guichard, 1979).

In this work, I asses the use of LA-ICP-MS analysis on in situ rock samples as a new technique for measuring REE abundances in barite in order to draw conclusions on the environment of formation. This was done by measuring both non-Archean barite with known environment of formation and comparing the REE patterns with measurements of Archean barites with less detailed information on environment of formation. The LA-ICP-MS technique was qualitatively checked by ICP-MS analysis on Ba-REE solutions of the same non-Archean and Archean barite samples. Therefore, a technique was developed together with the Bau group at Jacobs University Bremen to totally dissolve barite and perform an Ion Exchange Chromatography method on the obtained solutions to separate the Ba^{2+} from the REE such that BaO interferences during ICP-MS analysis are overcome.

The following sections will provide some background information on barite and REEs as well as more detailed information on oceanic and atmospheric conditions during the Archean.

1.2 Barite.

The mineral barite ($BaSO_4$) is the end-member of the barite ($BaSO_4$)-celestine ($SrSO_4$) solid solution series. In this report, the term barite will be used to refer to not only the stochiometric endmember, but also to (Ba, Sr)SO_4 solid solutions dominated by Ba. The mineral barite occurs in a very diverse range of sedimentary, metamorphic and igneous geological environments and is deposited as bedded barite deposits between 3.6Ga to 3.2Ga and from 2.4Ga to present with increasing abundance (Huston and Logan, 2004) at a wide range of pressures and temperatures (*Figure 1.1*) (Hanor, 2000). This wide range of deposition periods makes it a good mineral to use for comparison between present-day deposits with known characteristics and Early Earth deposits of which the characteristics are unknown.

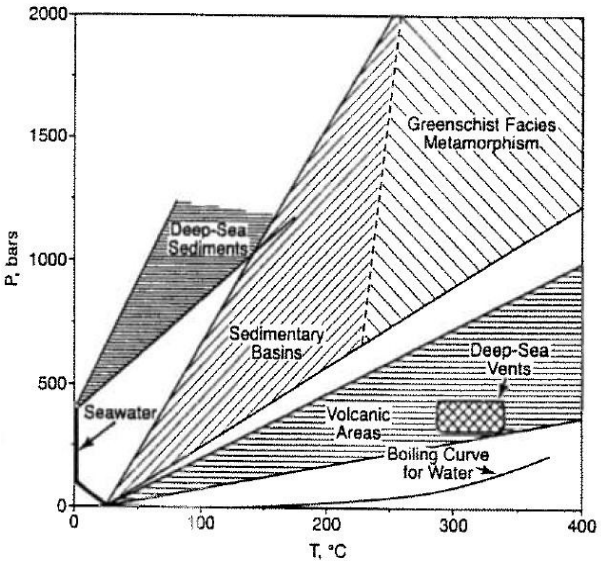

Figure 1.1. Pressure and temperature conditions for shallow crustal and marine environments in which barite has been deposited (Hanor, 2000).

1.2.1. Crystallography.

Both barite as well as celestine are orthorhombic, dipyramidal and have the space group *Pnma* (Hanor, 2000). The structure of barite consists of SO_4^{2-}-tetrahedra that are bonded laterally through Ba^{2+} cations. Each Ba^{2+} cation is in 12-fold coordination with the oxygens in the sulfate tetrahedral. Barite crystals are mainly tabular or sometimes prismatic to the *a* and *b* crystal axes. A variety of textures result either from intergrowth of crystals or from concretion processes. Examples are intergrown rosettes or platy aggregates and fibrous or granular and cleavable masses from concretion (Nesse, 2004). Barite undergoes a transition at 1148°C to a monoclinic structure that melts at 1580°C (Hanor, 2000).

1.2.2. Sources of Ba and S.

Both barium (Ba) as well as sulfur (S) are widely distributed and relatively abundant (Ba = 250ppm and S = 310ppm) in the Earth's crust (Hanor, 2000). Ba is present in most igneous and siliciclastic rocks but the majority of the Earth's crustal Ba can be found as solid solution for K in K-bearing minerals such as K-feldspars and K-micas (biotite)(Hanor, 2000). In igneous rocks, the abundance of Ba increases with Si (and hence, K and Ca) content (Hanor, 2000). The Ba concentration in seawater varies significantly since it is fast removed from the water column. A range of concentrations in Recent seawater is 5-20µg/kg seawater in open ocean waters, while the concentration is much higher (60µg/kg) in marine anoxic basins. Sulfate is the second most abundant anion in Recent seawater with an average concentration of 2.712mg/kg. In marine anoxic basins, sulfate can be reduced to sulfide. A variety of valance states of sulfur (sulfide - S^{2-}, sulfate - SO_4^{2-} and native sulfur - S^0) occur at the Earth's crust that are largely controlled by the redox state in the marine or hydrothermal water considered (Hanor, 2000). Under reducing conditions sulfur mainly exists as H_2S or metal sulfides while at oxidizing conditions sulfur mainly exists as dissolved sulfate and the alkaline earth sulfates gypsum, anhydrite, celestine and barite (Hanor, 2000). The geochemical sulfur cycle has evolved significantly over time. The Early Earth atmosphere consisted of CO_2, N_2 and CH_4 and limited sulfide concentrations in the oceans, while the modern-day atmosphere is characterized by the existence of free oxygen which first appearance 2.5Ga made sulfate reduction and associated isotope fractionation possible (Hanor, 2000)(Canfield et al, 2000). The evolution of the atmosphere is further discussed in the section 'Archean atmosphere and ocean compositions' further in this chapter.

1.2.3. Solubility.

Barite solubility at or below the Earth's surface is not only dependent on pressure and temperature but also on the presence of other dissolved substances in solution, ion exchange with clay minerals and other materials and the possible instability of barite under sulfate-reducing conditions (Blount, 1977). The Ba^{2+}-ion has a high ionic potential and can be readily accommodated in aqueous solutions as hydrated divalent cations (Hanor, 2000). The SO_4^{2-} ionic complex is also very soluble as a hydrated ionic species (Hanor, 2000). However, the reaction between dissolved Ba^{2+} and SO_4^{2-} produces such an insoluble mineral that natural waters can be found either with significant amounts of Ba^{2+} or with significant amounts of SO_4^{2-} but not with both (Hanor, 2000). In ideal aqueous solutions, the mass action relation for the dissolution of barite is given by:

$$BaSO_4(s) \Leftrightarrow Ba^{2+}(aq) + SO_4{}^{2-}(aq) \quad 1)$$

for which the equilibrium constant K is given as:

$$K_{BaSo_4} = \frac{(a_{Ba^{2+}}) * (a_{SO_4{}^{2-}})}{(a_{BaSO_4})} \quad 2)$$

(Hanor, 2000). It was found by Bowers et al (1984) that at any fixed temperature, the aqueous solubility of barite will increase with increasing pressure, while at a fixed pressure, there is a solubility increase from 0-100°C and then a progressively decrease in solubility for T>100°C (Hanor, 2000)(Bowers et al, 1984). The values of the logK for low temperatures range from -10.49 (P=saturation vapor pressure, T=0°C) to -9.12 (P=2.0kbar, T=0°) while for higher temperatures the range is from -15.43 (P=0.5kbar, T=400°C) to -10.79 (P=2.0kbar, T=400°C)(Hanor, 2000). However, in natural environments sulfate will show non-ideal behavior in solution even at low ionic strengths (Hanor, 2000). Furthermore, microbial sulfate reduction will enhance the dissolution of barite in the marine column in that this process depletes the seawater in SO_4^{2-} such that porewaters get undersaturated w.r.t. barite so that it will dissolve (Jørgensen and Kasten, 2006). Extensive work towards the solubility of end-member barite in non-ideal aqueous solutions was performed by Blount (1977)(Hanor, 2000). Blount (1977) determined the impact of increasing salinity on the solubility of barite in a variety of electrolyte solutions at different T and found that there is a significant increase in the solubility of barite by over an order of magnitude with increasing concentration of NaCl from 0-6M (*Figure 1.2.*)(Blount, 1977)(Hanor, 2000). This is mainly due to the strongly non-ideal behavior of the sulfate ion in concentrated electrolyte solutions (Hanor, 2000). According to Blount (1977) barite solubility in non-ideal aqueous solutions is on the order of 10^{-5} moles $BaSO_4$ per kilogram solvent.

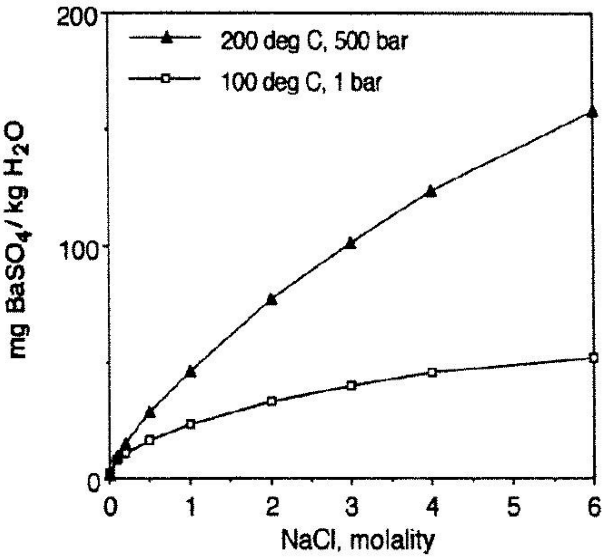

Figure 1.2. Barite solubility dependence on salinity as investigated by Blount (1977) (Hanor, 2000).

1.2.4. Environments of Formation.

Barite is often subdivided into 'continental' and 'marine' barite, according to the research by Goldberg (1969) who states that the isotopic analysis of sulfur and the ratio between uranium and thorium are diagnostic to distinguish between the two types. However, according to Hanor (2000) this subdivision is highly questionable, since Goldberg (1969) only takes the present location of the barites into account and neglects the sources of Ba and S. In this research, neither the terms 'continental' or 'marine' will be used to specify a certain barite sample, but the subdivision by Hanor (2000) is used which is defined as following (numbers 1-4):

1) Barite in submarine volcanic hydrothermal systems ("hydrothermal barite")

Barite formed by this process results from convective circulation of fluids in the oceanic crust (Hanor, 2000). The fluids are discharged upwards by extensional faults while leaching Ba from a variety of source rocks after which they become mixed with sulfate-rich seawater when ascending to the seafloor (Hanor, 2000). Two different deposits result from this process:

A) Volcanic-Hosted Massive Sulfate (VHMS) deposits that result from high heat (Hanor, 2000) associated with emplacement of magma but can be unrelated to sedimentary processes.
B) Sedimentary-Exhalative (SEDEX) deposits of barite that formed by ascending barium -rich fluids venting into the marine environment (Hanor, 2000) at elevated temperatures resulting in the precipitation of stratiform ore.

The VHMS-deposits are characterized by bulbous to tabular stratiform accumulations of massive base-metals such as pyrite and Zn, Cu and Pb sulfides (Hanor, 2000). A modern analogue to VHMS deposits are black smoker chimneys that are associated with extensional or rifted terrains or with seamounts which are all characterized by high heat flow (Hanor, 2000). SEDEX-deposits normally are to a lesser extent associated with the presence of base-metals and rather form in shallow-water sediments deposited during the stage of thermal subsidence following active extension (Hanor, 2000). SEDEX barite deposits are often spatially associated with syn-sedimentary faults and are characterized by the presence of lenses and massive laminated structures (*Figure 1.3.*)(Hanor, 2000).

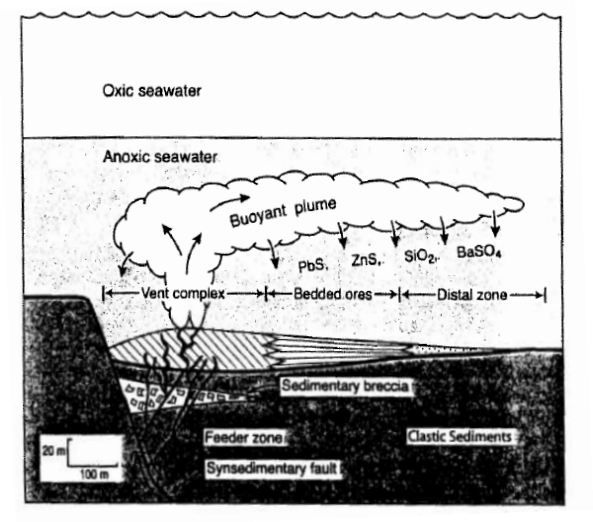

Figure 1.3. Schematic diagram showing the principal characteristics of a SEDEX sulfide-barite deposit at the time of deposition (Hanor, 2000).

2) Cenozoic pelagic barite and dispersed barite in deep-sea sediments

Pelagic barite is commonly used for barite produced in the shallow part of the water column of the open ocean, while dispersed barite in deep-sea sediments may include pelagic barite, barite precipitated at the seafloor and particulate barite occurring as suspension in the oceans derived from distant hydrothermal sources (Hanor, 2000). Although widely studied because of the capability to serve as a palaeo-proxy, the modes of precipitation of pelagic barite are still debated (Hanor, 2000). A number of mechanisms for precipitation and deposition are proposed of which the precipitation in sulfate-enriched environments seems most likely the main process. After precipitation, pelagic barite consists of bio-aggregates without crystalline habit in the upper 10-20m water column and as bio-aggregates with crystalline habit in the lower water column (Hanor, 2000). At water depths below a few 100 meters, barite is found to be present as free discrete particles settling much slower than the aggregates (Hanor, 2000). According to Church (1979) there are 3 types of deep-sea sediments that have been found to contain barite:

A) deep-sea sediments with abundant calcareous and siliceous biological debris
B) deep-sea sediments with abundant Mn and Fe phases in both nodular and dispersed forms
C) deep-sea sediments with abundant altered volcanic debris with the minerals montmorillonite, palygorskite and clinoptilolite (Church, 1979).

3) Epigenetic barite deposits and evaporites

The barite that is classified to this sub-group is distinctive from the earlier barites in that sulfur is not derived from a direct seawater source but

from marine evaporites and/or buried evaporative marine waters while the other elements are derived from surrounding rocks (Hanor, 2000) and that it is thus a later-stage geological feature. This group comprises both carbonate-hosted barite deposits, barite in continental rift systems, barite in late-stage thrust belts (stockwork vein barite) and dispersed cements and nodules of barite in evaporate sequences (Hanor, 2000).

The carbonate-hosted deposits are characteristic for Paleozoic development of deposits associated with biochemical continental margins and epicontinental platform carbonates (Hanor, 2000). Typical ore deposits are:

A) Mississippi Valley Type ore deposits which are mainly epigenetic cavity fill and replacements by galena, sphalerite, fluorite and barite in cemented platform limestones and dolomites (Hanor, 2000).
B) Irish Type ore deposits which are Pb-Zn-Ba deposits that form in an extensional carbonate environment resulting from the mixing of a hot (120-180°C) ore fluid with low-T sulfur-rich fluid (Hanor, 2000).

Further away from continental margins or active marine basins in a continental rift setting, barites are deposited in veins (Hanor, 2000). These veins are often deposited epigenetic rather than in a syndepositional marine setting (Hanor, 2000). Fluid inclusion studies from veins in Mesozoic rift basins in the USA show that mineralization was deposited from moderately saline brines (10-16wt% NaCl) with a temperature range of 100-250°C (Hanor, 2000).

Especially in Europe, much of the barite is found as vein deposits in orogenic belts (Hanor, 2000). It is thought - at least for the Southern Alps - that formation of barite is attributed to the interaction of Ba-rich ascending solutions through sulfate-rich surrounding evaporitic rocks.

4) Barite of continental igneous and igneous-hydrothermal origin

Another example of barite that is formed from a non-seawater sulfate source is barite that is common in a wide variety of metal deposits that are associated with continental igneous activity (Hanor, 2000). Barite can either be formed magmatic by late crystallization of K-feldspar from a Ba-enriched melt forming carbonatites or by hydrothermal activity forming small barite deposits in veins associated with porphyry Cu and Cu-Mo deposits (Hanor, 2000).

1.2.5. Archean barite.

The first appearances of barite in the geologic record is probably the synsedimentary mound deposits on the East Pilbara craton which were deposited on the seafloor 3.5Ga ago (Nijman et al, 1998). These barites fall within the subcategory Submarine Volcanic Hydrothermal and formed during continuous venting of a hydrothermal system analogue to white smokers (Huston and Logan, 2004) after the peak of high-T discharge and where seawater contained abundant sulfate (Hanor, 2000).

The sequence in the East Pilbara block is thought to be deposited within a shallow-water evaporative lagoon when submarine fluids rich in Ba, Si and S were boiling or degassing and mixing with the overlying water column when oxidation of sulfide to sulfates caused precipitation of barite (Buick and Dunlop, 1990; Nijman et al, 1998). A sample from this barite deposit (Dresser barite) will be evaluated in this research.

Similarly massive quantities of barite can also be found in the Early Archean portions of the Precambrian shields of India, Canada, Russia and South-Africa (Hanor, 2000). The latter deposit will be discussed extensively in the sample description part of this study.

1.3 Rare Earth Elements.

REEs are part of the so-called trace elements which most often only constitute a small fraction of the geological system considered (White, 2001). Although often very minor in abundance trace elements can provide a lot of geological and geochemical information due to several reasons. First, the variation of trace elemental concentrations is much larger than that in major element concentrations (White, 2001). Second, there are always more trace elements with unique chemical properties in a system than major elements (White, 2001). Third, the range in behavior of trace elements is large and altogether they are more sensitive to processes that major elements are insensitive of (White, 2001). Therefore, the partitioning of REEs in barite is used in this research to put constraints on the environments of deposition. The goal is to answer questions such as: how can we accurately measure REEs in barite? or: what are the controls on the REE partitioning in barite?

In this part of the Introduction, some information will be provided for REEs on behalf of their characteristics and their behavior in the natural environment. Previous studies towards REE partitioning in barite will be briefly discussed at the end of this chapter.

1.3.1. Characteristics.

Rare earth elements can be divided into the lanthanide and the actinide series, of which the first series is the only one considered in this research. The lanthanide REEs are all strongly electropositive (valency state of +3) and have electronegativities of 1.2 or less (White, 2001). As a result, REEs form predominantly strong ionic bonds (White, 2001). At the low oxygen fugacity state of the Earth's surface, Ce can be partly or wholly in the +4 state and Eu can be partly in the +2 state (White, 2001) meaning that these elements can fractionate from the remaining REEs in solution. The REEs are transition metals in which the *s* orbital of the outermost shell is filled before filling of the lower electron shells is complete (White, 2001). For the lanthanides, this means that the *4f* orbitals are being filled such that the configuration of the valance electrons is similar in all REEs which therefore all have the same chemical characteristics/behavior (White, 2001). The ionic radius is thus the characteristic that governs their relative behavior (White, 2001) and a plot of ionic radius versus REE can be found in *figure 1.4*. Their ionic radius also plays a role during incorporation in minerals. Although all REEs are incompatible due to their large radius and high charge, the heavy REEs (HREEs) can relatively easily be incorporated in many common minerals (White, 2001). For example, the heaviest REEs (Gd to Lu) can substitute for Al^{3+} while Eu^{2+} can substitute for Ca^{2+} in plagioclase feldspar (White, 2001). Because REEs are highly insoluble and immobile once incorporated into a mineral, the relative abundances of REE in a rock remain unchanged during metamorphism and weathering (White, 2001).

1.3.2. REE fractionation during mineral precipitation.

Although less is known about REE partitioning and its controls in barite specifically, much research is carried out towards (controls on) REE partitioning in other minerals derived from aqueous solutions. The two main controlling factors will be briefly discussed in this part, while an attempt is made to clarify the controls on REE partitioning in barite in the *section 1.3.5.* on "Previous studies towards the REE partition in barite" at the end of this chapter.

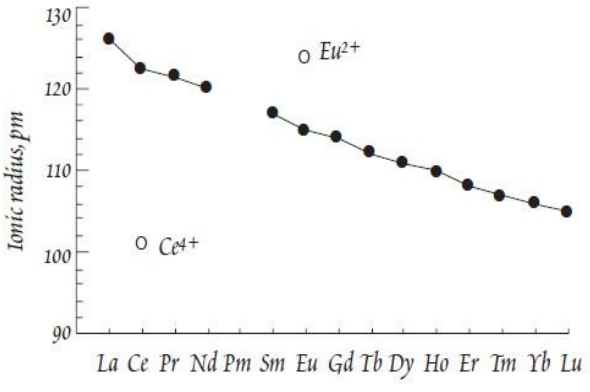

Figure 1.4. Respective ionic radii of the Rare Earth Elements (White, 2001).

Crystallographic control.

Already in 1937, the pioneer in Geochemistry V.M. Goldschmidt suggested that partitioning of REEs in minerals is mainly determined by their charge and ionic radius (Bau, 1996). This behavior, which is characterized as ChArge and RAdius Controlled (CHARAC) behavior by Bau (1996) should produce smooth chondrite normalized REE patterns (except for the Ce and Eu anomalies)(Bau, 1996). Furthermore, CHARAC behavior should also produce chondritic Y/Ho values since these elements are geochemical twins and should remain tightly coupled during geological processes (Bau and Dulski, 1999). These values are 27.7±2.7 (Bau and Dulski, 1999) for the weight-ratio and 52 for the molar ratio in most common igneous rocks and epiclastic sediments (Bau, 1996). Also Zr/Hf forms a geochemical twin that should remain coupled during geological processes and display a chondritic ratio of 36.6±2.9 (weight-ratio)(Bau and Dulski, 1999). Another indicator for crystallographic (CHARAC) control on the partitioning of REEs in minerals is the linear dependence of lnD versus $(r_{REE} - r_{cation})^2$, where D is the distribution coefficient and r is the ionic radius of the REE and the cation respectively if substitution according to the elastic lattice model is assumed (Morgan and Wandless, 1980).

Complexation control.

Any deviation from these previous indicators means that other parameters than ionic radius and valency have played a major role in partitioning the REEs during mineral precipitation. One of the most important parameters is the composition of the fluid from which the REEs are derived and the formation of aqueous complexes. Typically, aqueous solutions and their precipitates do show non-CHARAC behavior (non-chondritic Y/Ho and Zr/Hf ratios) (Bau, 1996). The fractionation of REEs in these solutions is controlled by the formation of aqueous complexes, which in turn is not only controlled by ionic charge and radius, but also by the electron configuration (Bau, 1996), the type of complexing ligand (Bau, 1996)(Wood, 1990a and 1990b) and by the pH and temperature of the fluid (Wood, 1990a and 1990b). For example, at low temperatures, REEs can become speciated in the form of fluoride and sulfate complexes at acidic pH and in the form of carbonate complexes at acidic to basic pH and with phosphate and hydroxide in low-T natural waters (Wood, 1990a) (Elderfield, 1988). Both chloride and nitrate complexes are negligible in low-T waters, phosphate and fluoride complexes are only important in non-natural environments (acid mine drainage systems etc.) (Wood, 1990a). The bonds that form between the REE^{3+} ions and the complexing cations are predominantly electrostatic in character (Wood, 1990a) and will become stronger with increasing T (Wood, 1990b). The bonds between REY^{3+} and the complexing ligands are considered stronger than the bonds between REY^{2+} or REY^{4+} and the complexing ligand (Wood, 1990b). The higher the ionic charge of the REY, the stronger sorption and complexation processes will be, resulting (in a reducing environment) in $(La/Lu)_{cn}>1$, -ve Eu anomaly during predominant sorption processes and $(La/Lu)_{cn}<1$, +ve Eu anomaly for predominant complexation processes (Bau, 1991)(Bau and Möller, 1991) (Schwinn and Markl, 2005).

However small deviations from the linear relation between logD and $(r_{REE} - r_{cation})^2$ are observed - the 'Lanthanide tetrad effect' (*figure 1.5.*) - this is assumed to have small influence on the speci-

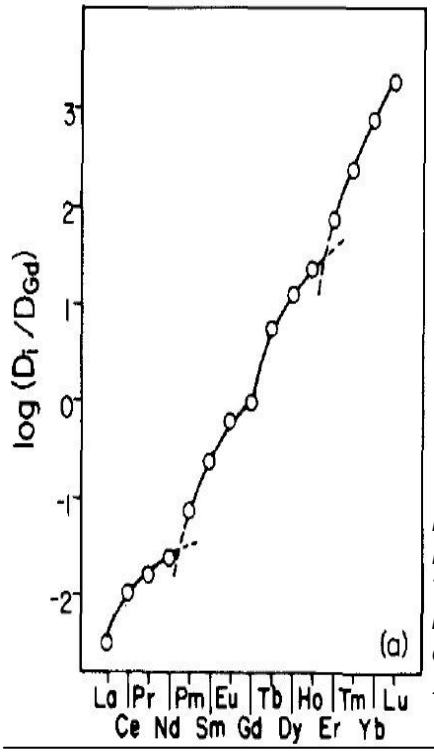

Figure 1.5. The Lanthanide Tetrad effect normalized to Gd (Woods, 1990a).

ation of the different REEs (Wood, 1990a). This lanthanide tetrad effect is probably due to the fact that half-filled or fully filled 4f transition elements are more ionic in character than La and Y which are both more covalent. As a result, La and Y will form higher covalent contributions to predominantly electrostatic bonding between La and Y and a complexing ligand. These differences between electron configuration of the 4f transition elements may result in the lanthanide tetrad effect and anomalies of Gd and Lu, which should be distinguished from anomalies resulting from REE speciation in the water column (Bau, 1999).

At higher temperatures - in hydrothermal systems - the processes responsible for speciation are a little more complex to describe, since the divalent state becomes more important for REEs as Sm, Yb and Eu at elevated T (Wood, 1990b). It is shown that especially Eu^{2+} and minor Yb^{2+} can be found at reasonable pH and at oxygen fugacity when temperature increases (Wood, 1990a). Fluoride complexes are dominant over all others at mildly acidic to mildly basic pH at elevated T, while carbonate as well as sulfate complexes can also play a significant role in speciation when sufficient carbonate or sulfate is available (Wood, 1990b).

1.3.3. Europium anomaly.

As stated before, the reduction of Eu^{3+} to Eu^{2+} is a major indicator for the presence of a low-T versus high-T environment of formation. At temperature >300°C, an increased volatility of Eu species can result in an Eu anomaly, while the development of this anomaly at temperatures ~25°C is unlikely because of the Eu^{3+}/Eu^{2+} redox

Ionic radius (Å) of the REE *in VI-fold coordination*:

$La^{3+} = 1.032 > Eu^{3+} = 0.947 > Lu^{3+} = 0.861$
$Eu^{2+} = 1.17 > La^{3+} = 1.032 > Lu^{3+} = 0.861$

Strength of sorption:

$La^{3+} < Eu^{3+} < Lu^{3+}$
$Eu^{2+} < La^{3+} < Lu^{3+}$

Stability of hydroxide complexes:

$La^{3+} < Eu^{3+} < Lu^{3+}$
$Eu^{2+} < La^{3+} < Lu^{3+}$

Figure 1.6. Impact of change in valency of europium on its characteristics (Bau, 1991)

equilibrium at very low oxygen fugacity (Bau, 1991). However, it is found that in hydrothermal environment the redox equilibrium is also dependent on pH, P, T and chemical composition of the fluid and that the oxygen fugacity at which Eu^{3+} is reduced to Eu^{2+} increases with increasing T (Bau, 1991). This reduction has impact on the partitioning in that Eu^{2+} displays other characteristics than Eu^{3+} (*figure 1.6.*).

Investigation of the impact of alteration/ metasomatism of rocks by hydrothermal fluids (Bau, 1991) leads to two important conclusions: 1) under acidic conditions, the REE pattern of the fluid is controlled by sorption processes, the fluid displays $(La/Lu)_{cn}>1$ (w.r.t. source-rock for REE) and if Eu occurs as Eu^{2+} the REE pattern displays a positive Eu anomaly; 2) in near-neutral to basic conditions, the REE pattern of the fluid is controlled by complexation processes, the fluid displays $(La/Lu)_{cn}<1$ (w.r.t. source-rock for REE)(Bau, 1991). Important in the second case (neutral to basic pH) is that Eu^{3+} tends to become more stable at lower oxygen fugacity due to complexation (Bau, 1991). This means that despite high temperatures, complexation can inhibit the reduction of Eu^{3+} to Eu^{2+}, resulting in an absence of the predicted positive Eu anomaly (Bau, 1991). These conclusions are all valid for alteration of the existing barite or metasomatism during metamorphism, if the fluid/rock ratio was sufficiently high (10^2), meaning that barites that have undergone extensive fluid-dominated alteration do (as indicated by the presence of hydrated phases or by the geology: shear zones present) not provide reliable data for the interpretation of REE patterns (Bau, 1991). This is important to bear in mind when drawing conclusions on the REE patterns of the metamorphosed Archean barite samples investigated in this research.

1.3.4. Cerium anomaly.

While the anomalous behavior of europium is especially pronounced in volcanic rocks and minerals precipitated from high-T fluids, cerium is fractionated in precipitates from low-T fluids such as seawater (Piper, 1974). The REE composition of seawater can be divided into three groups: 1) shelf water, reflecting shale-normalized REE patterns that are identical to

river water, although with lower absolute values, 2) bottom water, which has significantly lower REE concentrations than river water and shelf water and has a REE pattern that exhibits a monotonic increase in concentration with atomic number for the HREE and has a strong negative Ce anomaly, 3) intermediate water, which shows a most strongly fractionation from river waters (Piper, 1974). The increase in concentration for the HREE (the 'v'-shape pattern) is attributed to the greater stability of HREE complexes that form both organic and inorganic in the marine waters (Piper, 1974). The negative Ce anomaly is due to its oxidation from the trivalent state to the highly insoluble quadrivalent state (Piper, 1974). This Ce^{4+} is mainly taken up by Fe-Mn nodules which display a positive Ce anomaly (Piper, 1974). Barite that precipitates as pelagic barite directly from the depleted seawater will therefore show a negative Ce anomaly, corresponding to the shale-normalized seawater REE pattern (Piper, 1974). The increase in the concentration of REE with depth in the marine column might indicate that REEs are removed from the upper water column by lithogenic or biogenic removal (Piper, 1974). It should be noted that REE patterns in marine sediments are best studied when normalized to average shale rather than chondrite, since normalizing to chondrites stresses the differences between shale and chondrite rather than the differences between individual marine phases (Piper, 1974).

1.3.5. Previous studies towards the partitioning of REEs in barite.

The only three articles known to have determined REE patterns in barite are the 1979 article by Guichard et al, the 1995 article by Martin et al and the 1990 article by Barrett et al. All will be briefly summarized in this chapter and main findings and possible errors will be discussed when applicable.

Guichard et al, 1979: REEs in barite, distribution and effects on aqueous partitioning.

Guichard determined REE patterns normalized to chondritic values by neutron activation and column chromatography ion exchange of a variety of barites with deep-sea origin or with non-seawater sulfate source origin (continental barites as referred to in the article by Guichard is a debatable term as seen in the 'Barite' section of the Introduction). All the barites showed a relative $(La/Lu)_{cn}>1$ pattern, while the barites derived from the deep-sea were distinctive from the barites collected from shallower environments or from hydrothermal systems in that they showed a REE enrichment relative to the latter (Guichard, 1979). It was remarkable that the deep-sea sample displayed a negative Eu anomaly, but lacked the expected negative Ce anomaly that is distinctive for seawater (Guichard, 1979). Even positive Eu anomalies were found in the samples derived from reducing sedimentary and metamorphic environments (Guichard, 1979). An overview of the obtained results from Guichard (1979) can be found in *figure 1.7*, but note that the term 'continental barites' is not justified considering the classification of barites as used in this re-

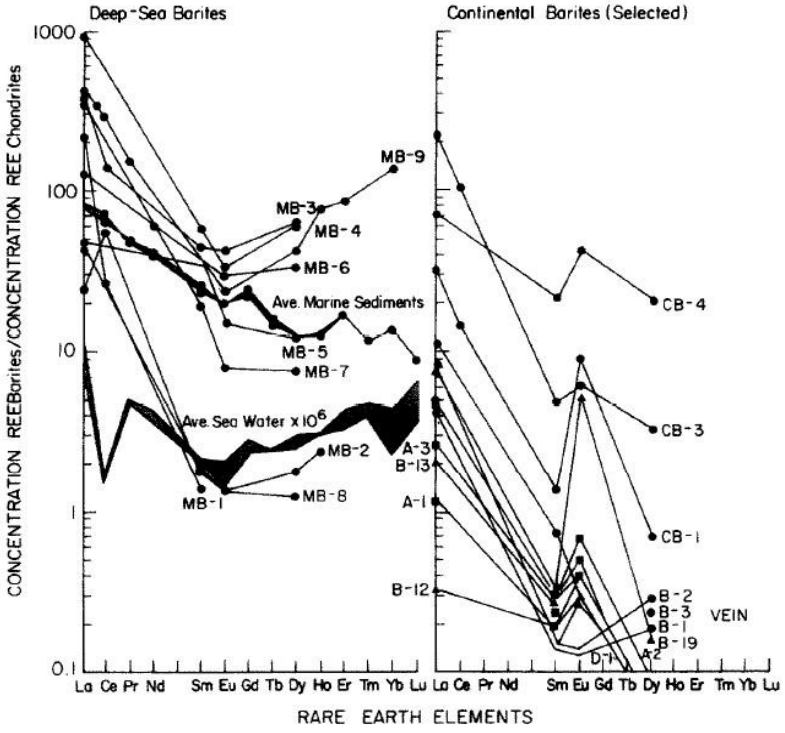

Figure 1.7. Results on REE concentrations in barites as obtained by Guichard. For discussion see text (Guichard, 1979).

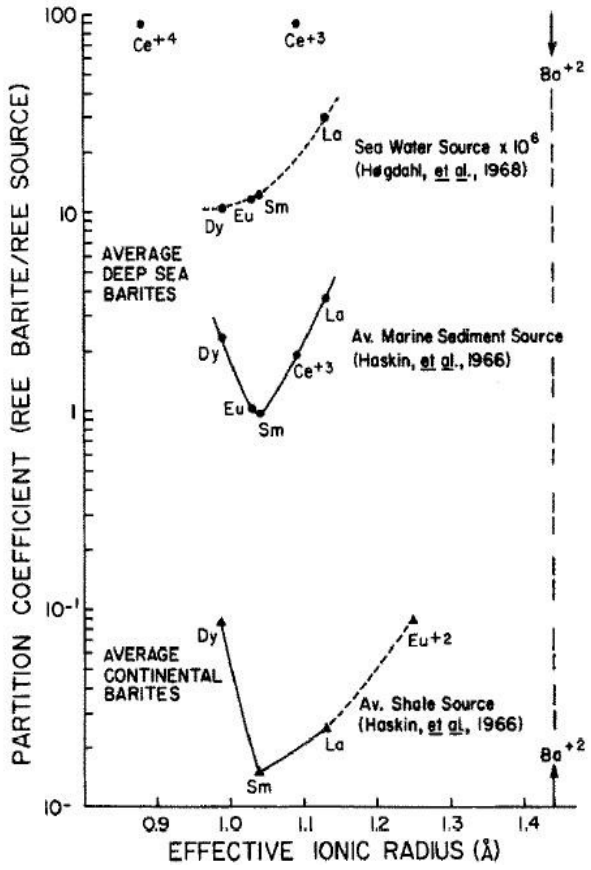

Figure 1.8. Dependence of the ionic radius of REEs on the partition coefficients in a variety of sources. The closer the effective ionic radius to the ionic radius of Ba^{2+}, the easier substitution can take place (Guichard, 1979).

search report. More interesting than Guichards results on REE distributions are his thoughts on the effects of REE partitioning in barite, since little is known about the controlling factors of this process. He suggests that crystallographic controls have played a role (*figure 1.8.*) but also suggests that complexing of REEs in barite-forming solutions competes against the process of barium substitution (Guichard, 1979). However, the partitioning coefficients for all the REEs in barite are assumed values due to lack of knowledge on the REE composition of the host fluid solution and the effective ionic radius of the REE cations during substitution (Guichard, 1979). It would probably be better to use the approach used by Kagi[1] (1993) for the determination of REE partitioning coefficients in calcium-sulfate, since this mineral is an analogue for barite in terms of crystallography. However, it is beyond the scope of this research to apply the obtained relationship between REE cations and the substituted calcium cations as derived by Kagi[1] (1993) to barite in order to obtain results on the partitioning coefficients of REEs in barite to check Guichards results.

Martin et al; 1995. Strontium and Neodymium isotopic analysis of marine barite separates.

Although Martin et al (1995) focus more on the reliability of barite as a paleo-oceanographic monitor in terms of Strontium and Neodymium isotopes, they draw some important conclusions on the apparent problems of marine barite phase separation that causes discrepancies in the data of Guichard (1979). During the chemical steps taken to purify the barite samples, continental contaminants such as anatase, rutile, zircon and sphene will not be removed (Martin et al, 1995). It is therefore proposed that the high REE concentrations that Guichard (1979) obtained for the samples derived from the deep-sea were most likely representing barite samples which were contaminated with continental material (Martin, 1995). It is therefore important to

[1]Kagi (1993) argued that for REE substitution for Ca^{2+} in $CaSO_4$(s) the apparent distribution coefficient (D) of the REE ion (Ln^{3+}) between the $CaSO_4$ crystal and the solution could be written as

$$D = \frac{(Ln^{3+})_s/(Ca^{2+})_s}{(Ln^{3+})_l/(Ca^{2+})_l}$$

where s is solid and l is liquid. The substitution of REEs implies a volume change of the solution from L_0 to L, such that the distribution coefficient of REE between $CaSO_4$ crystal and its saturated solution can be calculated from the REE concentration that can be measured and the volume (weight) change of the solution according to the rearrangement of the equation for the distribution coefficient to:

$$D = \frac{L_0*(Ln^{3+})_{l0} - L*(Ln^{3+})_{lF}}{Ln^{3+}{}_{lF}*(L_0 - L)}$$

identify the presence of the major constituents of these minerals when determining the environment of formation of the barites from the obtained REE patterns: Ti and Zr.

Barrett et al, 1990. Rare earth elements geochemistry of massive sulfides-sulfates and gossans on the Southern Explorer Ridge.

This research does not focus solely on REE patterns in pure barite, but investigates the distribution of REEs in sulfides containing a small percentage of sulfates such as barite. The REEs were determined by ICP-MS measurements of a digested sulfate-sulfide mineral, thereby correcting for the interference of $^{135}Ba^{16}O$ on ^{151}Eu using the 'doubly charged' technique (Barrett et al, 1990; Jarvis et al, 1989). However, the large Eu anomalies as recorded for the massive sulfates-sulfides are probably still due to the interference effect, since only a small part of Eu (1-2% of the parent ion) is doubly charged (Jarvis et al, 1989) and not all interfering material will thus be removed as proposed by Barrett et al (1990). Furthermore, during the chemical separation technique, a barite residue was removed from the final solution (Barrett et al, 1990), it is well possible that this barite residue comprised a part of the total REE abundance, thereby resulting in an underestimation of the REE concentration in the rocks.

1.4 Precambrian ocean and atmosphere compositions.

When discussing Archean barites it is important to realize that a lot of now common processes were different during the formation of the Early Earth, tectonically as well as geochemically. Therefore, in order to give a good context for this research the sulfur cycle and the oceanic compositions are briefly discussed below.

1.4.1. Archean atmospheric compositions.

When discussing the Archean atmosphere, one of the most important subjects is the first appearance of significant oxygen levels in the atmosphere. Oxygen accumulation in the atmosphere is important with respect to barite formation since atmospheric oxygen promotes the oxidative weathering of rocks on land forming oxidized species such as iron oxides and soluble sulfates (Canfield, 2000). In the literature, 2 scenarios are proposed for the dating of the first accumulation of significant oxygen levels in the atmosphere (Canfield, 2000). It is either thought that atmospheric oxygen levels reached present-day levels 3.8Ga and persisted ever since (Ohmoto, 2006) or that atmospheric oxygen first began to accumulate much later at 2.2-2.3Ga during the Great Oxidation Event (Canfield, 2000). Research is carried out by Canfield (2000) towards the timing of the Earths oxidation event by analyzing the relation between temperature and sulfur isotope fractionation of Sulfate Reducing Bacteria (SRB) at temperatures >45°C. Archean marine sediments normally show a low sulfur fractionation ($\delta^{34}S$ = +5‰ in the Archean compared to $\delta^{34}S$ = +2-+3‰ in modern marine sediments) which is proposed by Canfield (2000) to be a result from A) sulfate reduction at low sulfate concentration of <1mM where isotope fractionation during sulfate reduction is greatly reduced and B) a non-biogenic source of sulfide if the SRB had not yet evolved (Canfield, 2000). However, since SRB are thought to have been evolved before the cyanobacteria it is proposed that low fractionation of sulfide is caused by low oxygen concentration in the atmosphere, implying first accumulation of oxygen at 2.2-2.3Ga (Canfield, 2000).

1.4.2. Archean oceanic compositions.

Also of significance is the composition of the early ocean, especially with respect to the pH, pCO_2, concentrations of sulfate and the flux of rare earth elements.

An interesting model to determine the pH and pCO_2 is proposed by Grotzinger in 1992 that uses a simple equilibrium model of the carbonate system into account knowing that in the Archean, no calcium sulfates (gypsum) can be found that formed in the open marine basin (Grotzinger, 1992). The absence of these deposits in the early

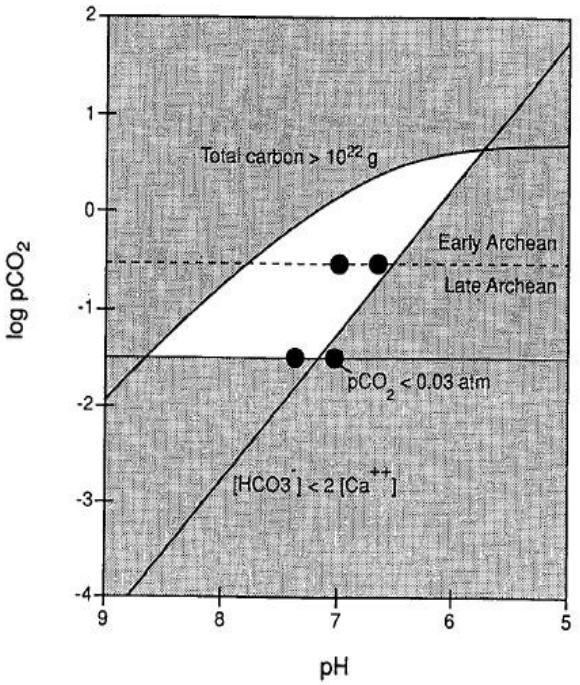

Figure 1.9. Possible range of pH and pCO_2 conditions for Archean seawater (Grotzinger, 1992).

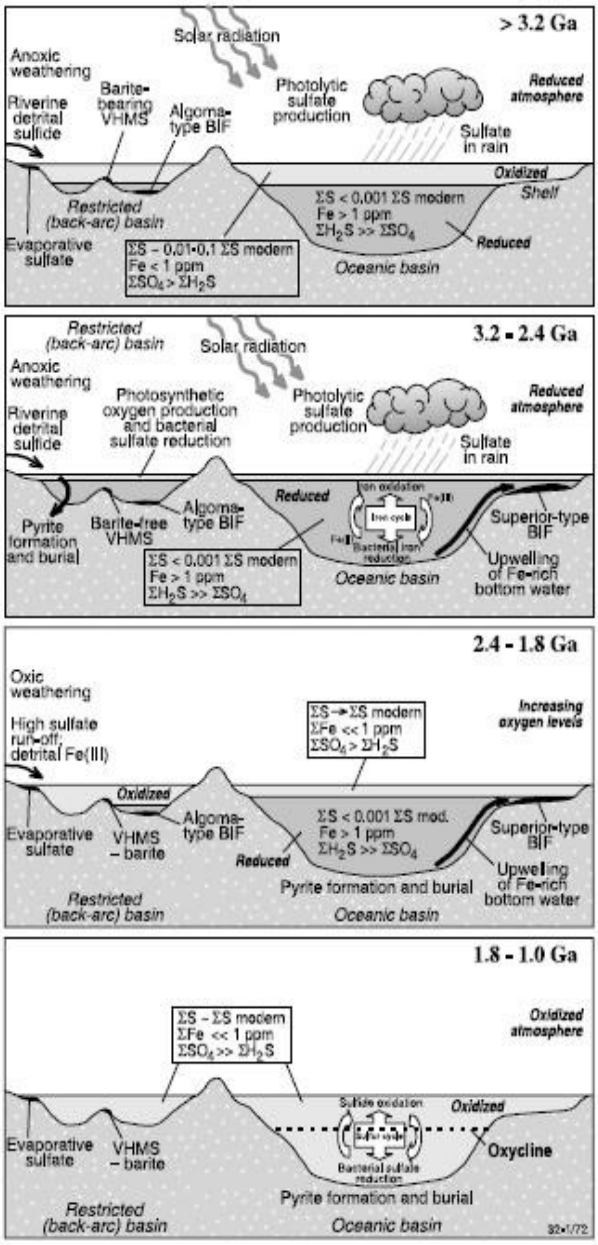

Figure 1.10. Overview of the evolution of the Archean atmosphere and oceanic conditions in terms of sulfur (Huston, 2004).

Earth can be explained by 2 scenarios: A) oceanic sulfate concentrations were very low or B) calcium was removed by abundant bicarbonate in the oceans (Grotzinger, 1992). At an ocean temperature of 25°C, supersaturation of the ocean with respect to calcite by a factor 2 and CO_2 as the main greenhouse gas are all assumed and if the total available carbon in the ocean is taken as 10^{22}grams (compared to 10^{19} for the oceans now - difference results from the absence of major landmasses in the Archean) a field could be constructed displaying possible pCO_2 and pH values for the Archean ocean (*figure 1.9.*) (Grotzinger, 1993). These values are consistent with pH and pCO_2 values obtained by Holland using a model for the concentration of Fe^{2+} in solution (Grotzinger, 1993). The sulfate concentration of Archean oceans were <200µM, maintained by volcanic outgassing of SO_2 and allowing an atmosphere controlled by anaerobic oxidation of methane (AOM) (Habicht et al, 2002) (Riedinger, 2005). More detailed information on the sulfate concentration is given by Huston (2004) who states that the redox state and the abundance of sulfur in the hydrosphere varied widely during the Archean and the Proterozioc. The following sequence in redox state and sulfur composition is proposed: 1) <3.2Ga: sulfur-rich upper layer and sulfur-poor and reduced lower layer of the hydrosphere, 2) 3.2-2.4Ga: uniform sulfate-poor concentration throughout ocean due to sulfate reduction by SRB, 3)around 2.4Ga: layered oceans due to oxygenation event (as also proposed by Canfield, 2000) with sulfate-rich surface waters and reduced, sulfate-poor bottom waters and 4) 2.4-1.8Ga: buffered redox state and homogenization towards sulfate-rich hydrosphere (Huston et al, 2004). A complete overview of these processes is given in *figure 1.10* (Huston, 2004).

The trace element chemistry of seawater is a balance between the flux of REEs from the continental crust derived from erosion and the flux of REEs derived from hydrothermal alteration of the oceanic crust (Derry and Jacobsen, 1990). In modern oceans, it is assumed that there are 3 sources for REEs in seawater: dissolved loads in rivers, hydrothermal alteration of the oceanic crust and sediments undergoing diagenesis (Derry and Jacobsen, 1980). Of these three, the hydrothermal flux resulting in a HREE enrichment and the dissolved loads in rivers resulting in a LREE depletion and Eu enrichment are most important (Derry and Jacobsen, 1980). In rivers, the REEs are mainly derived from weathering of continental material, resulting in a shale-normalized pattern (Piper, 1974). In hydrothermal vent systems the REEs are derived from chemical ion exchange with hydrothermal plagioclases formed during dissolution and alteration of MORB plagioclase (Klinkhammer et al, 1994) Therefore, the REE content of hydrothermal fluids can differ significantly on a local scale, dependent on the degree of albitization within individual vent systems (Klinkhammer et al, 1994).

The behavior of LREE and HREE in hydrothermal vent systems changes not only laterally (Klinkhammer et al, 1994) but also decreases with increasing depth because of scavenging of hydrothermal REEs by Fe-Mn nodules during Ce^{3+} to Ce^{4+} oxidation (Piper, 1974)(Bau and Dulski, 1999)(Derry and Jacobsen, 1980). This results in the thought that the hydrothermal REE flux is insignificant to the REE contribution to the oceans (Bau and Dulski, 1999). However, in early Precambrian times, the oxygen levels in the atmosphere were significantly lower and this removal mechanism did not yet operate (Bau and Dulski, 1999). This means that in the Archean all REEs from hydrothermal vents (the black smokers) could accumulate in the deeper parts of the oceans (Bau and Dulski, 1999). However, it was found that modern day black smokers result in lower REE concentrations as those measured in Archean deep-sea sediments, implying that the high REE concentrations in Archean sediments is mainly due to the contribution of surface waters not affected by high-T hydrothermal input (Bau and Dulski, 1999).

1.5. Sample description.

A variety of Barite-(Celestine) samples were taken from the Utrecht University mineral collection. The samples were selected for their size and the availability of enough material to grind some of it, their variety in textures and colours and - most important - their origin. It was crucial that at least to some extent the possible environment of formation of these barites was known, since this information is used to cross-relate the obtained REE-patterns with the environments of formation of Archean barites. The Archean barites were both derived from the mineral collection of Paul Mason (Dresser Barite) and from rocks obtained by Paul Mason and Desiree Roerdink during fieldwork in South-Africa. A table with the main characteristics, names and locations is given below:

Sample name	Location	Characteristics*
1880-318	Alston Moore, Cumberland, UK	Platy crystals, white color, slight transparent
1896-45	Frizington, Cumberland, UK	Well-formed crystals, white color, transparent
1986-1321	Bad Grund, Harz, Germany	Inhomogeneous sample, dark green to yellowish color, transparent
1986-1334	Sieberthal, Harz, Germany	Granular material, pink color, opaque
1923-19	West-Cumberland, UK	Well-formed crystals, green to red color, transparent
DB5	Dresser deposit, North Pole Dome area, East Pilbara basin, Australia	Granular/massive material, grey color, slight transparent
08-LON-01	Londozi deposit, Barberton greenstone belt, South-Africa	Granular/massive material, white color, slight transparent
08-BV-01	Barite Valley, Barberton greenstone belt, South-Africa	Massive material, greenish to grey color, slight transparent
Ver02	Vergelegen deposit, Barberton greenstone belt, South-Africa	Massive material, white, opaque
Ver01D	Vergelegen deposit, Barberton greenstone belt, South-Africa	Massive material, white to grey, opaque
TR-04.1	Stentor deposit, Barberton greenstone belt, South-Africa	Massive material, grey, opaque
Foss Barite	Foss mine, Aberfeldy, Scotland	Massive material, white to grey, slight transparent

Table 1.1. Overview Barite samples used. **Characteristics is just a very brief description of the rocks. Extensive optical microscopy study towards the textures of the barites would be beyond the scope of this research. Additional information on the barite of Barite Valley can be provided by Tessa van der Voort, BSc-thesis (unpublished).*

Geology and environments of formation of barite in the Alston Moore area, Cumberland, United Kingdom [sample 1880-318].

The platy white sample from Alston Moore, Cumberland is derived most likely from the North Pennine orefield on the Alston block (one of the structural highs) (Bouch, 2008). These structural highs are composed of Lower Paleozoic sediments and volcanic rocks that are intruded by Caledonian ganites (Bouch, 2008). This sequence is overlain by Carboniferous limestone, sandstone, mudstones and some minor thin coals (Bouch, 2008). The mineralization in the Alston block is a stratabound type, is hosted mainly in a conjugate system of steeply-dipping normal faults and is characterized by a marked zonation from fluorite to barite that corresponds with the form of the underlying Weardale granitic batholiths (Bouch, 2008). Radiometric data shows that the main mineralization has most likely taken place from the latest Permian to the end of the Triassic (Bouch, 2008). Fluid inclusion and stable isotope analysis reveal that the barite monophase fluids in the inclusions have generally lower salinities than observed in other stratabound minerals. Furthermore, this monophase character and low T_{fm} (~-55°C) indicate relatively cool conditions during precipitation from a mixed NaCl-$CaCl_2$ brine (T<50°C). This temperature is also obtained when $\delta^{18}O_{SMOW}$ are considered (10-15‰)(Bouch, 2008). The general conclusion made is that the lower temperatures and salinities of fluid inclusions in barite relative to inclusions in fluorite and quartz possibly indicate that this represents the waning stages of hydrothermal circulation, possibly under slightly cooler conditions when the sources of metals within the basement and/or igneous rocks had become depleted (Bouch, 2008). *Figure 1.11* a model as proposed by (Bouch, 2008) for barite mineralization in the Alston Moor area.

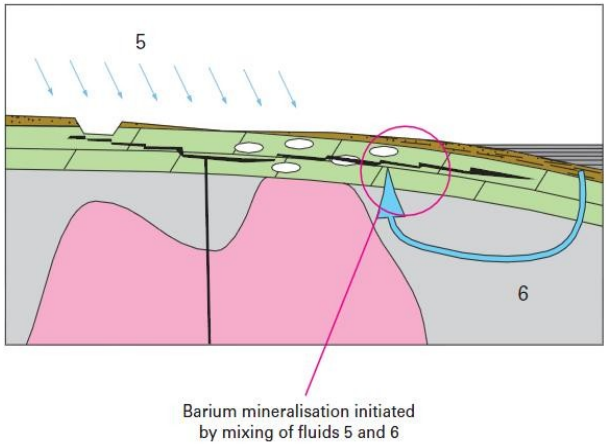

Figure 1.11. Proposed model for Triassic (?) barium mineralization from meteoric water with dissolved evaporates (fluid 5): low salinity, low Na:K and high sulphate content. This mixes with an evaporated brine (fluid 6): reduced salinity, waning circulation, reduced metal content and reduced temperature (Bouch, 2008).

Geology and environments of formation of barite in the Sellafield (Frizington) area, Cumberland, United Kingdom [samples 1896-45 and 1923-19].

The town of Frizington is located in the Sellafield area in west Cumberland in what is called the west-Cumberland iron ore field. The stratigraphy of the area is composed of Lower Paleozoic basement (acidic granite intrusions and the Borrowdale Volcanic Group). On top of this basement a succession of Lower Carboniferous (Dinantian) limestones can be found, which in turn are overstepped by a Permo-Triassic succession (Brockram conglomerate, Magnesian limestone, St Bees shale and St Bees sandstone) (Rowe et al, 1998). The area is bordered in the South-East by the Lake District Boundary Fault and in the North-East by the Dent Fell Anticline. The iron ore can be found in the Frizington (Dinantian) limestone formations characterized by a sharp contact between the ore and the unmineralized zone. This contacts comprises of a marginal zone of gangue mineralization of which barite is one of the main minerals (Rowe et al, 1998). Research by Milowdowski and co-workers (1998) further details the petrology and paragenesis of the vein mineralizations and uses fluid inclusions and $^{87}Sr/^{86}Sr$ ratios to determine the conditions during formation. It is concluded that the vein minerals in the Sellafield area are produced by no less than 9 'Mineralization Episodes' (M1-oldest to M9-youngest)(Milodowski et al, 1998). Barite can mainly be found in ME6c, where barite and fluorite mineralizations are most extensively developed in the Carboniferous limestone and the Brockram conglomerate deposits (Milodowski et al, 1998). The general idea is that all mineraliza-

tion in the ME6 was deposited from a warm, highly saline complex Na-Cl-Ca-SO_4 basinal brine. However, the ME6c barite does show some different data compared to the other vein minerals, such as an anomalous low $^{87}Sr/^{86}Sr$ (~0.7090 vs ~>0.7100), lower T obtained from fluid inclusions (<80° C vs 53°-180° C)and lower salinity (18 wt% vs >25 wt %) (Milodowski et al, 1998). Also the sulphur isotopic composition is significantly lighter ($\delta^{34}S_{CDT}$ +3.9 to +8.1‰) than other vein minerals in ME6 such as anhydrite (Milodowski et al, 1998). The ME6c barite mineralization of which the barite samples as tested in this report are assumed to be equal to is thus considered to result from the mixing of a warm, complex, sulphate-rich basinal mineralizing brine (derived from the East Irish Sea Basin area) with a second, less saline, low-sulphate local fluid carrying Ba during early stages of ME6c (Milodowski et al, 1998).

Geology and environments of formation of barite in the Harz mountain region, Germany.

In the Harz mountains in Germany, stages in vein mineralization (Late-Variscan and Mesozioc) have resulted in deposits of sulfidic ores such as fluorite and barite along WNW-ESE striking faults (Lüders et al, 1993). Barite mineralization is distributed close to the western and southern borders of the mineralization region (Lüders et al, 1993). The Harz region can be subdivided into the Upper Harz region, the Middle Harz Region and the Lower Harz region. Sulfur isotope studies show that there are distinct differences between $\delta^{34}S$ values between these regions, indicating that sulfides from different ore districts either derived their sulfur from distinctly different sources or formed under quite different physiochemical conditions (Zheng and Hoefs, 1993). Two samples used for REE pattern studies are derived from two different regions in the area of which the geology and environment of barite formation are described below.

1) Bad Grund deposit [sample 1986-1321].

The Bad Grund deposit is located in the Upper Harz region which is characterized by Triassic-Jurassic sulfides, quartz, calcite and a later-stage barite gangue sulfide (Möller and Lüders, 1993). All ore deposits occur as vein mineralizations occurring on NW-SE shear zones that are formed during activation of a local stress field during Mesozioc wrench faulting through the Eoalpine collisions in the Late-Cretaceous/Early Tertiary. The vein mineralizations are hosted by an approximately 6km thick sequence of Ordovician to Lower Carboniferous sediments and basic and acidic volcanic (Möller and Lüders, 1993). The vein sulfates are characterized by a $\delta^{34}S$ value of +13 to +15‰ and $\delta^{18}O$ values of +12 to +17‰, these results are interpreted as evidence for a hypogene (subsurface) origin of the barites (Zheng and Hoefs, 1993). Comparison of the $\delta^{34}S$ values with those of known sulfur reservoirs in the area will give an indication on the source of the sulfur. For the Bad Grund deposits, the $\delta^{34}S$ values correspond approximately with $\delta^{34}S$ values of Zechstein sulfate in the region (+10 to +13‰) and sulfur is thus either derived from the Zechstein ocean waters or from weathered Zechstein evaporates. Since the Bad Grund barites are dated younger than the main Pb-Zn hydrothermal mineralizations, the Zechstein evaporates is the most likely sulfur source. The origin of the metal-rich fluids is determined using temperature indicators as 1) fluid inclusions in calcite/fluorite (T_h= 250-300°C) 2) Ga/Ge ratios in silicates (T_{min}=250°C) 3) $\delta^{13}C$-$\delta^{18}O$ relationship in calcite (T=200-300°C) and 4) positive Eu anomalies in carbonates and fluorites (T>250°C) (Möller and Lüders, 1993). These high temperatures point towards a deeper crustal source for the metal-rich waters.

2) Sieberthal (Sieber valley) deposit [sample 1986-1334].

The barite veins (up to 9km long) that can be found in the Sieber syncline in the Middle Harz region are among the most persistent vein systems in the Harz (Stedingk and Stoppel, 1993). The Sieber syncline and the associated Blankenburg fold zone are characterized by pre-flysch and flysch sediments, ranging from Devonian slates, greywackes, siliceous slates and volcanic to Lower Carboniferous greywackes. Notable is the presence of granitic intrusions in the area that are assigned Late Carboniferous to Permian

ages and are thought to have had an effect to the mineralization in the area (Stedingk and Stoppel, 1993). Mineralization in the area has taken place in several stages (Stedingk and Stoppel, 1993). The sample as examined in this research shows a pinkish color which could be an indication for a stage-4 formed barite. The barites of the Sieberthal are characterized by $\delta^{34}S$ values of +6.6 ~+8.3‰ and $\delta^{18}O$ values of +12 to +15.5‰ (Zheng and Hoefs, 1993). The relatively low $\delta^{34}S$ values most likely indicate that the sulfur source in either sulfide or sulfate minerals is a mixture of sulfur from igneous sulfide and Zechstein sulfate (Zheng and Hoefs, 1993). Since the range of $\delta^{34}S$ values gives an indication on the mixing of sulfurs during the ore-genarating event, the narrow range of $\delta^{34}S$ values in Sieber barites indicates that the sulfurs were fairly well-mixed in the hydrothermal fluids (Zheng and Hoefs, 1993). Also the barite mineralizations at Sieberthal thus are thought to have evolved from hypogene mixing of hydrothermal fluids also indicating a high-T origin of the barites.

Based on carbon and oxygen isotopic data, Zheng and Hoefs (1993) have proposed the existence of 2 separate fluids: I: earlier, H_2CO_3-dominant (350 -150°C) and II: later, HCO_3^--dominant (100-50°C). These authors suggest that the fluid I took up the igneous sulfur (or well-homogenized crustal sulfur) to form the calcite -sulfite mineralizations in the Upper and Lower Harz on one hand while leaching the sedimentary sulfide-sulfur to form calcite-sulfide mineralizations in the Middle-Harz. At a later stage, fluid II would have taken up the Zechstein sulfate to form the barite mineralizations and subsequently altering the primary calcite in the Middle Harz and Upper Harz (Zheng and Hoefs, 1993).

Geology and environments of formation of the Foss Barite, Aberfeldy, Scotland *[sample Foss Barite].*

The Aberfeldy stratiform barite deposit is part of the late PreCambrian to Lower Cambrian metasediments of the Dalradian supergroup located in the Grampian Highland in Scotland (United Kingdom) (Willan and Coleman, 1983). These metasediments comprise a 20-25km thick assemblage that underwent complex polyphase deformation and metamorphism during the Lower Ordovician Grampian Orogeny (520-460 Ma.) (Willan and Coleman, 1983). Granites intruded the sedimentary stack during Late Silurian to Lower Devonian orogenesis (415-400 Ma.), a

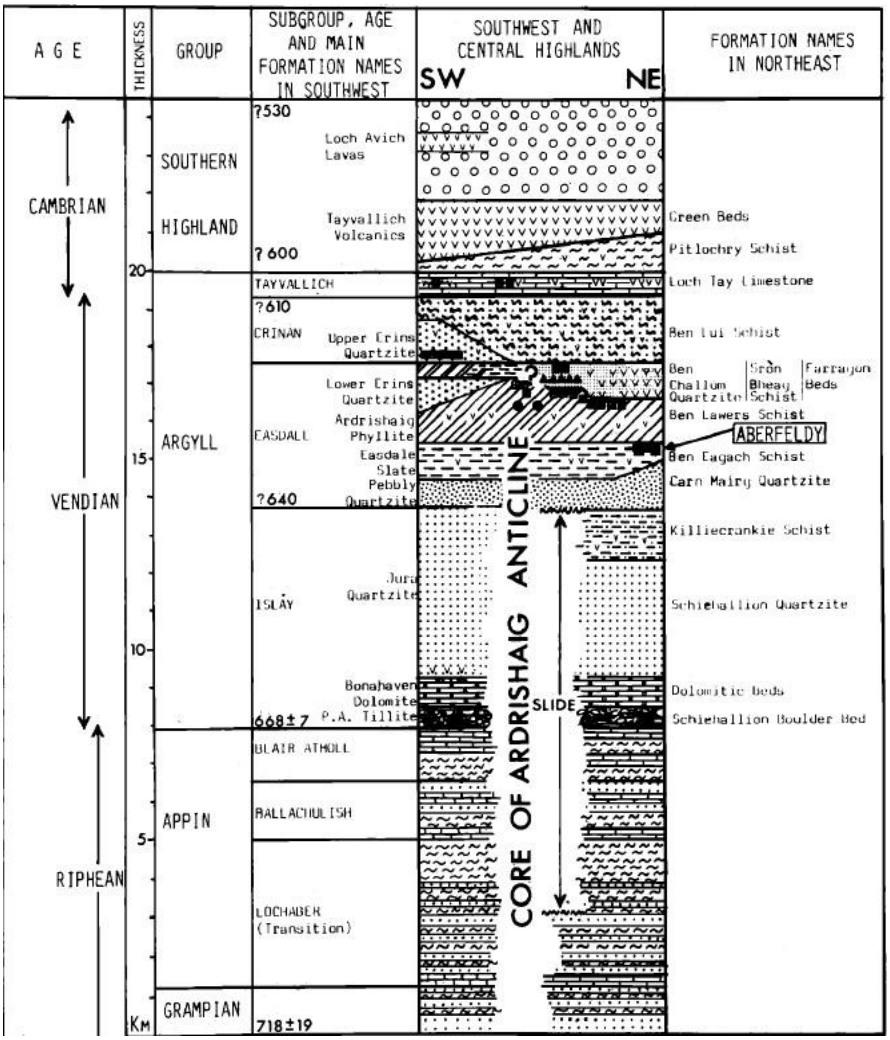

Figure 1.12. Stratigraphic column of the Dalradian Supergroup in Aberfeldy, Scotland (Willan and Coleman, 1983).

process that is also responsible for the formation of sinistral strike-slip faults in the area (Willan and Coleman, 1983). As can be seen in the stratigraphic column in *figure 1.12*, the Dalradian supergroup is divided into four lithostratigraphic groups and several subgroups (Willan and Coleman, 1983). The massive barite beds of the Aberfeldy deposit are part of the 5km thick sediments of the Argyll subgroup that exhibit rapid lateral thickness and facies changes (Willan and Coleman, 1983). The Aberfeldy Ba, Zn and Pb deposit is surrounded by the Ben Eagach Schist that is characterized by high sulfide contents and is considered as the beginning of exhalative activity (Willan and Coleman, 1983). $\delta^{34}S$ study towards the sulfates and the sulfides at the Foss mine where the Aberfeldy barite deposit is exposed show that this deposit is formed during a climax in hydrothermal activity, when hot (200°C) type IIa brines were expelled onto the seafloor. These brines were entrained in the seawater by the feeder system as a result of intense hydraulic fracturing and increased rock permeabilities. The barite deposit resulted from the activity of a white smoker where sulfates are precipitated as a result of cooling (Willan and Coleman, 1983). The bulk of the barium sulfate was derived from Precambrian ocean waters that most likely have shown a $\delta^{34}S$ enrichment relatively to the modern ocean water due to bacterial reduction (Willan and Coleman, 1983).

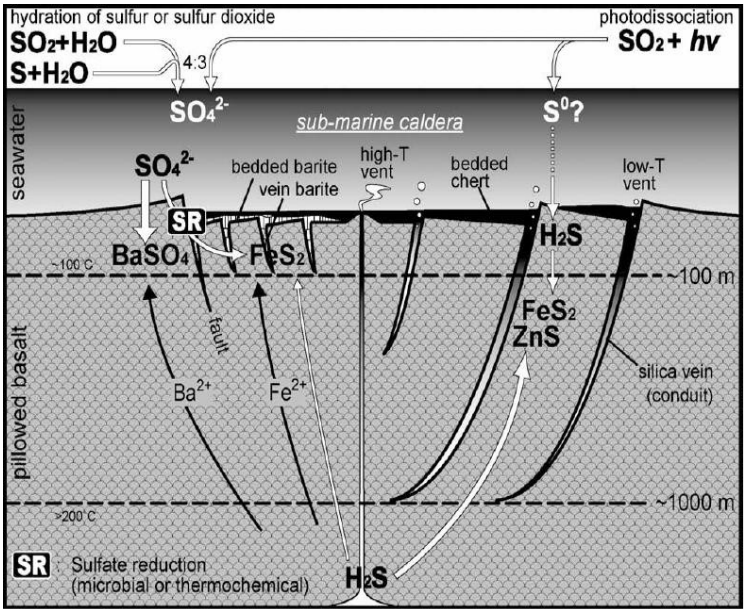

Figure 1.13. Proposed model for the formation of the Dresser barite deposit, North Pole basin, Pilbara, Western Australia (Ueno, 2008).

Geology of the Dresser barite deposit, Australia *[sample DB5].*

The Dresser Formation crops out in the North Pole area, central Pilbara Granite-Greenstone Terrane, Western Australia (Ueno et al, 2008). Barite occurs as bedded (0.1-5m thick) barite interlayered with chert (1-70m thick or thinner layers) in a 6km thick succession of basaltic greenstones (Ueno et al, 2008). The cherts and greenstones in the Pilbara area are overlain by the felsic volcanic of the Panorama Formation that is dated 3.458Ga (Ueno et al, 2008). Galena dating of the Dresser Formation lead to a depositional age of 3.490Ga (Ueno et al, 2008). Barite can also be found as accessory mineral in silica-veins that intrude into the Dresser formation (Ueno et al, 2008). The distribution of these veins and the presence of barite in these veins indicate that hydrothermal fluids circulated to depths of at least 1000m and less than 100m below the seafloor at depth of deposition of the Dresser Formation (Ueno et al, 2008). Negative $\Delta^{33}S$ anomalies support a feeder/deposit relationship for the barite deposition of which a proposed model is given in *figure 1.13* suggesting a seawater source for the sulfate (Ueno et al, 2008).

Geology of the Barberton greenstone belt deposits [samples TR-04.1, 08-LON-01, Ver01D, Ver02 and 08BV01].

The Barberton greenstone belt is located in South-Africa and Swaziland (*figure 1.14.*) and contains barite deposits that cover the entire time span from which sulfate-deposits are known in the Archean. Lower greenschist facies to amphibolite facies metamorphism have affected the greenstone belt and the barites. The following description of the geology is taken from Roerdink et al, 2011 (submitted).

Londozi barite [sample 08-LON-01]

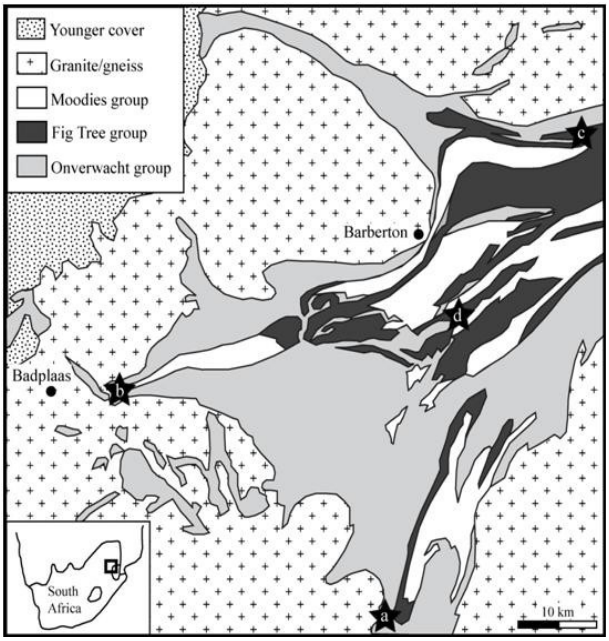

Figure 1.14. Location and simplified geology of the Barberton Greenstone belt in South-Africa (Roerdink, submitted).

The Londozi deposit is located in the southeastern part of the Barberton greenstone belt (amphibolite facies metamorphism). The volcaniclastic sediments of the Lower Onverwacht group (3.4Ga) (Lowe and Knauth, 1977) have been intruded by the 3.511-3.502Ga Steynsdorp pluton, dominating the region. Barite occurs in lenses of variable thickness (0.5-10m) in a zone that can be traced laterally for about 1km along strike. Barite is often associated with strongly silicified host rocks and finely crystalline barite is often interbedded with thin layers of chert while some contain slivers of amphibolite wall rock. At the contact between the barite and the wall rock, accessory minerals such as titanite, spinel and garnet occur. Associated sulfides include pyrite, sphalerite and to a lesser extent chalcopyrite and galena. Dating of felsic volcanics adjacent to the Londozi deposit revealed an age of 3.540Ga suggesting that this is the oldest sulfate deposit known in the geological record. The 08-LON-01 sample was collected from a barite outcrop along a road.

Vergelegen barite [samples Ver01D and Ver02].

A small barite deposit that represents the westward extension of the Buck Reef chert occurs on Farm Vergelegen in the westernmost part of the Barberton greenstone belt. The barite-chert deposit is located on top of sheared mafic to intermediate layers in the south while it is overlain by talc-carbonate schists and sheared serpentenites in the north. Sulfides are absent in this deposit. Although poorly constrained, the association of the barite-chert deposit with the top of the Onverwacht group suggests an age around 3.4Ga. Barite can be found as thinly bedded barite with chert to thinly bedded chert with barite. In the main outcrop, barite can be up to 30m thick occurring as a white to grey coarse crystalline rock. The deposit becomes more heavily deformed from the east where sample Ver01D is derived towards the western part of the outcrop from where sample Ver02 is derived.

Stentor barite [sample TR-041].

The Stentor barite deposit can be found as two related, parallel seams of barite occurring in the northeast part of the greenstone belt near the Stentor pluton. The barite belongs to the Bien Venue Formation of the lower Onverwacht Fig Tree Group which is dated 3.256-3.260Ga. Barite beds are interlayered with chert bands and occur in quartz-muscovite schist host rocks which are derived from felsic volcanics and volcanoclastics. The total thickness of the barite is around 70m and the deposit can be traced over 700m along strike. Intrusion of the Stentor pluton and the Nelspruit batholiths 150My after deposition resulted in middle to upper greenschist facies metamorphism of the barite deposit with temperatures ranging from 380°C-410°C and pressures ranging from 4.2-4.5kbar. The sample TR-041 is collected from the Stentor farm.

Barite Valley barite [sample 08BV01].

The youngest (3.23-3.26Ga) barite deposit is located in the area of the Barite Valley in the central part of the greenstone belt. This region is mainly dominated by terrigeneous clastic sediments belonging to the Lower and Middle Mapepe Formation of the Fig Tree Group. Barite can both be found as detrital sand-size accumulations or as bladed crystals (diverging bundles or 2-10cm long blades). The detrital barite is green-coloured and contains 2-5% pyrite and heavy mineral phases including chromite and zircon. The bladed barite crystals are thought to be

formed during early diagenesis. The barite horizon occurs above a chert-rich zone containing the basal chart of the Fig Tree Group and is overlain by sandy tuffaceous sediments, coarser greywackes and shales. The sample is derived from a surface outcrop, containing both bladed and detrital barite.

2. Methods.

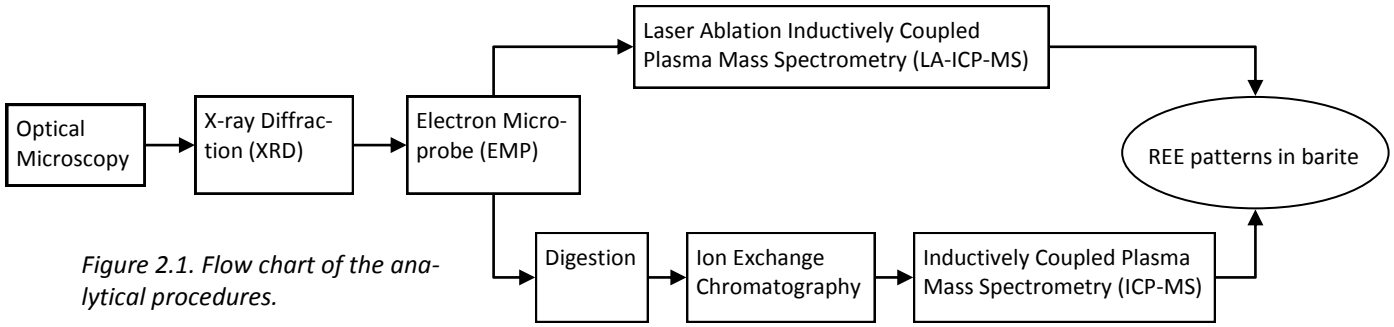

Figure 2.1. Flow chart of the analytical procedures.

In order to determine the REE abundances in $BaSO_4$, two different analysis were performed: Laser-Ablation Inductively Coupled Plasma Mass Spectrometry (LA-ICP-MS) on in-situ solid rock material and Inductively Coupled Plasma Mass Spectrometry (ICP-MS) on solutions. These two analyses were performed in order to qualitatively verify the data obtained from the LA-ICP-MS, a relatively new technique for REE measurements in $BaSO_4$. Preliminary to these two analysis, qualitative analysis on bulk rock (X-ray Diffraction) and qualitative analysis on rock mineralogy (Optical Microscopy, Electron Microprobe analysis) were carried out to obtain an overview of rock composition and to obtain internal standards for LA-ICP-MS analysis. Furthermore, the solution ICP-MS analysis required digestion of the extremely insoluble mineral barite and development of an Ion Exchange Chromatography method to remove interfering elements. The flow-scheme above (*Figure 2.1.*)provides an overview of the various analysis steps taken.

sample	XRD	EMP	Ion Exchange chromatography	LA-ICP-MS	Total digestion
$BaSO_4$ powder			x		
1883-37		x		x	
1880-318	x	x*	x	x	x
1896-45	x	x*	x	x	
1902-39		x		x	
1972-8		x		x	
1880-390		x		x	
1890-45		x		x	
1923-19	x	x		x	
1986-1321	x	x*	x	x	
1986-1334	x	x*	x	x	
Foss Barite	x	x*	x	x	x
08-BV-01	x	x	x	x	x
Ver02	x	x	x	x	
Ver01d	x	x	x	x	
TR041	x	x	x	x	
DB05	x	x	x	x	
08-LON-01	x	x	x	x	x

*Table 2.2. Overview of samples and the analysis methods used per sample. Red crosses indicate samples that were measured, but showed bad results. The EMP samples indicated with an * have been measured twice.*

2.1. Optical Microscopy (OM).

A Micro1-LA-LABOLUX Polarization microscope (reflected light) with 16.5x magnification was used to study the presence of fluid inclusions and accessory phases. Especially the presence of continental contaminants as rutile, apatite and zircon was investigated, since these can influence the REE pattern from

marine chemical precipitates as barite (Martin et al, 1995). The presence of hydrated minerals such as mica's and amphiboles can point towards post-precipitation hydrothermal alteration of barite (Bau, 1991).

2.2. X-ray Diffraction (XRD).

The barite samples were measured using a 2D phaser X-ray diffraction analyzer (Buker) for quantitative bulk mineralogy analysis. Therefore, the rock is grinded into fine powder in an agate grinder and placed in a sample holder which moved at a speed of 15 rotations/min. The X-rays were produced by cobalt waves which have a wavelength of 1.79026Å, the sample powder is exposed for 15min to these X-rays. A range of refraction angles (2θ) of 5°to 85° was measured in steps of 0.05°, 0.5sec for every step. Obtained data is processed using EVA™ software resulting in counts versus refraction angle plots that have specific peaks for each individual mineral as determined and given by the ICDD (International Centre for Diffraction Data).

2.3. Electron Microprobe (EMP).

A JXA-8600 superprobe electron microprobe was used to determine concentrations of major elements (Ba, Sr, Ca, Mg, S and O) in the barite samples. Therefore, small grains of each barite (except the synthetic barite) placed in a carbon-coated epoxy sample holder were measured using a 5µm electron beam at 15kV/20 nano-ampere. Samples indicated with an asterix (*) in *table 2.2* were measured twice on two different occasions. Samples 1883-37 to 1986-1334 have been measured first with an average of 3 measurement per grain, samples indicated with an * and samples 08-BV-01 to 08-LON-01 were measured with an average of 5 measurement per grain. It was assumed that all grains were homogeneous and care was taken to ignite material from spots that looked free from fluid inclusions and accessory phases. The Electron Microprobe was calibrated before analysis using standard procedures.

sample	added Na2CO3(g)	added BaSO4(g)	total weight(g)	BaSO4: Na2CO3
1.1	4.6	0.40	5.0	1:12.61 1
1.2	4.5	0.50	5.0	1:9.94
1.3	4.4	0.62	5.0	1:8.13
1.4	5.0	0.00	5.0	

Table 2.3. Weights of powders used for Na_2CO_3 fusion method to digest $BaSO_4$ powder. Different ratios between powder and fusing material are taken in order to test which ratio will give the best result i.e. the pearl that will digest most easily.

2.4. Digestion.

This part will provide information on the digestion of barite using NaCO3-flux based fusing method as described by Barbieri et al, 1982 and Breit et al, 1985 and partly used by Guichard et al, 1979. It was necessary to dissolve 100% of the used barite sample to be certain that all REEs were dissolved and could be measured. Furthermore, because of low REE concentrations expected a significant amount of barite (0.5grams) must be dissolved in order to get detectable REE concentrations. Also other, however less successful, digestion methods were carried out of which an overview is given in *Appendix 1.*

2.4.1. Synthetic barite.

Barite powder was ordered from Merck KGaA, Germany and used as delivered. This powder was stated to be 98% pure and will further be referred to as "synthetic barite". Eight pearls were made by fusing synthetic barite with $NaCO_3$ (Merck, 99.5% pure) in Pt-crucibles (Guichard, 1979) at 1200°C for ~30min with a variable $BaSO_4$:$NaCO_3$ ratio as stated in *table 2.3.* This ratio was varied such that it could be tested which ratio would give the best results for the digestion. 1mL Lithium-Iodide (LiI) is added to enhance the recovery of the fused material from the Pt-crucibles, it is expected that this LiI is removed by evaporation during the fusing process. The fused Ba-REE oxide cake (Guichard, 1979) that formed was grinded into a very fine powder using an agate grinder. This powder is subsequently leached with UHQ in 50mL Greiner tubes. The suspension that forms during the leaching steps was centrifuged down and the supernatant water was collected and tested for the presence of sulfur using $BaCl_2$ and measured for Ba^{2+} by ICP-OES. After the third leaching step

(~150mL UHQ used), no precipitate was formed during the reaction of the supernatant water with $BaCl_2$ and the suspensions were dried down. The remaining residues were taken up in 5ml 6M HCl and diluted with UHQ to 1L in Nalgene™ bottles .

sample	Na2CO3 (g)	BaSO4 (g)	total weight (g)	BaSO4:Na2CO3
Ver02	4.5	0.51	5.0	1:9.9
1986-1334	4.5	0.50	5.0	1:10
Foss Barite	4.5	0.53	5.0	1:9.5
08-LON-01	4.5	0.51	5.0	1:9.8
1896-45	4.5	0.50	5.0	1:10.0
Ver01d	4.5	0.50	5.0	1:10.1
1986-1321	4.6	0.51	5.1	1:10.0
08-BV-01	4.5	0.55	5.1	1:9.2
1880-318	4.5	0.51	5.0	1:9.8
DB5	4.5	0.50	5.0	1:9.9
TR041	4.4	0.51	4.9	1:9.8
Foss Barite TD	6.3	0.71	7.0	1:9.9
1986-1321 TD	4.1	0.45	4.6	1:10.0
08-BV-01 TD	4.5	0.51	5.0	1:9.7
08-LON-01 TD	5.4	0.66	6.0	1:9.2

Table 2.4. Na_2CO_3 to $BaSO_4$ ratio as taken for the fusing method. This ratio was found ideal for producing an easy digestable pearl from the fusing experiments on $BaSO_4$ powder (see results).

2.4.2. Natural barites.

The selection of the natural rock samples as given in the column 'Ion Exchange Chromatography in *table 2.2.* were grinded to powder using an agate grinder. As a test, duplicates of samples 1880-318, Foss Barite, 08-BV-01 and 08-LON-01 were additionally exposed to a combination of HF, HNO_3 and H_2O_2 in order to remove silicates, organic material and carbonates to see if this additional treatment was necessary to obtain better results. It was necessary during this exposure to digest 3x0.250g of each sample to obtain a total volume of 0.750g (0.5g needed for fuse) due to limited volume of the digestion vessels. The remaining residue was added together. The residue was leached several times with UHQ to remove acids and dried down in a clean fume hood. All powders were fused with Na_2CO_3 powder (Merck, 99.5% pure) with a ratio given in *table 2.4.* in Pt crucibles for 30min at ~1200°C. The fused material was directly collected from the Pt-crucible and grinded in an agate-grinder to a very fine powder. Approximately 0.5g of this powder is leached with approximately 150mL UHQ to remove remaining sulfates. The leached fluid is tested for the presence of these sulfates by adding a few mL of $BaCl_2$.

After all sulfates were removed, the residual leached powder was dried down in a clean fume hood, weighted and taken up in ~5mL 6N HCl. This suspension is shaken overnight and diluted to 1L in Nalgene™ bottles. The 1L bottles are spiked with 50µL of a 974mg/kg Yb and 50µL of a 972mg/kg Pr solution except for samples 1986-1321, Foss Barite total digestion (TD) duplo, 08-BV-01 TD duplo, 1880-318 duplo, Foss Barite TD, 08-BV-01 TD and Foss Barite duplo that are spiked with 50 µL of a 984 mg/kg Yb and 50µL of a 984 mg/kg Pr solution. These elements were used as spike, since both the behavior of LREEs (Pr) as well as HREEs (Yb) during Ion Exchange Chromatography would be known. It was assumed that both elements were of limited interest for the determination of the environment of formation of the barite. This assumption was incorrect as will be discussed in chapter 4.

2.5. Ion exchange chromatography (REE preconcentration).

See *Appendix 2* for a detailed laboratory work flow sheet for the Ion Exchange Chromatography process as used for the removal of interfering species on REEs in solution. The method is developed by the Bau group of the Jacobs University, Bremen and is based on research by Winchester, 1963 and Shabani et al, 1992.

2.5.1. Synthetic barite.

Solutions 1.1A, 1.2A and 1.3A were spiked with approximately 1mL spike containing Ba and REEs in such quantities that a concentration of ~5µg

REE is expected in the final 40mL eluate. In a later stage (see results), solutions 1.2B, 1.3B and 1.4B were spiked with 0.5mL of the same spike such that ~2.5µg REE is expected in the final 40mL solution.

Sep-pak C18 cartridges (Waters) were cleaned by rinsing them with a 10mL 6N high-purity HCl at a flow speed of approximately 3mL/min followed by rinsing with 7mL UHQ at an equal flow speed. Approximately 0.5mL bis-(2-ethylhexyl) orthophosphoric acid was loaded onto the cartridge using a reverse pump direction and different tubing. The cartridge was rinsed again by flushing 10mL 6N high-purity HCl through it at a flow speed of 3mL/min followed by 10mL UHQ at a flow speed of 9mL/min.

After preparation of the cartridges, a different tube was attached to the pump and rinsed on the inside as well as the outside with a few mL 6N HCl and a few mL UHQ. 50mL of the initial solution was collected from the 1L initial solution in a 50mL Greiner tube before the prepared C18 cartridge was attached. The prepared cartridge was rinsed on the ends using 0.01N HCl and attached to the tube. The 1L bottle was transferred over the cartridge at a flow speed of 13mL/min and eluate was subsequently collected in 50mL Greiner tubes in order to be able to construct elution curves. These 50mL Greiner tubes were measured by the ICP-OES for Ba, Na and other major elements analysis. The cartridges now contain the REE which were eluted from the cartridge using 40mL 6M HCl solution. Again, elution curves were made by collecting the 8x5mL of eluate in 15mL Greiner tubes and diluting to 10mL before sending to the ICP-MS (Thermo Finnigan XR) for REE analysis.

It should be noted that the pump used (Masterflex consoledrive with Easyload™ II 77201-60 cartridge) is not well-suited for precise flow-speed measurements. Flow speeds given are therefore an approximation, however, caution is always taken that the fluids passed through the cartridges by drops rather than by a continuous flow. The tubing used in these experiments is Tygon™ precision tubing (T3606-23, Masterflex) with 8mm od /4,8mm id /1,6mm wall. Different tubing of the same type is used for HCl, ester and sample material. Samples and materials were always protected with parafilm during the process. Tubing was always rinsed in between different samples by passing through 40mL high-purity 6N HCl followed by 40mL UHQ at ~10mL/min.

2.5.2. Natural barites.

The spiked 1L Nalgene bottles with the Ba-REE oxide cake solution were pre-concentrated using the same methods as described for the synthetic barite, with the exception that >0.5mL of bis (2-ethylhexyl) orthophosphoric acid was loaded on the cartridge. 10mL of Original sample was collected in a 15mL Greiner and 10mL of Ba-eluate was collected as well in a 15mL Greiner for Ba analysis using the SpectroCiros ICP-OES. The pre-concentrated REEs were eluted using 40mL of 6N ultrapure HCl in 8 subsequent steps of 5mL in order to observe REE behavior during elution. REEs were analyzed using a ThermoFinnigan Element XR ICP-MS with APEX devolatization system using 0.5M HCL as matrix carrier fluid and using standard calibrations.

2.6. Laser-Ablation Inductively Coupled Plasma Mass Spectrometry.

In order to quantitatively determine the abundances of REEs in barite, the barite samples were measured as small individual grains (5mm) in an epoxy sample holder by a Thermo Finnigan, Element 2 mass spectrometer using a Microlas Geolas 200Q, 193nm excimer laser ablation system to ablate sample material. Nist 612 glass (37.5 ppm for all elements of interest) was used as reference material (Pearce et al, 1997). No external barite standard with known REE concentration was available. The values of the parameters used during laser ablation are:

Crater size:	60µm
Energy:	barite: <1 J/cm^2 (variable from 0.23 J/cm^2 for Vergelegen barite to 0.34 J/cm^2 for Stentor barite). NIST612: ~0.56 J/cm^2.

The non-Archean samples were measured first with 3 measurements on every grain with 200

Element	Chondrite (Anders and Grevesse, 1989)	PAAS (Nance and Taylor, 1976)
La139	0.32	38.0
Ce140	0.82	80.0
Pr141	0.12	8.9
Nd146	0.62	32.0
Sm147	0.20	5.6
Eu153	0.080	1.1
Gd157	0.27	4.7
Tb159	0.050	0.77
Dy163	0.33	4.4
Ho165	0.080	1.0
Er166	0.22	2.9
Tm169	0.030	0.50
Yb172	0.22	2.8
Lu175	0.030	0.50
Y89	2.1	28.0

Table 2.5. Normalization values for the LA-ICP-MS and ICP-MS REE concentrations.

analysis on every single spot. This measurement was done to get an indication of the REE abundances in barite and to test which internal standard could best be used. Therefore, the data was exported with ^{135}Ba, ^{137}Ba and ^{88}Sr as separate internal standards.

On the selected samples as indicated in *table 2.2.,* a new analysis was carried out with 10 individual spot measurements for every grain. Every single spot value represents an average of ~200 single pulses as measured by the ICP-MS (Thermo Finnigan Element 2). On every spot, REE isotopes were measured that were assumed to have no interference with any oxides present. Multiple-isotopes of each REE were measured where possible in order to be able to compare the obtained abundances and remove interferences. The data was exported with ^{88}Sr as internal standard, since this element was supposed to be measured more accurately than Ba^{2+}. Data was averaged and the consistency between several measurements was checked by dividing the average concentrations of REEs from two different measurement dates of samples 1923-19, 1986-1334, 1986-1321 and 08-BV-01. The concentrations (all ppm) were averaged and the average value was normalized to Post Archean Average Shale (Nance and Taylor, 1976) and Chondrite (Anders and Grevesse, 1989) values as given in *table 2.5.*

2.7. Inductively Coupled Plasma Mass Spectrometry (ICP-MS) and Inductively Coupled Plasma Optical Emission Spectrometry (ICP-OES).

Solutions that are stated in the text before to have been measured with the ICP-MS are analyzed by either the Thermo Finnigan Element 2 or a Thermo Finnigan XR using standard calibration procedures. Samples that are stated to have been measured with the ICP-OES are analyzed with a SpectroCiros using standard calibration procedures.

Because of the results from the ICP-MS analysis of the pre-concentrated REEs of the $BaSO_4$ powder (very high Ce concentration), a high-resolution mass spectra scan was carried out for masses 135 to 180 for synthetic barite samples 1.1s, 1.1, 1.2, 1.3 and 1.4 with the Thermo Finnigan XR ICP-MS using standard calibration procedures.

3. Results.

3.1. Optical Microscopy.

All samples consist of large grains of barite, of which the grain boundaries are visible due to the presence of dark phases. Fluid inclusions are possibly present within the grains, but constitute <5% of each sample. Only minor (<5%) accessory phases can be distinguished such as minor pyrite in e.g. sample TR041 and minor mica in sample 1880-318. Some very small dull-grey irregular grains can indicate continental contaminants such as zircon, rutile or apatite which are known to be present in some Archean barites (Ver01d and Ver02 for example; Reimer, 1980). The craters of the LA-ICP-MS ablation are clearly visible in all samples and these holes look very clear, round and with a flat bottom surface. All LA-ICP-MS craters are located in between grain boundaries and away from other phases.

3.2. X-ray Diffraction (XRD).

XRD analysis was performed on the pure rock samples that were grinded into a very fine powder. *Appendix 3* shows all refraction angle versus counts plots with the black line representing real counts, the red line representing counts minus background and the colored lines the supposed mineralogy as indicated in the marginal note. All samples consist mostly of $BaSO_4$ as is indicated by the correlation of the peaks in the spectra with peaks for 'syn' Barite as taken from the International Centre for Diffraction Data (ICDD). The supposed residual mineralogy for samples Ver02, TR041, 1923-19 and 1986-1321 is rather an estimate than a real mineralogy since the minor phases were based on single or only few high amplitudes. The samples that showed different sample powder colors -1923-19 and 1986-1321, pink and brownish respectively - do not show any presence of significant amounts of residual minerals. Instead, the individual barites all show remarkable similar patterns as is shown in *figure 3.1.* (combined data, note the adjusted counts for displaying reasons), mainly suggesting major barite content. This result could validate the proposed method to directly fuse the barite samples without the necessity for performing a time-consuming total digestion, although it must be noted that the XRD analysis has low precision.

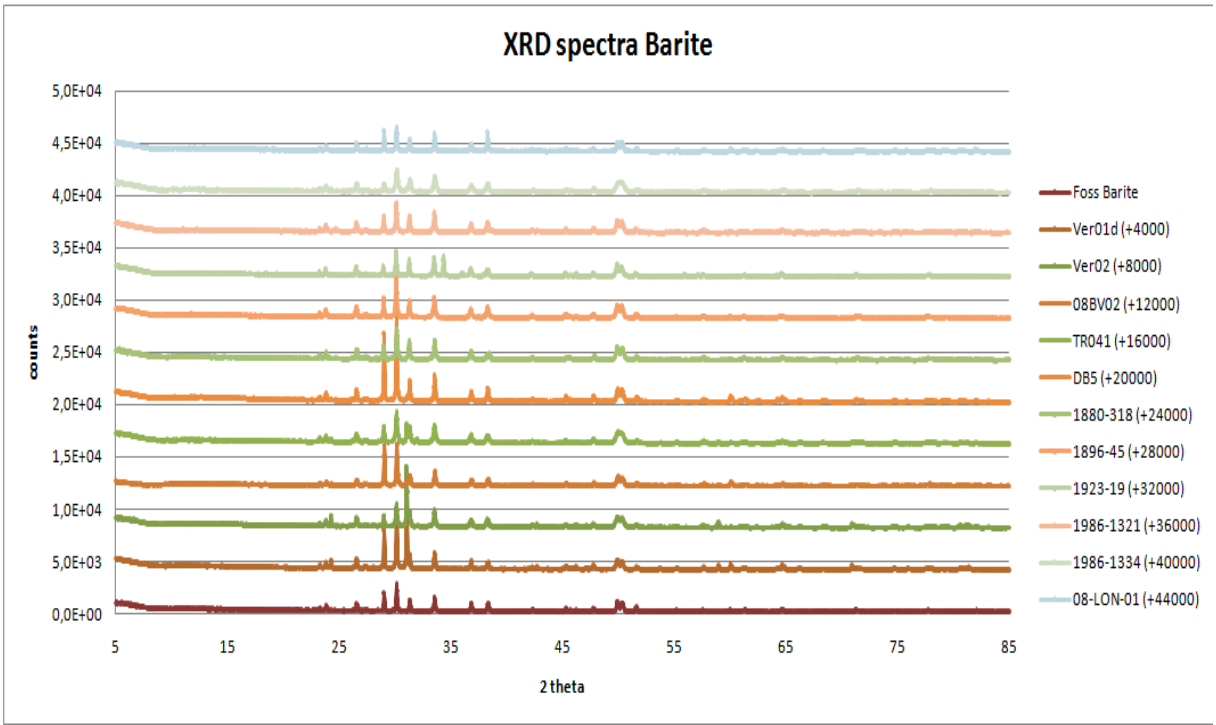

Graph 3.1. Combined XRD data for all samples that are taken into consideration for further research. Note that steps of +4000 are taken in between samples for displaying purposes. For real count values, see Appendix 3.

	Compound wt%						calibration error		Repeat-ability	
sample	Ba (1)	Ba (2)	Sr (1)	Sr (2)	total tield in wt% (1)	total yield in wt% (2)	Ba-cation/S-cation (1)	Ba-cation/S-cation (2)	for Ba	for Sr
Foss Barite		65.7±0.2		**0.22±0.03**		100.54		1.04±0.002		
08-BV-01		64.7±0.5		**0.85±0.45**		100.13		1.03±0.012		
Ver02		65.0±0.2		**0.81±0.03**		100.83		1.02±0.006		
Ver01d		65.1±0.2		**0.89±0.06**		101.04		1.02±0.005		
TR041		64.7±0.3		**0.99±0.05**		100.73		1.01±0.010		
DB05		64.5±0.8		**1.02±0.61**		100.69		1.00±0.022		
08-LON-01		64.3±0.2		**1.30±0.25**		100.75		1.01±0.005		
1880-318	65.9±0.2	65.6±0.2	0.33±0.23	**0.14±0.07**	99.97	99.71	0.98±0.015	1.07±0.013	1.005	2.357
1896-45	63.2±1.3	65.5±0.1	2.1±1.4	**0.12±0.05**	100.16	100.88	1.05±0.022	1.03±0.008	0.965	17.417
1923-19	63.5±1.9	64.6±1.2	2.1±1.9	**0.87±0.88**	100.61	100.84	1.06±0.048	1.01±0.022	0.983	2.368
1986-1321	65.5±0.5	65.2±0.4	0.55±0.34	**0.49±0.31**	101.00	100.98	1.02±0.012	1.01±0.01	1.005	1.122
1986-1334	65.2±1.0	62.8±2.0	0.77±0.79	**2.33±1.71**	100.66	100.81	1.02±0.021	0.98±0.05	1.038	0.330
1883-37	65.9±0.2		**0.12±0.04**		100.77		1.01±0.007			
1902-39	63.7±2.1		**2.1±1.9**		101		1.06±0.044			
1972-8	66.1±0.04		**<d.l.**		100.76		1.00±0.007			
1880-390	64.8±0.2		**0.99±0.04**		100.85		1.03±0.007			
1890-45	65.9±0.1		**<d.l.**		100.72		1.01±0.002			

Table 3.2. Electron Microprobe results of (1) measurement on selected grains, 3-4x each grain and (2) measurements on grains taken into account for further research, 5x each grain. Only compound (BaO and SrO) weight percentage is given, since these values are used for internal calibration of the LA-ICP-MS.

3.3. Electron Microprobe (EMP).

As can be seen in *table 3.2.* the barium compound concentration (in weight%) is very constant at around 65wt% while the Sr elemental concentration (in weight%) can vary within a sample between 0.00 to 2.33wt% in some individual samples (1986-1334). It can be seen that the calibration error (calculated by taking the ratio between the Ba cations and S cations, which is supposed to be 1 in $BaSO_4$) is very low. Together with the yields of the elemental weight percentages that are all around 100%, no further processing of the data was required. It can be seen that the repeatability of the data for Ba for two individual measuring days (1) and (2) is very good, but that for Sr the concentration measured in the same grain varies between different analysis on the same machine, in other words, that the Sr concentration is not homogeneous throughout the sample. Although it would be ideal to use Ba as internal standard for the LA-ICP-MS analysis, it was found that this element was incorrectly measured using this method (see LA-ICP-MS results section). Therefore, Sr was used as internal standard and care was taken that the value with lowest error was used (all values from the 5x each grain (2) measurement, indicated in **bold** in *table 3.2.* The implication of an inhomogeneous internal standard is that all other elements are calibrated to a Sr concentration that is not reliable, resulting in large errors for the resulting REE concentrations. This is especially valid in barite, since the REE concentrations are approximately 100x lower than Sr concentrations and incorrect calibration therefore has a large impact.

3.4. Digestion

3.4.1. Synthetic barite.

It should be noted that it was very difficult (despite the added LiI) to remove the pearls from the holder in the pearl making machine. The fused material had to be manually removed, possibly resulting in contamination. Only part of the pearl was removed, but due to the total melting and the shaking of the sample it was assumed that the pearl was homogeneous in composition.

sample number	[Ba2+] as calculated in powder (in mg)	leaching step	[Ba2+] in supernatant water (in mg)	ratio [Ba2+] supernatant / [Ba2+]powder
1.1	23.3-27.8	A	<d.l.	<d.l.
		B	0.053	2.3E-03 to 1.9E-03
		C	<d.l.	<d.l.
1.2	32.7-39.0	A	<d.l.	<d.l.
		B	0.022	6.8E-04 to 5.7E-04
		C	<d.l.	<d.l.
1.3	37.4-41.2	A	0.004	1.0E-04 to 9.3E-05
		B	0.036	9.6E-04 to 8.7E-04
		C	<d.l.	<d.l.
1.1duplo	19.7-25.1	A	0.003	1.3E-04 to 1.0E-04
		B	0.035	1.8E-03 to 1.4E-03
		C	<d.l.	<d.l.
1.2duplo	30.8-39.4	A	0.001	1.9E-05 to 1.5E-05
		B	0.008	2.7E-04 to 2.1E-04
		C	<d.l.	<d.l.
1.3duplo	40.3-46.2	A	0.006	1.5E-04 to 1.3E-04
		B	0.074	1.8E-03 to 1.6E-03
		C	<d.l.	<d.l.

Table 3.3.. Ratio between [Ba^{2+}] as calculated and the [Ba^{2+}] as measured to be present in the supernatant water from the UHQ leaching steps after grinding of the fusion bead. The two values for calculated [Ba2+] are derived from two ways of calculating the [Ba2+] in the powder: 1) by taking the weight of $BaSO_4$ or 2) by taking the weight after fuse and assuming that all powder is BaO.

Ba^{2+} analysis on the SpectroCirus ICP-OES of the supernatant water of the UHQ leaching steps of the grinded fuse reveals that only a very small fraction of the Ba (and associated REEs) will have been removed during the leaching steps (*Table 3.3.*) After adding 5mL 6N HCl, still some white suspension was present in the Greiner tubes, however, this residue disappeared when a few mL UHQ was added and was therefore assumed to be a soluble carbonate phase. In some cases, after adding UHQ to the grinded fuse, gas bubbles formed and it was therefore necessary to open the lids of the Greiner tubes before centrifuging.

3.4.2. Natural Barites.

Because of the removal problems with the $BaSO_4$ powder during fusing, the cooled fusion bead was directly acquired from the Pt-crucible without collecting it in a pearl-holder. This method possibly avoided contamination and nearly 100% of the pearl could be removed and grinded. No pearl could be made from sample 1923-19, since even after subsequent melting and fast cooling, a substance formed that could not be removed from the Pt-crucible. Approximately 0.5gram of the grinded pearl was taken and subsequently leached with ~150mL UHQ to remove sulfates and nitrates. Of samples Foss Barite, 08-LON-01, Ver01d, DB5 and 1880-318 a duplicate sample of 0.5g powder was taken. Since the results from the $BaSO_4$ powder leaching procedure were showed that very minor Ba was removed during this process, it was not found necessary to analyze the supernatant water of the leaching procedure. Again a white residue formed when 5mL 6N ultrapure HCl was added, but this disappeared after a few mL UHQ was added.

3.5. Ion Exchange Chromatography and Inductively Coupled Plasma Mass Spectrometry

3.5.1. Synthetic barite

In order to be able to test if all Ba^{2+} is transported through the column, an elution curve was constructed for every sample. It was expected that all Ba^{2+} would have been transported through the column without being bonded to the bis(2-ethylhexyl) orthophosporic acid. It can be seen in the graphs (*Appendix 4*) that the Ba^{2+} was continuously eluted as expected for every 50mL solution with a total resolved Ba^{2+} that is consistent with preliminary calculations on the amount of Ba^{2+} present before ion exchange (*Table 3.4.*)

sample	[Ba]total as calculated* (mg)	[Ba]total recovered (mg)
1.1	24.2-23.7	23.3
*1.1***	24.2-23.7	25.1
1.2	31.7-39.2	32.6
1.3	38.8-43.7	33.3

*Table 3.4. Recovered Ba^{2+} during step-wise elution of the 1L bottles (all from the 40mL with 5ppm REE spike analysis, 2.5ppm spike not tested for Ba^{2+}) compared to Ba^{2+} concentrations as expected to be present in the dissolved powder. *: two values because $[Ba^{2+}]$ as calculated varies if $BaSO_4$ starting material is taken for calculation or if BaO as residue is taken for calculation. Note that values differ between table 3.2 and this table, because in this table an average is taken for the [Ba2+] concentration from the sample and the duplicate.**: sample 1.1 is measured twice; spiked and not-spiked with REEs. The spiking of the sample should have only very minor effect on the total recovered Ba^{2+} (5ppm compared to >45000ppm).*

The 1L (5µg REE expected in final 40mL solution) spiked bottles were also eluted in steps such that elution curves could be constructed which can be found in *Appendix 5A*. It can be seen that for the light REEs (lanthanum to holmium) the REEs are eluted in a concave downward pattern, meaning that most REEs are eluted in an early stage. For the heavier REEs the pattern gets more irregular, especially for sample 1.2spike. The total yield was low as can be seen in *table 3.5*. It is thought that this might be due to a limited concentration of REEs that the amount of ester in the cartridge can hold. Therefore, the solutions were spiked again with only 0.5mL REE spike such that 2.5µg REE is expected in the final 40mL solutions. The elution curves for this experiment are shown in *Appendix 5B*. It can be seen that the recovery of all REEs (except lutethium) was more regular. Besides this, the total yield corresponds more to the 2.5µg REE expected, except for cerium which is shown in red in *table 3.5*. However, the yield does not vary

sample	La	Ce	Pr	Nd	Sm	Eu	Gd	Tb	Dy	Ho	Er	Tm	Yb	Lu	Yield (median)
1.1no spike	0.020	6.9	0.01	0.010	<d.l.	<d.l.	0.020	<d.l.	<d.l.	<d.l.	<d.l.	<d.l.	<d.l.	<d.l.	<d.l.
1.1 (5µg)	2.8	6.4	2.8	2.7	2.8	2.8	2.9	2.9	2.9	2.9	2.9	3.1	3.1	2.5	57.6%
1.2 (5µg)	3.8	6.2	3.8	3.7	3.9	3.9	3.9	3.9	3.9	4.0	3.9	4.0	3.4	2.6	78%
1.3 (5µg)	3.8	4.8	3.9	3.8	3.9	3.9	4.0	4.0	4.0	4.0	3.9	3.8	3.2	2.5	78%
1.2 (2.5µg)	2.2	4.7	2.2	2.1	2.2	2.2	2.2	2.2	2.2	2.2	2.2	2.2	1.8	1.4	86.4%
1.3 (2.5µg)	0.72	1.5	1.1	1.2	1.8	2.0	2.1	2.2	2.2	2.2	2.2	2.0	1.6	1.1	76%
1.4 (2.5µg)	2.1	4.6	2.1	2.1	2.2	2.1	2.2	2.2	2.1	2.2	2.2	2.1	1.8	1.4	85.6%

Table 3.5. Rare Earth Element total concentrations in µg in approximately 40mL 6N HCl eluate as measured using the ICP-MS (ThermoFinnigan-Element XR). Cerium concentrations were measured higher than expected and are therefore displayed in red. Because of this, median concentrations are taken for the total yield of the REEs. The total yields are much lower than expected, probably due to amount of ester used and flow speeds of the solution through the cartridge.

much depending on which spike is used and the amount of ester loaded on the cartridge as well as the flow speed of the solution through the cartridge were thus of major importance during the recovery of the REEs. Care is therefore taken in following experiments that as much ester as possible is loaded onto the cartridge and that flow speeds are lower than used before (see methods). The cerium concentration is very high, especially in the first 3 runs (1.1no spike, 1.1 (5µg) and 1.2(5µg)). The variable yields between the samples 1.2(2.5µg), 1.3(2.5µg) and 1.4 (2.5µg) cannot be explained since the influence of amount of ester and flow speed on the process can be large and is unfortunately not measured accurately enough.

As mentioned, the concentration of Ce is very high in all samples and a mass spectrum scan is made for all samples which can be found in *Appendix 6*. Using the relative amplitudes of the counts per second at variable masses the expected cps for Ce at mass 140 (88.48% abundant) is calculated in the following way:

^{145}Nd (8.3% abundant) is the only stable isotope present at mass 145. The cps peak at mass 145 therefore only represents ^{145}Nd (8.3%). The amplitude of this peak is compared to ^{142}Nd (27.2% abundant) via: ^{142}Nd=(27.2/8.3)*^{145}Nd. However, the amplitude of the mass 142 peak consists of ^{142}Ce (11.08% abundant) and ^{142}Nd (27.2% abundant). So ^{142}Ce (11.08%)=total peak at 142 minus (^{142}Nd). To calculate the expected peak for ^{140}Ce (88.48% abundant) the ^{142}Ce is multiplied with (88.48/11.1).

This value is compared with the peak amplitude at mass 140 and it can be seen (*Table 3.6.)* that

sample	calculated Ce-140 peak	observed Ce-140 peak
1.1	5.6	5.8
1.1s	15.6	15.0
1.2s	5.3	5.6
1.3s	3.7	3.9
1.4s	1.6	1.3

Table 3.6. Comparison between the two Ce-140 counts per second as calculated via Nd-145 and Nd-142 and as observed in the High-Resolution Mass Spectrum Scan.

^{140}Ce as calculated is in most cases lower than the observed peak; in other words, ^{140}Ce is truly measured without interference on mass 140 and it thus very high compared to the other REEs. The fact that ^{140}Ce is also very high in the blank sample 1.4s (only Na_2CO_3) leads to the conclusion that the fusing matrix is probably contaminated with Ce. The small differences between the calculated and observed values are most likely due to incomplete measurement of the exact mass 140.12 (Ce).

3.5.2. Natural Barites

The results from the barite eluation of the $BaSO_4$ powder were such that during the Ion Exchange Chromatography process of the natural barites, only the [Ba^{2+}] of the Original 1L solution and of the first 10mL eluate was analyzed by ICP-OES. Using the amount (weight) of powder added to the fuse, it can be calculated how much [Ba^{2+}] should be present in the original. Preferentially, 100% of this barium present should be passed through the C18 cartridge in order to prevent interferences on Eu during ICP-MS analysis. Calculated and measured values of the [Ba^{2+}] can be found in *table 3.7.*, while a schematic represen-

sample	[Ba2+] as expected (in ppm)	[Ba2+] measured in Original sample (in ppm)	[Ba2+] measured in first eluate (in ppm)	$[Ba2+]_{measured}/[Ba2+]_{calculated}$ Original	$[Ba2+]_{measured}/[Ba2+]_{calculated}$ 1st Eluate
Foss Barite	31.7	37.7	36.4	1.2	1.1
Foss Barite duplo	31.8	35.2	35.0	1.1	1.1
Foss Barite TD	30.1	31.8	31.3	1.1	1.0
Foss Barite TD duplo	30.0	31.5	30.5	1.0	1.0
08-BV-01	31.6	33.5	33.1	1.1	1.0
08-BV-01 TD	30.5	32.7	32.0	1.1	1.0
08-BV-01 TD duplo	32.9	32.7	32.0	1.0	1.0
Ver02	30.1	13.6	13.4	0.5	0.4
Ver01d	30.1	16.4	16.3	0.5	0.5
Ver01d duplo	29.0	9.2	9.0	0.3	0.3
TR041	30.7	20.0	20.1	0.6	0.7
DB5	29.5	30.8	30.4	1.0	1.0
DB5 duplo	30.6	30.8	29.9	1.0	1.0
08-LON-01	30.2	30.5	30.1	1.0	1.0
08-LON-01 duplo	29.6	33.4	32.5	1.1	1.1
08-LON-01 TD	33.2	34.6	33.8	1.0	1.0
08-LON-01 TD duplo	32.9	36.6	36.0	1.1	1.1
1880-318	30.6	33.6	32.9	1.1	1.1
1880-318 duplo	29.8	35.4	34.9	1.2	1.2
1896-45	30.1	33.9	32.8	1.1	1.1
1986-1321	29.4	26.0	25.8	0.9	0.9
1986-1321 TD	29.3	33.3	32.5	1.1	1.1
1986-1334	30.1	34.4	33.3	1.1	1.1

Table 3.7. Barium concentrations as calculated from the amount of powder added and as measured with the SpectroCiros ICP-OES for the 'Original' solution in the 1L Nalgene bottles and the first eluate after attachment of the SepPak C18 cartridge. A ratio is shown for easy comparison between the calculated and measured values. The values in red (Ver02, Ver01d, Ver01d duplo and TR041) all show ratio<1, which means that a lower [Ba^{2+}] is eluated or/and present in the original solution than expected from the amount of powder added.

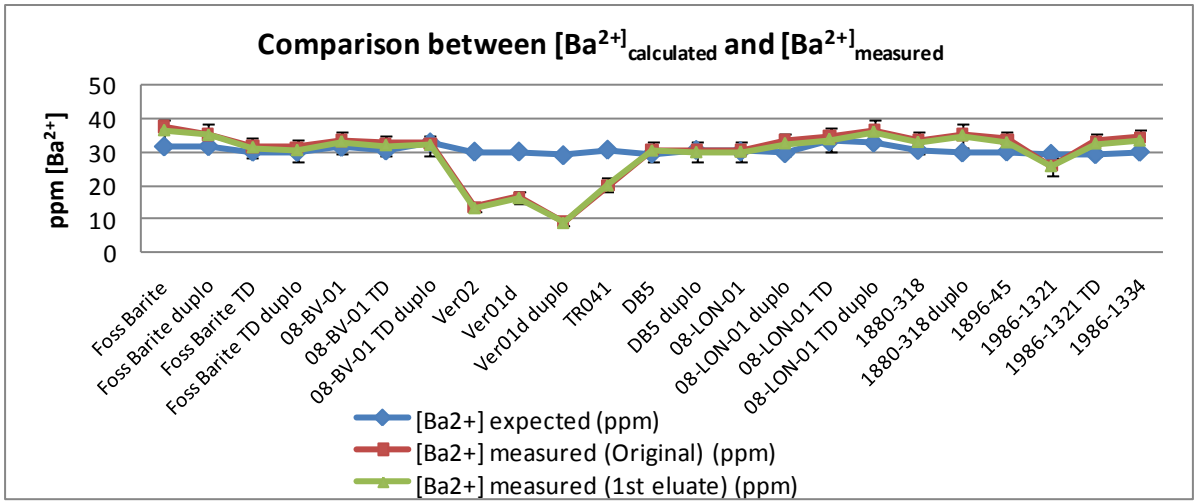

Figure 3.8. Graphical representation of the differences between the expected [Ba^{2+}] concentrations from calculations on the amount of powder dissolved and the measured [Ba^{2+}] concentrations from ICP-OES analysis. The error bars indicate a +5% and –5% error range.

tation of the calculated and actual concentrations (*Figure 3.8*) shows that for all samples except Ver01d and Ver02, the concentration in the 1L solution is as calculated. Although samples Ver01d and Ver02 show lower Ba^{2+} concentrations, it can be seen in both the table and the graph that all Ba^{2+} present in the Original solution is recovered during the Ion Exchange process and thus separated from the REEs. The concentration in mg/L (ppm) is considered and corrected for the deviations of 1L of the eluate solutions, since the data from the ICP-OES is given in ppm and the exact dilutions were unclear.

Natural Barites - REE elution.

The results from the Ion Exchange Chromatography solution analysis would be referred to as 'ICP -MS' data, while the results from the in situ LA-ICP-MS analysis is further referred to as 'LA-ICP-MS' data.

The results of the REE elution can be found in *Appendix 7* which shows the elution of all elements for sample TR041 and the accompanying problems in eluting not all of the spiked Pr and Yb and the irregularities in eluting the HREEs. The ICP-MS data of all natural barite samples, the duplicates and the total digested samples with accompanying duplicates was corrected for lower detection limits for which a value of 3sigma (theoretical detection limit) was taken. After the correction, the results were calculated back to the concentration as which would have been present in the natural rocks and corrected for yield. These concentrations can be found in *table 3.9.* The concentrations are normalized to Post Archean Average Shale (Nance and Taylor, 1976) and Chondrite (Anders and Grevesse,

	Pr yield in %	Yb yield in %
TR041	no data	81.0
1986-1334	76.7	75.8
Ver01d	66.4	66.5
1896-45	82.6	77.4
Foss Barite	81.1	77.1
08-LON-01	74.0	73.9
Ver02	75.3	71.2
Ver01d duplo	78.2	82.3
1986-1321 TD	81.9	80.2
DB5 duplo	82.8	67.7
08-LON-01 duplo	90.3	74.5
08-LON-01 TD duplo	97.9	83.3
1880-318	96.7	82.7
08-BV-01	71.6	63.5
08-LON-01 TD	93.8	71.3
DB5	91.0	75.6
1986-1321	170.2	128.3
Foss Barite TD duplo	96.8	65.5
08-BV-01 TD duplo	93.2	54.9
1880-318 duplo	109.9	68.5

Table 3.10. Obtained yield for the Ion Exchange Chromatography process as obtained from Pr and Yb spike.

All in ppm	La	Ce	Nd	Sm	Eu	Gd	Tb	Dy	Ho	Er	Tm	Lu
TR041	2.578	4.835	2.154	0.452	0.165	0.455	0.097	0.373	0.095	0.235	0.060	0.095
1986-1334	2.593	3.540	1.039	0.268	0.109	31.856	0.038	0.083	0.017	0.020	0.013	0.040
Ver01d	0.678	1.022	0.272	0.084	0.033	33.328	0.039	0.061	0.030	0.037	0.016	0.051
1896-45	0.112	0.340	0.025	0.016	<d.l.	29.796	0.016	<d.l.	<d.l.	<d.l.	0.005	0.026
Foss Barite	1.365	2.655	0.512	0.068	0.094	29.058	0.013	0.049	0.008	0.007	0.004	0.012
08-LON-01	0.588	0.811	0.148	0.026	0.131	31.334	0.010	0.025	<d.l.	0.010	0.003	0.008
Ver02	0.819	2.281	0.273	0.044	0.016	28.986	0.011	0.036	0.007	0.026	0.003	0.004
Ver01d duplo	0.474	0.737	0.177	0.031	0.009	29.052	0.010	0.030	0.004	0.014	0.002	0.010
1986-1321 TD	0.713	1.720	0.502	0.071	0.030	29.483	0.012	0.021	0.004	0.009	<d.l.	0.009
DB5 duplo	1.052	0.912	0.079	0.012	0.006	28.464	0.006	<d.l.	<d.l.	<d.l.	<d.l.	<d.l.
08-LON-01 duplo	0.562	0.751	0.109	0.020	0.104	29.674	0.008	0.049	<d.l.	<d.l.	0.006	<d.l.
08-LON-01 TD duplo	0.230	0.092	<d.l.	<d.l.	0.031	25.443	<d.l.	0.008	<d.l.	<d.l.	<d.l.	<d.l.
1880-318	0.409	1.648	1.498	0.377	0.178	30.222	0.061	0.419	0.065	0.172	0.010	0.013
08-BV-01	1.674	3.066	0.883	0.137	<d.l.	27.689	0.019	0.128	0.018	0.041	0.006	<d.l.
08-LON-01 TD	0.219	0.082	0.032	0.016	0.047	27.540	0.018	0.024	0.013	<d.l.	0.023	0.011
DB5	1.085	0.905	0.103	0.041	0.021	31.942	0.007	0.029	0.006	0.009	0.005	<d.l.
1986-1321	0.480	2.477	1.484	0.594	0.433	31.500	0.159	0.376	0.108	0.174	0.098	0.081
Foss Barite TD duplo	0.900	1.189	0.412	0.034	0.036	32.081	0.011	0.042	<d.l.	<d.l.	0.011	<d.l.
08-BV-01 TD duplo	0.852	1.092	0.369	0.011	<d.l.	32.517	<d.l.	0.022	0.010	<d.l.	0.005	<d.l.
1880-318 duplo	0.497	1.831	1.903	0.403	0.254	34.555	0.067	0.442	0.082	0.219	0.012	<d.l.

Table 3.9. ICP-MS obtained REE concentrations after Ion Exchange Chromatography.

1989) and the resulting REE plots can be found in *Appendix 8A and 8B*. Since Gd displays very high values (also when normalized—see *discussion*), this element is will not be discussed further. Because of the Pr and Yb spikes in the Ion Exchange method, these two elements are not plotted in the REE patterns. However, a yield for the Ion Exchange Process can be calculated from these two elements which is shown in *table 3.10*. It should be noted for these two elements that the concentration as derived from the ICP-MS has an error >10% and is therefore uncertain. The mean yield is taken for back-calculations of the concentration REEs in the rocks.

As can be seen in the PAAS-normalized REE graphs as well as in the Chondrite-normalized graphs, nearly all duplicate samples show equal REE patterns as the original samples, except for 1986-1321 and 08-LON-01 TD duplicate. There is a variation in $(La/Lu)_{PAAS}$ values which is given in *table 3.11* and which is more pronounced for the Chondritic normalized values, because the PAAS normalization values have +VE anomalies for the LREEs when normalized to Chondrite (*Figure 3.12*)

	La/Lu (PAAS)	La/Lu (Chondrite)
TR041	0.36	2.55
1986-1334	0.86	6.15
Ver01d	0.17	1.24
1896-45	0.06	0.41
Foss Barite	1.53	10.89
08-LON-01	0.99	7.03
Ver02	2.72	19.40
Ver01d duplo	0.63	4.48
1986-1321 TD	1.08	7.68
DB5 duplo	>1	>1
08-LON-01 duplo	>1	>1
08-LON-01 TD duplo	>1	>1
1880-318	0.43	3.03
08-BV-01	>1	>1
08-LON-01 TD	0.26	1.87
DB5	>1	>1
1986-1321	0.08	0.55
Foss Barite TD duplo	>1	>1
08-BV-01 TD duplo	>1	>1
1880-318 duplo	>1	>1

Table 3.11. La/Lu ratios for the ICP-MS analysis after Ion Exchange Chromatography. For more detail on the REE patterns, see section 4. Discussion.

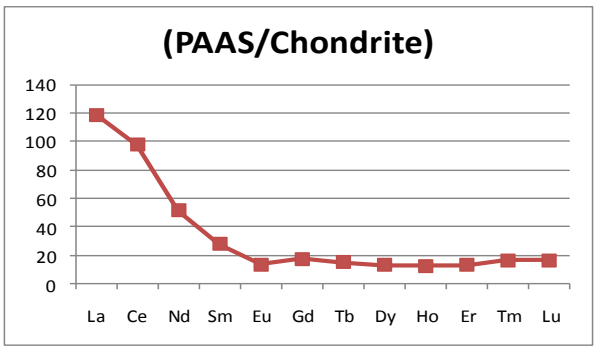

Figure 3.12. PAAS normalization values over Chondrite normalization values to show that PAAS normalization effects the LREE relatively more than the HREEs, resulting in higher normalized LREE abundances when normalizing to Chondrite. This is observed in the data.

Since the Na_2CO_3 that was used for fusing was contaminated with Ce and since Pr is taken as spike in the ICP-MS dataset, no Ce anomaly could be calculated for the ICP-MS results. The Eu anomaly could be calculated in two ways (Eu/Sm) and as $(Eu/Eu^*)_{PAAS}=(Eu_{PAAS}/(0.67Sm_{PAAS}+0.33Tb_{PAAS}))$ for the ICP-MS data and this results in a +VE anomaly except for 1896-45, (Ver01d (0.99 for $(Eu/Eu^*)_{PAAS}$) and 08-BV-01. The Eu anomaly is calculated in the same manner for the Chondrite normalized data. Since there is still minor Ba^{2+} present after the Ion Exchange Chromatography, it is checked whether or not this has an influence on the +VE Eu anomaly as observed. As can be observed in *figure 3.13* there is no obvious relationship between Eu anomaly and the presence of Ba in the solution.

In order to qualitatively check the LA-ICP-MS measurements (see following section), graphs are constructed which show the REE patterns for PAAS normalization (*Appendix 9A*) and the REE patterns for Chondrite normalization (*Appendix 9B*) for both methods in one graph. For quantitative control, the LA-ICP-MS PAAS normalized data was plotted against ICP-MS PAAS normalized data for a selection of elements to see if a linear relationship was obtained (*Appendix 10*). As can be seen in these graphs, any linear rela-

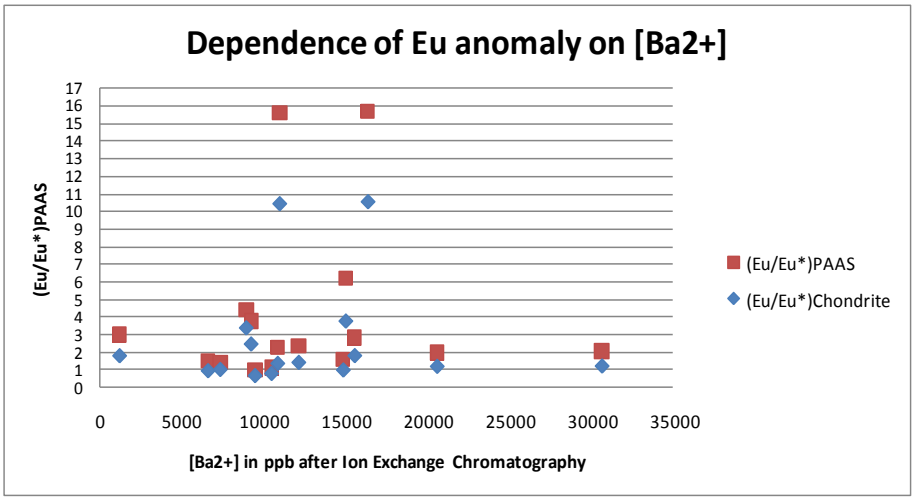

Figure 3.13. Graph of the calculated Eu anomaly against Ba^{2+} concentration (in ppb) present in the solution after Ion Exchange Chromatography. No relation can be observed, arguing for the theory that the small amounts of Ba still present have no significant effect on Eu abundances in the form of BaO interferences.

tionship is absent for this selection of elements. The results of this qualitative and quantitative control are further discussed in *section 4.*

3.6. Laser-Ablation Inductively Coupled Plasma Mass Spectrometry (LA-ICP-MS)

The REE abundances (*Table 3.14*) that are derived from the LA-ICP-MS method are normalized to PAAS and Chondrite of which the results can be found in *Appendix 11A and 11B.* Since it was expected that Eu would not be correctly measured due to BaO interferences, this element is only measured in some samples and anomalies are calculated in the same manner as with the ICP-MS, resulting in a total calculated Eu anomaly as discussed in *section 4. Discussion.* Tm is measured only in some samples as well and it can be seen that where it is measured, both PAAS as well as Chondrite normalized abundances show a large +VE anomaly. Also the Gd +VE anomaly is very distinct in all samples, however, the amplitude of the anomaly is lower compared to the ICP-MS Gd abundances after Ion Exchange Chromatography. The Ce anomaly is calculated as $Ce=(Ce_{PAAS}/(0.5Pr_{PAAS}*0.5La_{PAAS}))<1$ **and** $Pr=(Pr_{PAAS}/(0.5Ce_{PAAS}*0.5Nd_{PAAS}))>1$ (*Figure 3.15.*). However, as can be seen in both the LA-ICP-MS as well as the ICP-MS PAAS normalized abundance REE patterns, Nd behaves anomalous in a variety of samples. The $(Sm/Nd)_{PAAS}$ ratio is calculated and it can be seen in *figure 3.16* that a -VE Nd or +VE Sm anomaly is found with both measurement techniques for all samples except Foss Barite, Ver02, 08-BV-01 and an anomaly is found for only one measurement technique for samples 08-LON-01 and 1880-318. These anomalies of Nd or Sm cannot be explained by interferences (Dulski, 1994) but influences the calculation of the –VE Ce anomaly. For all samples except Foss Barite, Ver02 and 08-BV-01 the calculated –VE Ce anomaly must be taken as uncertain.

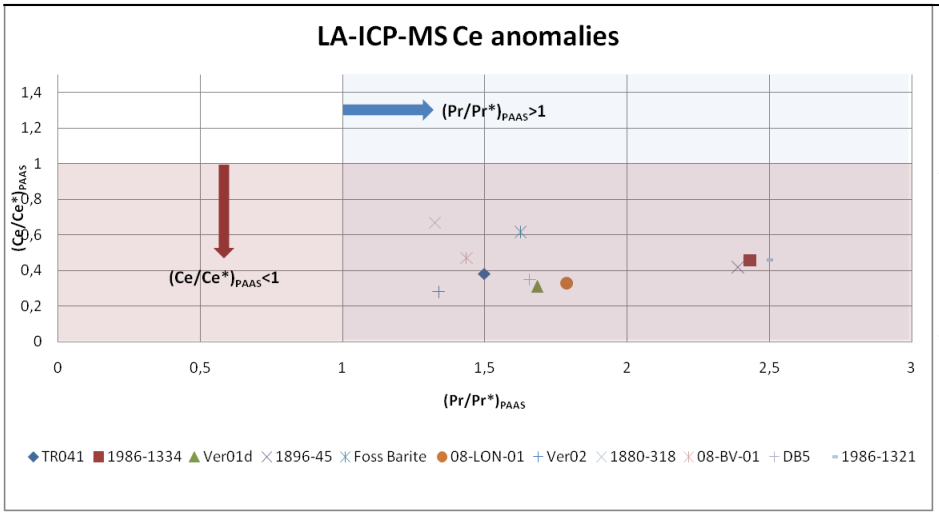

Figure 3.15. Ce anomaly calculated as described in the text. It can be seen that all samples fall within the dark field that represents $(Pr/Pr^*)_{PAAS}>1$ and $(Ce/Ce^*)_{PAAS}<1$. Ce anomalies could only be calculated from the LA-ICP-MS results and cannot be calibrated against ICP-MS results.

All in ppm	La	Ce	Pr	Nd	Sm	Eu	Gd	Tb	Dy	Ho	Er	Tm	Yb	Lu
TR041	0.033	0.010	0.020	0.017	0.034		0.045	0.019	0.014	0.012	0.011		0.016	0.018
1986-1334	0.003	0.002	0.006	0.003	0.017	0.075	0.025	0.010	0.005	0.006	0.005	0.012	0.007	0.009
Ver01d	0.036	0.010	0.026	0.021	0.047		0.058	0.025	0.018	0.012	0.014		0.021	0.017
1896-45	0.143	0.085	0.266	0.137	0.629	4.355	0.568	0.264	0.177	0.148	0.169	0.390	0.193	0.293
Foss Barite	0.041	0.023	0.034	0.018	0.064	0.468	0.076	0.023	0.017	0.017	0.015	0.038	0.019	0.033
08-LON-01	0.037	0.011	0.033	0.025	0.059		0.098	0.030	0.020	0.015	0.019		0.023	0.027
Ver02	0.042	0.014	0.056	0.070	0.314		1.640	0.270	0.315	0.175	0.500		0.165	0.240
DB5 duplo	0.071	0.020	0.041	0.030	0.065		0.101	0.036	0.024	0.020	0.022		0.028	0.028
1880-318	0.030	0.054	0.133	0.146	0.151	0.427	0.074	0.035	0.028	0.027	0.017	0.035	0.020	0.035
08-BV-01	0.062	0.026	0.046	0.039	0.081		0.097	0.047	0.039	0.029	0.030		0.036	0.023
DB5	0.071	0.020	0.041	0.030	0.065		0.101	0.036	0.024	0.020	0.022		0.028	0.028
1986-1321	0.008	0.006	0.020	0.010	0.048	0.339	0.072	0.032	0.013	0.020	0.014	0.035	0.018	0.033

Table 3.14. REE concentrations in the barite rocks as obtained from LA-ICP-MS analysis. Sr-87 is taken as internal standard.

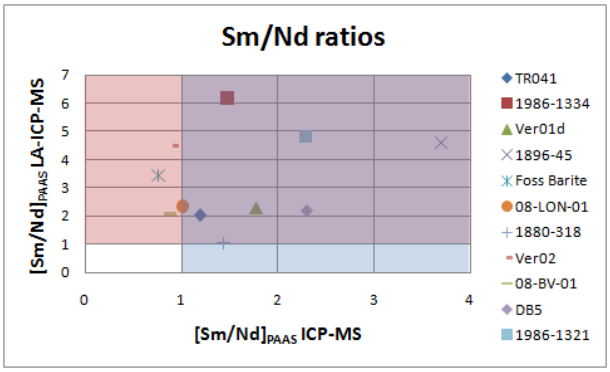

Figure 3.16. Sm/Nd ratios for barite of the ICP-MS analysis versus the LA-ICP-MS analysis. The dark field represents a true -VE Nd or +VE Sm anomaly as measured by both techniques. This anomaly can influence the Ce anomaly as calculated from the LA-ICP-MS technique.

As mentioned in the methods section, some samples were measured several times by the LA-ICP-MS method on different occasions. A consistency check is performed on the mean abundances for various REEs, which values can be found in *table 3.17*. It can be seen that the repeatability of the LA-ICP-MS analysis is very poor and that this has to be taken into account when discussing the results.

	1923-19	08-BV-01	1986-1334	1986-1321
La	0.74	1.99	7.90	3.20
Ce	0.34	0.99	4.85	2.33
Pr	0.34	0.64	4.07	2.26
Nd	0.45	0.48	6.02	3.28
Sm	0.29	0.12	2.87	2.54
Gd	0.59	0.01	14.66	6.62
Tb	0.42	0.12	3.39	1.47
Dy	0.27	0.15	4.16	3.60
Ho	0.32	0.04	6.65	2.86
Er	0.22	0.06	7.54	2.46
Tm	No data	No data	No data	No data
Yb	0.37	0.04	5.73	3.49
Lu	0.32	0.03	6.16	2.92

Table 3.17. Ratio between MEAN abundances for REEs for two different measurements on the LA-ICP-MS. In the ideal case, this ratio is 1, implying a good repeatability for the LA-ICP-MS analysis. In this case, the repeatability is poor.

4. Discussion.

4.1. Potential of measuring REEs in $BaSO_4$ by LA-ICP-MS.

Although expected to serve as a reliable paleo-proxy for temperature and redox conditions during chemical precipitation of $BaSO_4$, analysis of REE abundances and the presence of Ce and Eu anomalies in barite has been limited to only a few publications in the past (Guichard, 1979; Barrett et al; 1995). The method for REE analysis in barite as developed in this research provided a way to overcome limitations such as expensive Neutron Activation Analysis characterized by poor accuracy and precision and to minimize analysis errors due to interferences of BaO on Eu -153. The Ion Exchange Chromatography procedure to remove Ba^{2+} and other major cations from solution as proposed by Winchester (1963) and Shabani et al (1992) was carefully adjusted for the anomalous high Ba^{2+} concentrations of dissolved $BaSO_4$ using 98% pure synthetic barite. Since it was expected that REE concentrations in barite would be very low, it was important to be able to dissolve significant amounts of barite. It was found that the method as proposed by Barbieri et al in 1982 using Na_2CO_3 fuse was able of dissolving at least 0.5grams of barite in 5mL 6N HCl. A fuse ratio between $BaSO_4$ and Na_2CO_3 of 1:10 appeared to give the best results shown by Ba elution calculations. However, a problem that arose during this process was that Na_2CO_3 was contaminated with significant amounts of Ce, limiting the reliable analysis of this element using the Ion Exchange Chromatography method. Leaching with UHQ and reaction of the supernatant fluid with $BaCl_2$ showed that all Sulfates were removed during the fusing, resulting in a complete dissolution of the Ba-REE oxide cake in 5mL 6N HCl. It was shown that the usage of Sep-Pak C18 cartridges for Ion Exchange Chromatography resulted in near 100% removal of interfering Ba and significant recovery of REEs.

Since the quantitative comparison plots of the ICP-MS data versus LA-ICP-MS data show a lot of scatter and no obvious linear relationship between the two measurement methods, it appears that the two analysis techniques are not in agreement. However, when looking at the qualitative comparison graphs, some similarities can be seen for some samples, and therefore, these plots will be described in more detail in this section.

Foss Barite, Aberfeldy, UK.

The PAAS normalized REE abundance patterns show that there is a relatively minor offset in abundances between the LA-ICP-MS and the ICP-MS data especially for the LREEs. Only Er and possibly Tm show anomalous behavior between two methods. In general, the sample that has undergone a Total Digestion (TD) has lower HREE and Ce abundances than the original sample. This can be due to removal of phases containing HREEs and Ce during the total digestion procedure. Note that the LA-ICP-MS pattern is similar in both graphs since LA-ICP-MS analysis was only performed *in situ* on natural rock samples. The REE abundance pattern is relatively flat for both measurements showing +VE Eu anomalies in both cases, slight –VE Ce anomalies for the LA-ICP-MS and the TD ICP-MS data and a concave pattern for La to Sm and for Tb to Lu (especially for the ICP-MS data). The similarity of both graphs can be due to the homogeneity of the Foss Barite sample as is also shown by sulfur isotope analysis (*Desiree Roerdink, pers comm.*). Both methods seem to work approximately correct for the homogeneous Foss Barite sample. The implications of this with respect to the geology and environments of formation will be discussed in *section 4.4*.

1880-318, Alston Moore, UK.

For sample 1880-318 it can be seen that the LREEs (La to Eu) show a relative similar pattern for both analysis techniques with a constant offset even when corrected for yield (82-96% for the ICP-MS analysis). It is remarkable that the LREEs have a larger abundance when measured by the LA-ICP-MS as expected, but that the MREEs to HREEs (Gd to Er) have lower abundances when measured by the LA-ICP-MS. Lu displays a higher abundance for LA-ICP-MS analysis than expected. Since this feature is consistent for both samples, it can be assumed that this

pattern results from rock properties rather than from analysis error. Since the ICP-MS analysis represents more of a bulk rock analysis than the LA-ICP-MS analysis—which was carried out on selected spots high in $BaSO_4$ as observed under the microscope—it is possible that there are phases present in the sample that are enriched in HREEs. This should be tested by carrying out a total digestion of sample 1880-318, thereby removing accessory phases such as calcites, carbonates, silicates and fluid inclusions or by performing more detailed optical microscopy and Electron Microprobe analysis. Since Eu corresponds well within the two analysis techniques, this elements can be used for anomaly calculation. For the –VE Ce anomaly it should be questioned if the presence of the slight +VE Sm or –VE Nd anomaly affects the calculated value. The implication of the anomalies present is further discussed in *section 4.4.*

1986-1321. Bad Grund deposit, Harz Mountains, Germany.

For the original sample both techniques show an constant offset especially for the LREEs, while for the total digested sample the MREEs and HREEs (Nd to Lu) seem to be removed from solution. This can point towards the presence of accessory minerals enriched in MREE and HREE and results in higher LA-ICP-MS abundances of all REEs for the total digested sample. For La and Ce the data seems to corresponds better, and therefore a –VE Ce anomaly might be valid for this sample. However, the Sm/Nd ratio is >1 for both techniques, implying that the –VE Ce anomaly might not be calculated right. The sample shows La/Sm<1 especially visible in the LA-ICP-MS data and again a concave pattern for the HREEs with large relative Lu enrichments. Although Eu is part of the REEs with much lower measured abundances in the Total Digested ICP-MS sample, the relative +VE Eu anomaly can be distinguished in the total digested sample and is exactly similar in the original sample for both analysis techniques and is therefore assumed to be real.

DB5, Western Australia.

Sample DB5 shows larger PAAS normalized REE abundances for the LA-ICP-MS process than for the ICP-MS analysis even when corrected for the expected lower yield of the ICP-MS process. In both the original sample as in the duplicate, La and Ce show equal offsets between the techniques. Tb, Ho and Dy show equal offsets for both techniques in the original samples, but were much less abundant in the ICP-MS solutions of the duplicate. Nd shows a large difference between the LA-ICP-MS results and the ICP-MS data, being much more abundant in the LA-ICP-MS data. It is unclear where this difference is derived from, since interferences with oxides should result in larger abundances in the ICP-MS data rather than in the LA-ICP-MS data. Because of this Sm/Nd>1 ratio, the calculated –VE Ce anomaly for the DB5 samples should be taken as uncertain. Since Eu is only measured by the ICP-MS technique, the +VE anomaly acquired by this technique should also be considered as uncertain and should be cross-calibrated against other parameters for environment of formation in this rock to be indicated as real or not.

Ver01d. Barberton Greenstone Belt, South Africa.

The PAAS normalized REE abundance graphs show very flat patterns for both analysis techniques. The duplicate shows a regular offset between the two measurement techniques for La, Nd, Tb, Dy, Ho and Er. However, the original sample looks more irregular and has higher Tb and Ho abundances in the ICP-MS analysis. It should be tested to see if this feature is derived from analysis errors rather than from rock composition by repeated measurements of this sample. The absence of a Ce anomaly in the ICP-MS results is clear in this sample and is derived from the contamination of the Na_2CO_3 with Ce as indicated by the synthetic barite experiments. Since La and Nd seem to be accurately measured by both techniques, the –VE Ce anomaly acquired from the LA-ICP-MS technique could be taken as real. However, Nd displays an -VE anomaly for both techniques in this barite compared with Sm and this anomaly can better be taken as uncertain. Given that the duplicate sample seems to give the best results, the Lu enrichment and the accompanying concave pattern for the HREEs is again very distinct for the ICP-MS analysis. It is unclear which process causes this concave pat-

tern. The +VE Eu anomaly as calculated from the ICP-MS results cannot be calibrated against LA-ICP-MS analysis and should be taken as uncertain.

1986-1334, Sieberthal, Harz Mountains, Germany.

Sample 1986-1334 is one of a few samples in which the ICP-MS results have higher abundances than the LA-ICP-MS analysis when corrected for the lower yield of the ICP-MS analysis. Since it is expected that the LA-ICP-MS results in REE yield higher than the ICP-MS analysis due to limitation of contamination and loss, this high abundance in the ICP-MS data can be derived from anomalous low yield of the LA-ICP-MS analysis. However, since no external standard was available to calculate yields for the LA-ICP-MS process, this is a hypothesis that has to be verified in the future. The two analytical techniques show a regular offset for the LREEs La, Ce and Nd and also a different but regular offset for the HREEs Tb to Lu. The Sm/Nd ratio is >1 and therefore the calculated –VE Ce anomaly should be taken as uncertain. The exception for the latter offset is Er which has an anomalous low abundance in the ICP-MS data. It is unclear which step in the Ion Exchange Chromatography method would produce a loss of Er in the solution. Furthermore, sample 1986-1334 together with 1986-1321 are the only samples for which the ICP-MS and LA-ICP-MS give equal Eu concentrations. For sample 1986-1334 this could mean that Eu is measured correctly by both techniques, regardless of the amount of Ba still present. However, the Total Digested sample 1986-1321 shows a removal of Eu, indicating that the +VE Eu anomaly could be derived from an accessory phase.

08-LON-01. Barberton Greenstone belt, South Africa.

This sample is the only sample that comprises a whole set of originals, duplicates, total digested sample material and the duplicate of this latter procedure. La and the HREEs of the original sample seem to display an equal offset between the two techniques with the abundances all higher for the LA-ICP-MS even after correcting for lower yield of the ICP-MS analysis. Nd and especially Sm show larger offsets with both techniques and a Sm/Nd ratio>1 for the LA-ICP-MS technique and Sm/Nd ratio = 1 for the ICP-MS technique. The absence of a –VE Ce anomaly in the ICP-MS data is due to the contamination of the fusing material, but since Nd or Sm seem to display anomalous behavior, the anomaly has to be taken as uncertain. It can be seen that especially for the TD duplicate sample all of the HREEs are removed during total digestion. However, since the HREE abundances for all four samples give totally variable abundances, this set of isotopes is probably not measured reliable. It is unclear what causes this difference. The Eu anomaly as derived from the ICP-MS analysis cannot be calibrated against LA-ICP-MS results and should be taken as uncertain.

Ver02, Barberton Greenstone belt, South Africa.

The sample from Ver02 shows a rough but equal correlation between the MREEs to the HREEs between the two analysis techniques, however, the huge difference between the abundances of the ICP-MS and the LA-ICP-MS even after yield correction is striking. Both La and Nd show smaller offsets and the normalized abundances for Ce are the opposite of the rest of the abundances. This +VE Ce anomaly as displayed in the ICP-MS data is not explained by larger amounts of Ce-contaminated Na_2CO_3 present, since the ratio of $BaSO_4$ to Na_2CO_3 is not much different than for the other samples (*table 2.3.*) and can be derived from analysis error. The –VE Ce as calculated from the LA-ICP-MS must therefore be considered as uncertain, since it cannot be calibrated with ICP-MS results and since La/Nd shows opposite trends for both measurements. The Sm/Nd ratio is <1 for the ICP-MS technique and >>1 for the LA-ICP-MS technique indicating anomalous behavior of one of these elements. Also the Eu anomaly cannot be calibrated and therefore it can be concluded that this sample is not very suitable to use as proxy to put constraints on Archean ocean and atmosphere conditions.

TR041, Stentor farm, South Africa.

The TR041 sample is one of the few samples in

which the PAAS normalized abundances are lower for the LA-ICP-MS than for the ICP-MS. This can be explained by 1) assuming that the yield from the LA-ICP-MS analysis was lower than that of the ICP-MS analysis or 2) that many accessory phases were present in the bulk ICP-MS solution high in all REEs. The process of total digestion has to be performed on this sample to make a distinction between these two explanations. Although the ICP-MS pattern is much flatter, two concave patterns with relative La, Sm and Lu enrichments are present in both datasets. Since La and Nd show variable offsets between the two datasets, the calculated –VE Ce anomaly in the LA-ICP-MS data should be taken as uncertain. Eu can not be calibrated by LA-ICP-MS data and the reliability of the +VE anomaly as proposed by the ICP-MS method is therefore also questionable.

1986-45. Sellafield, Frizington area, Cumberland, UK.

The lack of data for the ICP-MS analysis of this sample makes it very hard to draw conclusions on the reliability of the analysis methods for this sample. The ICP-MS data are relatively constant lower in abundance than the LA-ICP-MS data, even when corrected for low ICP-MS yields. It can be seen in this sample that the –VE Ce anomaly as measured by the LA-ICP-MS is less than –VE Ce anomalies in other samples and that the Ce contamination of the fuse overcomes this anomaly in sample 1986-45 resulting in a +VE ICP-MS Ce anomaly, while in other samples ICP-MS Ce is neither +VE or –VE. Therefore, it can be concluded that the Ce anomaly as measured by the LA-ICP-MS is a more realistic –VE anomaly. Again, the LA-ICP-MS data shows concave patterns with LREE, MREE and HREE enrichments, a feature that is probably due to crystallographic effects during incorporation of the REE in the $BaSO_4$ lattice. The Eu anomaly as indicated by the LA-ICP-MS data can not be verified and should be taken as uncertain.

08-BV-01. Barberton Greenstone belt, South Africa.

Probably the sample with the lowest correlation between the two analysis techniques is sample 08-BV-01. The total abundances of the acid digested sample (ICP-MS) are very low, probably because a phase rich in REEs such as monazite was removed during this process. Because of the larger abundance of LREEs compared to HREEs in natural environments, removal of a phase rich in all REEs will result in HREE concentrations below detection limits. La and Nd seem to correspond between the two samples and display an equal offset between the two techniques. The –VE Ce anomaly as found in the LA-ICP-MS data can therefore be taken as a true anomaly. Both the MREEs and the HREEs are inconsistent between the two samples, the cause of this should be derived from multiple analysis of this sample. Eu is not measured or detected in both techniques, sample 08-BV-01 can therefore not be taken as a proxy for environment of formation.

Summarizing; for nearly all samples except TR041, 1986-1321 and 1986-1334 the REE concentrations as measured by LA-ICP-MS are higher than the REE concentrations obtained from Ion Exchange Chromatography and ICP-MS analysis. Gd shows a +VE anomaly in all samples in both analytical techniques. A –VE Ce anomaly is also found in all samples, together with a +VE Eu anomaly. However, these anomalies are uncertain in all cases, since the minor Ba present after Ion Exchange Chromatography could cause the +VE Eu anomaly in the ICP-MS samples and the –VE Ce anomaly as observed in the LA-ICP-MS samples cannot be calibrated against ICP-MS data. The result of total digestion of the barite rock powder is REE removal in all cases, often resulting in REE concentrations below detection limits, especially for the HREEs.

From these results a preliminary conclusion can be made that it is yet unclear if the determination of REEs in barite by the usage of LA-ICP-MS is reliable, since the Ion Exchange Chromatography method and accompanied ICP-MS analysis leaves a lot of questions unsolved. An additional check for the proposed anomalies that were calculated from the LA-ICP-MS method and thus for the reliability of the method itself would be the comparison with existing data on geology. This is discussed in the next section.

4.2. Geochemical implications of the REE abundances in barite - low versus high T precipitation of Archean and Phanerozoic barites: comparison of REE abundances with geology.

In this section, the obtained REE abundances and the observed Eu and Ce anomalies (where present) are compared with knowledge on geology and environment of formation as obtained from other parameters described in *section 1.5.* The comparison of the environment of formation as obtained from other parameters with the observed REE abundance patterns serves as another check for the reliability of this REE determination method. It should be noted, however, that the geology of the young barite deposits is often not well constraint and that information on environment of deposition of the samples is only a hypothesis. The consistency between obtained REE patterns and the observed REE abundances in the other rocks is used to deliberate on the possible temperature and redox state of the environment during barite precipitation in the Barberton Greenstone belt. Furthermore, the problem is that the younger barites used for comparison with the Archean barites only comprise barites that are 1) formed from complex brines in the subsurface or 2) formed from high-T expelled fluids in hydrothermal black/white smoker systems. The absence of low-T marine precipitated barite makes it difficult to use Eu as a T indicator, since both environments of formation mentioned before are expected to result in a +VE Eu anomaly a no comparative material with –VE Eu anomalies is present.

Foss Barite. Aberfeldy, Scotland.

The massive barite beds of the Foss barite deposit are thought to be formed during a climax in hydrothermal activity where a white smoker expelled Ba-rich brines to sulfide-rich seawater (Willan and Coleman, 1983). The PAAS normalized REE abundance patterns show La/Lu>1 (but in more detail a concave pattern for the LREEs and for the HREEs separately) large +VE Eu anomalies and –VE Ce anomalies in the LA-ICP-MS data. Both anomalies are consistent with a high-T, reduced fluid (+VE Eu anomalies) that comes into contact with seawater that shows a –VE Ce anomaly due to oxidative scavenging of Ce (IV)O_2 from the marine environment.

1880-318. Alston Moore, Cumberland, UK.

The barite mineralization in the Alston Moore high is thought to be deposited at relatively low (~55°C) temperature in the waning stages of hydrothermal circulation by mixing of a high-sulfide meteoric water with an evaporitic brine (Bouch, 2008). The PAAS normalized REE abundances show La/Sm<1 and Sm/Lu>1 (total La/Lu<1), an uncertain –VE Ce anomaly and a +VE Eu anomaly of 2.41-3.78. Although the temperature of chemical precipitation is low, a +VE Eu anomaly is expected for hydrothermal waters that are evolved and have cooled down. The –VE Ce anomaly is an indication for the presence of oxygen, which is expected to have affected the Ce content of the Permian to Triassic meteoric waters from which the sulfide was derived.

1986-1321. Bad Grund deposit, Harz Mountains, Germany.

The Bad Grund barite is thought to result from deep crustal vein mineralization by precipitation from a sulfate-rich evaporitic brine and deep, hot Ba-rich fluids at a temperature >250°C (Zheng and Hoefs, 1993; Möller and Luders, 1993). The PAAS normalized REE patterns show a relatively smooth behavior for the non-digested sample and a somewhat less smooth pattern for the 1986-1321 TD sample, both with La/Lu<1 and +VE Eu anomalies of 1.96-7.95 (1986-1321TD) or 2.82-7.95(1986-1321) and an uncertain –VE Ce anomaly for the LA-ICP-MS data. The +VE Eu as observed in the data corresponds well with the >250°C Ba rich fluid. The –VE Ce anomaly is characteristic for modern seawater and will also be reflected in fluids that are derived from recent seawater such as the sulfate-rich evaporitic brine.

DB5. Dresser barite deposit, Western Australia.

The bedded barite deposit as found in the Dresser formation is also supposed to be derived from reaction of a hydrothermal vent fluid with (Paleo)-Archean seawater (*Figure 1.13*; Ueno, 2008). The PAAS normalized REE abundance pat-

tern shows that the original sample and the duplicate have differences in the HREE content and that there are differences between the measured Nd and Er content between ICP-MS and LA-ICP-MS data. For both analytical methods and both samples the La/Lu ratio is larger than 1. The samples are characterized by an uncertain –VE Ce anomaly measured by the LA-ICP-MS. Both samples are further characterized by large, but uncertain +VE Eu anomalies of 6.22-9.31. These large Eu anomalies correlate with the proposed hydrothermal vent fluid that the barite was derived from. However, the uncertain –VE Ce anomaly is not typical for Precambrian seawater. Further research towards the reliability of this Ce anomaly is important to show if Precambrian seawater contained significant amounts of oxygen to make oxidative removal of $Ce(IV)O_2$ possible.

1986-1334. Sieberthal deposit, Harz Mountains, Germany.

The vein barite mineralization of sample 1986-1334 is thought to be derived from a complex mixing of fluids (Zheng and Hoefs, 1993; Stedingk and Stoppel, 1993) including a mixed sulfide-rich fluid that precipitated barite at 50-100°C. The PAAS normalized REE patterns give an uncertain +VE Eu anomaly an uncertain –VE Ce anomaly which is measured in the LA-ICP-MS data. For this sample, the –VE Ce anomaly is very interesting, since it is proposed by Zheng and Hoefs (1993) that the sulfate was derived from a mixture of igneous sulfide (no Ce anomaly expected) and Zechstein evaporates (derived from a sea thus a –VE Ce anomaly expected). Since the –VE anomaly as found in this research for Ce seems to be consistent with all foregoing samples, it can be concluded that the contribution of Zechstein evaporites were indeed important as a sulfate source for the barite precipitation. From the temperature constraints as given by Zheng and Hoefs (1993) no +VE Eu anomaly would be expected, however, it is most likely that the environment would have been reduced. Further research towards the reliability of this anomaly can confirm this hypothesis.

1896-45. Sellafield (Frizington) area, Cumberland, UK.

Fluid inclusion studies of the Sellafield vein barite deposits by Milodowski et al (1998) revealed that this vein barite resulted from mixing at low T (<80°C) of a complex evaporated seawater brine with a Ba-rich local fluid. The PAAS normalized REE abundance patterns show a relatively smooth LA-ICP-MS obtained REE pattern with La/Lu<1, an uncertain +VE Eu anomaly of 6.92-8.56 and an uncertain –VE Ce anomaly. This –VE Ce anomaly corresponds well with the presence of seawater (although evaporitic) as a sulfate source. The +VE Eu anomaly, however, is debatable since it is unclear if the environment was reducing enough for the low-T Ba-rich local fluid to reduce Eu(III) to Eu(II).

For the following samples, limited T or redox estimates are present from geochemical parameters.

08-LON-01. Barberton Greenstone belt, South Africa.

All four samples as measured by the two techniques resulted in such different patterns that both the –VE Ce anomaly as well as the +VE Eu anomaly should be taken as uncertain. However, the presence of intrusions in the region adjacent to the barite lenses rises the expectation of a +VE Eu anomaly in the barite. Further research to other parameters has to confine the source of the sulfate and to test the possibility of the –VE Ce anomaly by oxidative scavenging. Another feature that has to be taken into account is the amphibolite facies metamorphism that has affected the region, since large fluid to rock volumes can alter the REE abundance pattern in the rock.

Ver01d and Ver02. Barberton Greenstone Belt, South Africa.

The correlation between the original and the duplicate sample for the LREEs in Ver01d with both techniques assume the –VE Ce anomaly to be an indication. The difference between these samples could be derived from differences in deformation grade, which is more severe for sample Ver02. The barites are present on top of volcanic rocks and a +VE Eu anomaly can be expected from the precipitation of the barite from

high-T, reduced fluids circulating through these rocks. The uncertain –VE Ce anomaly in sample Ver01d can be uncertain of oxygenation of seawater from which also the overlying carbonates are possibly precipitated. It is important to note that part of the overlying rock is a serpentenized shear zone, which is uncertain of large fluid to rock ratios and possible weathering of the REE pattern in the underlying barite.

TR041, Stentor farm, South Africa.

Both Ce and Eu anomalies as calculated are uncertain and the REE abundance pattern was remarkable because of large ICP-MS concentrations compared to LA-ICP-MS concentrations. Both the structural feature for barite to be found in seams as well as the greenschist facies metamorphism of the region could have contributed to the presence of accessory phases and fluid inclusion in joints and cracks due to the pressure of 4.2-4.5kbar experienced. These phases could have affected the ICP-MS REE abundance pattern. The presence of barite in seams in felsic quartz-muscovite host rock suggests an epigenetic origin of these barites, with expected +VE Eu anomalies and absent Ce anomalies.

08-BV-01. Barberton Greenstone belt, South Africa.

The 08-BV-01 sample comprises of both detrital and bladed barite crystals surrounded by siliciclastic rocks and in the vicinity of continental contaminants as Zr and Cr. The –VE Ce as found in the LA-ICP-MS data can thus be an indicator for 1) barite precipitation from oxygenated seawater and evidence for atmospheric oxygen levels at 3.23-3.26Ga or 2) is a remnant of partial dissolution, renewed precipitation and reworking in a later-stage oxygenated environment.

From the comparison with the geology is appears that the data on Ce and Eu anomalies give fair correlations with the proposed environments of formation of the younger barites. However, to use this correlation to draw conclusions on the oxidation state of the Archean environment would be premature, since the anomalies in these Archean samples are mostly uncertain. In order to be able to draw conclusions on the environment of formation of Archean barites, further parameters must be compared with the obtained geology such as sulfur isotopes and fluid inclusion studies.

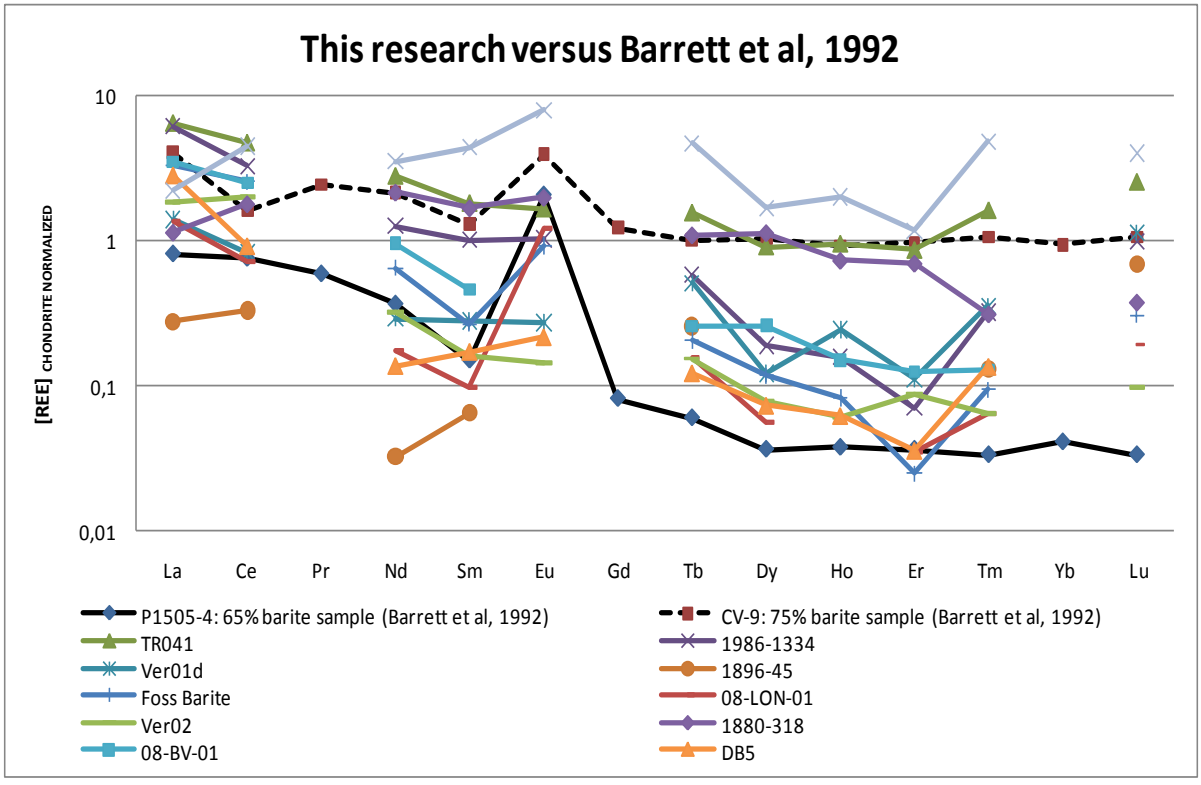

Figure 4.1. Comparison between obtained REE abundances between data from Barrett et al (1992): black lines.

Furthermore, the effect of greenschist facies metamorphism on the REE abundances in barite should be further examined. Multiple analysis using LA-ICP-MS and Ion Exchange Chromatography followed by ICP-MS analysis should be performed in order to distinguish between true anomalies or uncertain anomalies.

4.3. Comparison with existing data on REE abundances in Barite - REE partitioning mechanisms in barite and CHARAC behavior.

For comparison with existing data on REE abundances in barite, the ICP-MS chondrite normalized patterns are plotted together with a selection of the data from Barrett et al (1992) and Guichard et al (1979). The graphs can be found in *figure 4.1 and 4.2*. The REE abundances fall remarkably well within the range of abundances as obtained by Guichard (1979) and Barrett et al (1979). From the article of Barrett et al (1992) only the sample P1505-4 (65% barite) and sample CV-9 (75% barite) is taken into account since these samples are the only barite containing

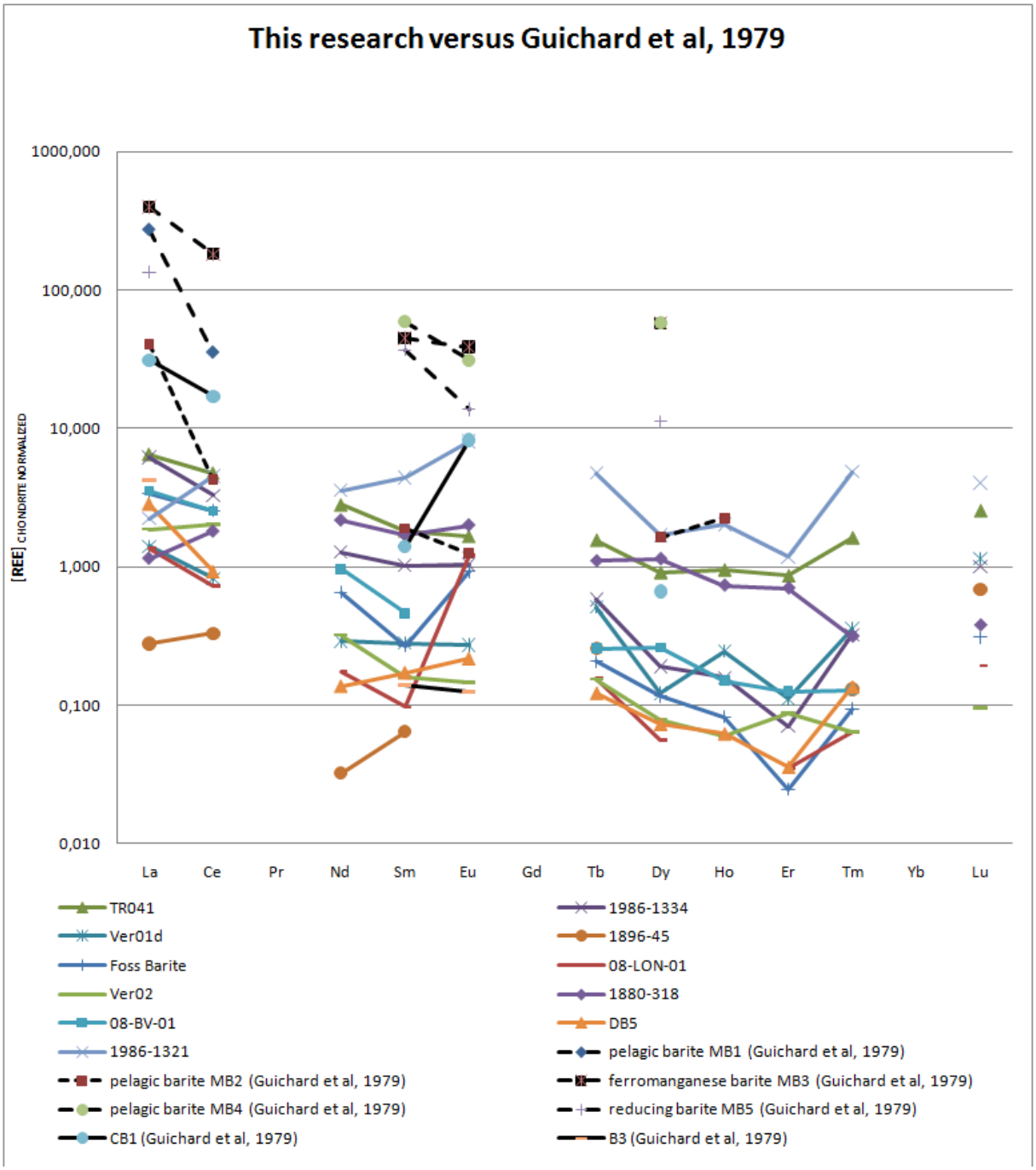

Figure 4.2. Comparison of REE abundances between a selection of data from Guichard et al (1979): black lines.

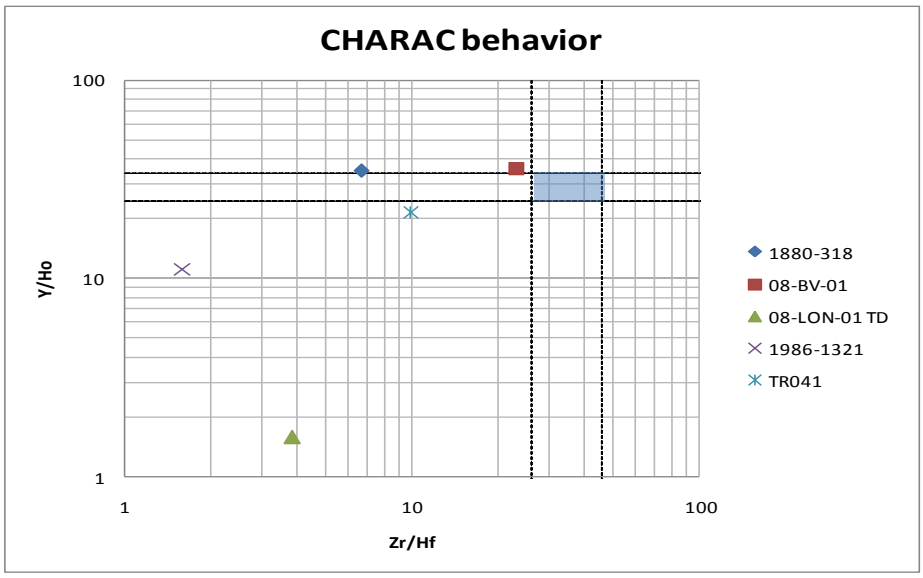

Figure 4.3. Investigation of the Charge and Radius Controlled behavior of the geochemical twins Y/Ho and Zr/Hf. The blue field are the chondritic values. It can be seen that none of the sample with detectable Y, Ho, Zr and Hf abundances plot within this field, indicating barite precipitation from a fluid in which REE partitioning by complexation was an important process.

samples from his research. Sample P1505-4 is thought to be derived from alteration reactions in the deeper parts of hydrothermal systems (T: 300-350°C), resulting in absent –VE Ce anomalies and large +VE Eu anomalies. Sample CV-9 is thought to be derived from a 1:500 mixture of hydrothermal vent water and eastern Pacific bottom water resulting in the presence of both a –VE Ce anomaly and a +VE Eu anomaly. Since most samples in this research show both a –VE Ce anomaly and a +VE Eu anomaly, they are most likely derived from a mixture between oxygenated marine waters and high-T hydrothermal waters such as sample CV-9. The Guichard et al (1979) REE data are very hard to compare, since he provides only data for 4-5 REEs. A selection is taken from his research and the samples indicated as 'MB' represent marine barite, while the samples indicated with 'B' is a vein barite and 'CB' are 'continental' barites (epigenetic). It can be seen that the LREE enrichment as observed in all barites by Guichard et al (1979) is also observed for all Chondrite normalized REE patterns in this research, except for samples 1896-45 and 1986-1321. This LREE enrichment is typical for barite, which has large substitution sites and is

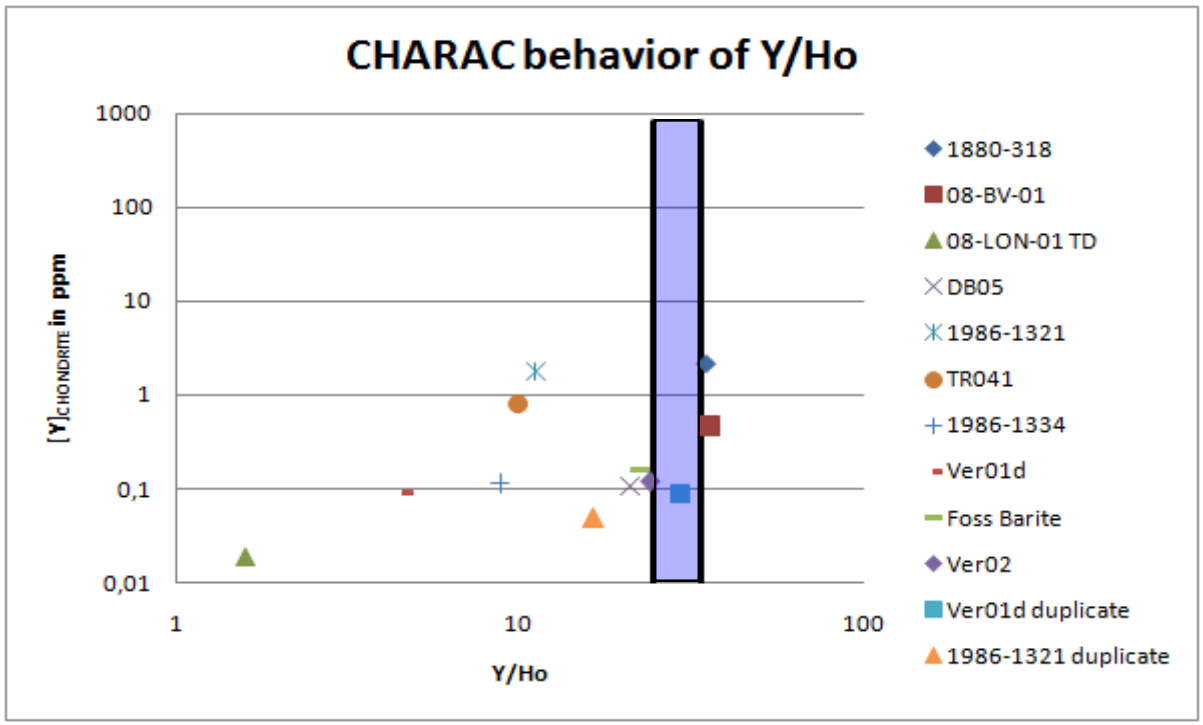

Figure 4.4. Investigation on the Charge and Radius Controlled behavior of geochemical twins Y and Ho.

also typical of complexation controlled behavior of the REEs, in which HREEs are more easily complexed by ligands in solution and are no longer available for incorporation into the barite crystal lattice. It can further be seen that the +VE Eu anomaly is only found in the hydrothermally formed 'continental' barites that display a +VE Eu anomaly because of promotion of Eu reduction by the precipitation of barite (Guichard et al, 1979) and that those can be compared with the barites from this research. The absence of the –VE Ce anomaly in marine barites as observed by Guichard (1979) cannot be confirmed due to contamination of the ICP-MS data with Ce.

The CHARAC behavior of the REEs in the barite samples was tested for a selection of barite that had Y, Ho, Zr and Hf abundances above the detection limits of the ICP-MS analysis. It can be seen in *figure 4.3* and *4.4* that none of the samples falls within the CHARAC field as indicated by Bau (1996). In figure 4.4 it can be seen that samples Ver01d duplicate might display chondritic Y/Ho behavior, but since Ver01d plots well outside this field, it can be questioned if the Y and Ho measurements are reliable. It is however expected that non-CHARAC behavior of the REEs would be the result, since all barites are derived from highly evolved brines or ligand-rich seawater with high complexation potential. Therefore, in all samples, electron structure must be considered as an additional parameter which besides valency and size controlled the behavior of the REEs in the solutions from which the barites chemically precipitated (Bau, 1996). However, the lack of knowledge on the mechanics and physics of REE partitioning in barite makes it problematic to draw conclusions towards the exact causes of the REE patterns as observed in this research.

4.4. Future work and recommendations.

Since the method of fusing used to dissolve barite involves Na_2CO_3 that was apparently contaminated with Ce, it is recommended to use synthetically obtained Na_2CO_3 from precipitation of a Na-phase with a CO_3-phase to limit the presence of contaminants. Since only 0.5g of $BaSO_4$ powder was used, it is also possible to use chemically precipitated $BaSO_4$ from pure solutions in future experiments on the adjustments of the Ion Exchange Chromatography method.

It is important to spike the 1L bottle solutions before Ion Exchange Chromatography before the elution through the C18 cartridges, because a yield of the method can then be calculated. However, since Pr is an important element in calculating Ce anomalies, it is better to only use Yb instead of both or use an isotope that appears to be unaffected by fractionation in barite such as Tm. Also care must be taken to spike the samples with concentrations not higher than 10-20x the expected concentrations, since the very high spikes in this research resulted in concentrations above upper detection limits and unreliable yield calculations.

The absence of either a external barite standard with known REE composition and/or an internal REE isotope with known abundance resulted in large uncertainty errors. Research is needed towards the potential of precipitating pure barite from a synthetic solution, thereby adding REEs in known composition such that 1) the behavior of REEs during barite precipitation can be analyzed and 2) a reliable external standard becomes available to calibrate LA-ICP-MS and Ion Exchange Chromatography and ICP-MS analysis. The usage of ^{87}Sr as internal known isotope could be debated due to the inhomogeneous distribution of this element in the barite samples as shown by EMP analysis. However, since Ba^{2+} is present in such high quantities in barite, Sr appeared to be the only element present in the rocks at concentrations the ICP-MS could be calibrated for. The presence of an external standard barite with known REE and Ba concentration could make ICP-MS apparatus calibration possible for rocks with such a range in concentrations and this could open the way for the usage of Ba as internal standard.

The usage of two different ICP-MS instruments can affect the obtained result since the oxide generation is not equal for both the XR and Element 2. Knowledge on this is present and can be used to check for interferences of BaO and BaO_2 by calculating back from the obtained counts for the oxides present.

5. Conclusions.

Ion Exchange Chromatography was performed on digested barite solutions to measure Rare Earth Elements by ICP-MS, in order to compare results and test for possible interferences during in situ LA-ICP-MS analysis of REE in barite. Optimal experiments involved digestion of 0.5g of barite in 5mL 6N HCl by fusing with 4.5g of Na_2CO_3 at 1200°C for 30min followed by grinding and leaching with 150mL UHQ to remove sulfates. A method for cation removal from solution by Ion Exchange Chromatography using 2-(ethylhexyl) orthophosphoric acid on a C18 Sep-Pak cartridge was adjusted for high Ba^{2+} concentrations in dissolved barite. This resulted in >99% removal of possible interfering Ba^{2+} from solution in a very constant way as was shown by elution curves for Ba^{2+}. Rare Earth Elements (REEs) were successfully captured by the 2-(ethylhexyl) orthophosphoric acid and were eluted in a 40mL 6N HCl solution with yields of 76-86% for synthetic barite and yields of 54->100% for natural barite. ICP-MS analyses of this 40mL REE solution were calibrated against in situ LA- ICP-MS. Comparison of REE abundances shows that both methods suffer from:

1. Anomalous high Gd concentrations in the ICP MS data possibly caused by interfering PrO with which the solution was spiked.
2. Contamination of the Na_2CO_3 flux with Ce.
3. Presence of Ba^{2+} in both methods resulting in interference of $^{137}Ba^{16}O$ on ^{153}Eu.
4. Absence of reliable internal and external standards to reliably quantify the LA-ICP-MS and Ion Exchange Chromatography process.
5. Presence of interfering accessory phases enriched in REEs such as monazites.
6. Poor detection limits.

I conclude that the analysis of REE abundances in barite by LA-ICP-MS might be possible for very homogeneous barites that contain minor accessory phases or are chemically purified. Calibration of these results by ICP-MS data acquired after Ion Exchange Chromatography is promising but also shows that this method has to be improved such that larger quantities of barite can be dissolved resulting in higher REE abundances and more reliable REE determination. The determination of redox and temperature conditions during barite precipitation by interpretation of Eu and Ce anomalies is ambiguous due to the Ce contamination of the fusing material and the Ba still present in the solutions after Ion Exchange Chromatography and that the anomalies should be calibrated against other temperature and redox parameters. First comparison of the obtained Eu and Ce anomalies with geological constraints shows the potential of the LA-ICP-MS method since most anomalies correspond with geological constraints. Further research is needed both to improve of the proposed method and to constrain the factors controlling REE partitioning in barite. This could include the usage of synthetically precipitated barite and Na_2CO_3 to overcome contamination, the use of an internal spike that is not used for anomaly calculations, such as Tm, and the acquisition of reliable internal and external standards.

7. Acknowledgements.

This research has been carried out under supervision of Paul Mason and Desiree Roerdink, who I'd like to thank for their reviews and fruitful discussions.

Research was performed in collaboration with the people from Jacobs University in Bremen, Germany, who were so kind to let me work in their laboratory. Therefore I would like to thank Michael Bau and Brian Alexander for their supervision and Jule Mawick for the laboratory assistance. Further analysis was performed in the laboratory of the Utrecht University, the Netherlands. I would like to thank Dineke van de Meent and Pieter Kleingeld for their assistance during the set-up of the experiments. I am grateful to Jan Drenth and Otto Stiekema for their assistance during rock preparation. Erik van Vilsteren, Giovanni Dammers and Ton Zalm are thanked for their contributions to this research in terms of ICP-OES and ICP-MS analyses. Anita van Leeuwen is thanked for XRD analysis and Tilly Bouten has been very helpful during Electron Microprobe analysis.

Most of all I would like to thank Helen de Waard for her assistance during LA-ICP-MS analyses, ICP -MS measurements and for providing practical solutions for tough problems.

The research is made possible by a grant from the European Science Foundation.

7. References.

1. **Anders E. and Grevesse N.;** Abundances of the elements: meteoritic and solar; Geochimica et Cosmochimica Acta; vol 53; pp 197-214; 1989
2. **Barbieri M., Masi, U and Tolomeo, L.**; Strontium geochemistry in the epithermal barite deposits from the Apuan Alps (Northern Tuscany, Italy); Chemical Geology; vol 35; pp 351-356; 1982
3. **Barrett, T.J., Jarvis, I. and Jarvis, K.E.;** Rare earth element geochemistry of massive sulfides-sulfates and gossans on the Southern Explorer Ridge; Geology; vol 18; pp 583-586; 1990
4. **Bau, M.;** Rare-earth element mobility during hydrothermal and metamorphic fluid-rock interaction and the significance of the oxidation state of europium; Chemical Geology; vol 93; pp 219-230; 1991
5. **Bau, M. and Möller, P.**; Rare earth element fractionation in metamorphogenic hydrothermal calcite, magnesite and siderite; Mineralogy and Petrology; vol 45; pp 231-246; 1992
6. **Bau, M.;** Controls on the fractionation of isovalent trace elements in magmatic and aqueous systems: evidence from Y/Ho, Zr/Hf and lanthanide tetrad effect; Contributions to Mineral Petrology; vol 123; pp 323-333; 1996
7. **Bau, M. and Dulski, P.;** Distribution of yttrium and rare-earth elements in the Penge and Kuruman iron-formations, Transvaal Supergroup, South Africa; Precambrian Research; vol 79; pp 37-55; 1996
8. **Bau, M. and Dulski, P.;** Comparing yttrium and rare earths in hydrothermal fluids from the Mid-Atlantic Ridge: implications for Y and REE behavior during near-vent mixing and for the Y/Ho ratio of Proterozoic seawater; Chemical Geology; vol 155; pp 77-90; 1998
9. **Bau, M.**; Scavenging of dissolved yttrium and rare earths by precipitating iron oxyhydroxide: experimental evidence for Ce oxidation, Y-Ho fractionation, and lanthanide tetrad effect; Geochimica et cosmochimica acta; vol 63; issue 1; pp 67-77; 1999
10. **Blount, C.W.;** Barite solubilities and thermodynamic quantities up to 300°C and 1400 bars; American Mineralogist; vol 62; pp 942-957; 1977
11. **Bolhar, R., Kamber, B.S., Moorbath, S., Fedo, C.M., Whitehouse, M.J.;** Characterization of Early Archean chemical sediments by trace element signatures; Earth and Planetary Science Letters; vol 222; pp 43-60; 2004
12. **Bouch, J.E., Naden, J., Shepherd, T.J., Young, B., Benham, A.J., McKervey, J.A., Sloane, H.J.;** Stratabound Pb-Zn-Ba-F mineralization in the Alston block of the North Pennine Orefield (England) - origins and emplacement; British Geological Survey Research Report; RR/08/06; pp 1-25; 2008
13. **Bowers T.S., Jackson, K.J. and Helgeson, H.C.**; Equilibrium activity diagrams; Springer-Verlag, Berlin; 397p; 1984
14. **Breit, G.N., Simmons, E.C. and Goldhaber, M.B.**; Dissolution of barite for the analysis of strontium isotopes and other chemical and isotopic variations using aqueous sodium carbonate; Chemical Geology; vol 52; pp 333-336; 1985
15. **Buick, R. and Dunlop, J.S.R.;** Evaporitic sediments of Early Archean age from the Warrawoona Group, Western Australia; Sedimentology; vol 37; pp 247-278; 1990
16. **Canfield, D.E., Habicht, K.S. and Thamdrup, B.;** The Archean sulfur cycle and the early history of atmospheric oxygen; Science; vol 288; pp 658-661; 2000
17. **Church, T.M.;** Marine Barite; *in* Marine Minerals; Reviews in Mineralogy; vol 6; pp 175-209; 1979
18. **Date, A.R. and Hutchinson, D.**; Determination of Rare Earth Elements in geological samples by Inductively Coupled Plasma Source Mass Spectrometry; Journal of Analytical Atomic Spectrometry; vol 2; 1987
19. **Derry, L.A. and Jacobsen, S.B.**; The chemical evolution of Precambrian seawater: evidence from REEs in banded iron formations; Geochimica et cosmochimica acta; vol 54; pp 2965-2977; 1990
20. **Dulski, P.;** Interferences of oxide, hydroxide and chloride analyte species in the determination of rare earth elements in geological samples by inductively coupled plasma mass spectrometry; Fresenius Journal of Analytical Chemistry; vol 350; pp 194-203; 1994
21. **Elderfield, H.**; The oceanic chemistry of the rare-earth elements; Philosophical Transactions of the Royal Society of London. Series A, Mathematical and Physical sciences; vol 325; issue 1583; pp 105

-126; 1988
22. **Grotzinger, J.P. and Kasting, J.F.;** New constraints on Precambrian ocean composition; The Journal of Geology; vol 101; pp 235-243; 1993
23. **Guichard, F., Church, T.M., Treuil, M. and Jaffrezic, H.;** Rare Earths in barite: distribution and effects in aqueous partitioning; Geochimica et Cosmochimica Acta; vol 43; pp 983-987; 1979
24. **Haas, J.R., Everett, L.S. and Sassani, D.C.**; Rare earth elements in hydrothermal systems: estimates of standard partial molal thermodynamic properties of aqueous complexes of the rare earth elements at high pressures and temperatures; Geochimica et cosmochimica acta; vol 59; issue 21; pp 4329-4350; 1995
25. **Habicht, K.S., Gade, M., Thamdrup, B., Berg, P. and Canfield, D.E.**; Calibration of sulfate levels in the Archean ocean; Science; vol 298; issue 5602; pp 2372-2374; 2002
26. **Hanor, J.S.;** Barite-Celestine geochemistry and environments of formation; *in* Sulfate Minerals - crystallography, geochemistry and environmental significance; Reviews in Mineralogy and Geochemistry; vol 40; pp 193-275; 2000
27. **Huston, D.L. and Logan, G.A.;** Barite, BIFs and bugs: evidence for the evolution of the Earths early hydrosphere; Earth and planetary science letters; vol 220; pp 41-55; 2004
28. **Jarvis, K.E., Gray, A.L. and McCurdy, E.;** Avoidance of spectral interference on Europium in Inductively Coupled Plasma Mass Spectrometry by sensitive measurement of the doubly charged ion; Journal of analytical atomic spectrometry; vol 4; pp 743-747; 1989
29. **Jørgensen, B. and Kasten, S.**; Sulfur cycling and methane oxidation; *in Marine Geochemistry*; pp 271-309; 2006
30. **Kagi, H., Dohmoto, Y. Takano, S. and Masuda, A.;** Tetrad effect in lanthanide partitioning between calcium sulfate crystal and its saturated solution; Chemical Geology; vol 107; pp 71-82; 1993
31. **Klinkhammer, G.P., Elderfield, H., Edmond, J.M. and Mitra, A.;** Geochemical implications of rare earth element patterns in hydrothermal fluids from mid-ocean ridges; Geochimica et Cosmochimica Acta; vol 58; issue 23; pp 5105-5113; 1994
32. **Lottermoser, B.G**.; Rare earth elements and hydrothermal ore formation processes; Ore Geology Reviews; vol 7; pp 25-41; 1992
33. **Lowe, D.R. and Knauth, L.P.;** Sedimentology of the Onverwacht group (3.4 billion years), Transvaal, South Adrica, and its bearing on the characteristics and evolution of the Early Earth; Journal of Geology; vol 85; pp 699-723; 1977
34. **Martin, E.E., McDougall, J.D., Herbert, T.D., Paytan, A. and Karstner, M.;** Strontium and Neodymium isotopic analysis of marine barite separates; Geochimica et Cosmochimica Acta; vol 59; pp 1353-1361; 1995
35. **Michard, A.**; Rare earth element systematics in hydrothermal fluids; Geochimica et cosmochimica acta; vol 53; pp 745-750; 1989
36. **Milodowski, A.E., Gillespie, M.R., Naden, J., Fortey, N.J., Shepherd, T.J., Pearce, J.M. and Metcalfe, R.;** The petrology and paragenesis of fracture mineralization in the Sellafield area, west Cumbria; Proceedings of the Yorkshire Geological Society; vol 52; issue 2; pp 215-241; 1998
37. **Moller, P. and Luders, V.;** Synopsis, *in* Monograph series on Mineral Deposits - Formation of Hydrothermal vein deposits; a case study of the Pb-Zn, barite and fluorite deposits of the Harz Mountains (edited by Moller, P. and Luders, V.); vol 30; pp 285-291; 1993
38. **Morgan, J.W. and Wandless, G.A.;** Rare earth element distribution in some hydrothermal minerals: evidence for crystallographic control; Geochimica et Cosmochimica Acta, vol 44, pp 973-980; 1980
39. **Nance, W.B. and Taylor, S.R.**; REE patterns and crustal evolution - I. Australian post-Archean sedimentary rocks; Geochimica et Cosmochimica Acta; vol 40; pp 1539-1551; 1976
40. **Nesse, W.D.;** Carbonates, Borates, Sulfates and Phosphates *in* Introduction to optical microscopy; pp 275; 2004
41. **Nijman, W., de Bruijne, K.H. and Valkering, M.E.;** Growth fault control of Early Archean cherts, barite mounds and chert-barite veins, North Pole Dome, Eastern Pilbara, Western Australia; Precambrian Research; vol 88; pp 25-52; 1998
42. **Ohmoto, H., Watanabe, Y., Ikemi, H., Poulson, S.R. and Taylor, B.E.;** Sulphur isotope evidence for

an oxic Archaean atmosphere; Nature; vol 442; issue 24; pp 908-911; 2006
43. **Pearce, N.J.G., Perkins, W.T., Westgate, J.A., Gorton, M.P., Jackson, S.E., Neal, C.R. and Chenery, S.P.**; A compilation of new and published major and trace element data for NIST SRM 610 and NIST SRM 612 glass reference materials; Geostandards Newsletter; vol 21; issue 1; pp 115-144; 1997
44. **Piper, D.Z.;** Rare earth elements in the sedimentary cycle: a summary; Chemical Geology; vol 14; pp 285-304; 1974
45. **Reimer, T.O.;** Archean sedimentary barite deposits of the Swaziland Supergroup (Barberton Mountain Land, South Africa); PreCambrian Research; vol 12; pp 393-410; 1980
46. **Riedinger, N., Pfeifer, K., Kasten, S., Garming, J.F.L., Vogt, C. and Hensen, C.**; Diagenetic alteration of magnetic signals by anaerobic oxidation of methane related to a change in sedimentation rate; Geochimica et Cosmochimica Acta; vol 69; issue 16; pp 4117-4126; 2005
47. **Roerdink, D.L., Mason, P.R.D., Farquhar, J. and Reimer, T.;** Paleoarchean barites record microbial reduction of a well-mixed oceanic sulfate pool; submitted to??; 2011
48. **Rowe, J., Turner, P. and Burley, S.;** Palaeomagnetic dating of the west Cumbrian hematite deposits and implications of their mode of formation; Proceedings of the Yorkshire Geological Society; vol 52; issue 2; pp 59-71; 1998
49. **Schwinn, G. and Markl, G.**; REE systematics in hydrothermal fluorite; Chemical Geology; vol 216; pp 225-248; 2005
50. **Shabani, M.B., Akagi, T. and Masuda, A.;** Preconcentration of trace Rare Earth Elements in seawater by complexation with bis(2-ethylhexyl) hydrogen phosphate and 2-ethylhexyl dihydrogen phosphate adsorbed on a C_{18} cartridge and determination by inductively coupled plasma mass spectrometry; Analytical Chemistry; vol 64; pp 737-743; 1992
51. **Shen, Y., Buick, R. and Canfield, D.E.**; Isotopic evidence for microbial sulphate reduction in the early Archaean era; Nature; vol 410; pp 77-81; 2001
52. **Stedingk, K. and Stoppel, D.;** Stratigraphy, Petrography, Paragenesis and Tectonic features in the Upper and Middle Harz vein districts, *in* Monograph series on Mineral Deposits - Formation of Hydrothermal vein deposits; a case study of the Pb-Zn, barite and fluorite deposits of the Harz Mountains (edited by Moller, P. and Luders, V.), vol 30; pp 55-64; 1993
53. **Sverjensky, D.A.**; Europium redox equilibria in aqueous solution; Earth and Planetary Science letters; vol 67; pp 70-78; 1984
54. **Ueno, Y., Yamada, K., Yoshida, N., Marayuma, S. and Isozaki, Y.**; Evidence from fluid inclusions for microbial methanogenesis in the early Archaean era; Nature; vol 440; issue 23; pp 516-519; 2006
55. **Ueno, Y., Ono, S., Rumble, D. and Maruyama, S.;** Quadruple sulfur isotope analysis of ca. 3.5Ga Dresser Formation: new evidence for microbial sulfate reduction in the Early Archean; Geochimica et Cosmochimica Acta, vol 72; iss 23; pp 5675-5691; 2008
56. **White, W.M.;** Chapter 7: Trace elements in igneous processes; *in* Geochemistry; pp 265-275; 2001
57. **Winchester, J.W.**; Rare Earth chromatography using bis(2-ethylhexyl) orthophosphoric acid; Journal of Chromatography; vol 10; pp 502-506; 1963
58. **Willan, R.C.R. and Coleman, M.L**.; Sulfur isotope study of the Aberfeldy barite, zinc, lead deposit and minor sulfide mineralization in the Dalradian metamorphic terrain, Scotland; Economic Geology; vol 78; pp 1619-1656; 1983
59. **Wood, S.A.;** The aqueous geochemistry of the rare-earth elements and yttrium. 1. Review of available low-temperature data for inorganic complexes and the inorganic REE speciation of natural waters; Chemical Geology; vol 82; pp 159-186; 1990a
60. **Wood, S.A.;** The aqueous geochemistry of the rare-earth elements and yttrium. 2. Theoretical predictions of speciation in hydrothermal solutions to 350°C at saturation water vapor pressure; Chemical geology; vol 88; pp 99-125; 1990b
61. **Zheng, Y.F. and Hoefs, J.;** Stable isotope geochemistry of hydrothermal mineralizations in the Harz mountains; II. Sulfur and oxygen isotopes of sulfides and sulfate and constraints on metallogenetic models, *in* Monograph series on Mineral Deposits - Formation of Hydrothermal vein deposits; a case study of the Pb-Zn, barite and fluorite deposits of the Harz Mountains (edited by Moller, P. and Luders, V.), vol 30; pp 211-230; 1993

APPENDIX 1

Failed digestion experiments.

Since barite is a notoriously difficult mineral to digest due to its low solubility, it was proposed to fuse the barite powder in a 1:10 ratio with a lithium borate flux resulting in a homogenized pearl. However, further experiments carried out with this material revealed that the solubility of barite did not increase enough in order to obtain a REE-rich solution. However, the methods and results of the failed experiments are very briefly discussed in this Appendix, since information on the behavior of barite was gained during these experiments.

Approximately 0.6 grams barite (sample from the mineral collection of the Utrecht University - other samples than used in further research) and 6 grams lithium borate were fused for 10 minutes at temperatures around 750° Celsius. The obtained pearls were grinded into very fine powder using an agate grinder. This powder is further referred to as 'pearl powder'.

HNO_3

Respectively 0.2g and 0.1g of pearl powder were digested in 50ml Greiner tubes using 25ml 10% Suprapure HNO_3 and 25ml UHQ. After one night of shaking, a residue was present in the Greiners which could either be $BaSO_4$ or non-dissolved lithium borate and because of this, the method was rejected.

HCl

At the laboratory of Jacobs University, Bremen, 100mg of pearl powder is added to 15ml 0.5M HCl and heated to 100°C overnight in Teflon vessels. After 12 hours of heating, a white suspension was clearly visible in the Teflon vessels. New samples were made by adding 300mg pearl powder to 10ml 1.58M HCl in a Teflon vessel and heating this under pressure to 225°C for 12 hours. After these 12 hours, the samples were heated without lid to evaporate the HCl off. This resulted very quickly in mass-loss due to cracking of the samples surface and therefore, this method was rejected.

Aqua Regia

This method was tested to investigate if significant amounts of powder (200mg - 300mg) could be dissolved using 7.5ml HCl and 2.5ml HNO_3 (both ultrapure). The samples were first heated to 60°C and regularly stirred to avoid mass-loss from cracking surfaces. After 30min, not all sample was dissolved and the Teflon beakers were placed under pressure and higher temperature for another 6 hours. After this period, a white coloured precipitate was present in nearly all vessels, together with a needle-like crust floating on top. 1ml of ultrapure HNO_3 was added to enhance dissolution. The aqua regia and the added HNO_3 created a pH that was approximately 0.95, and because a pH of 1,8 was wanted for ICP-MS analysis, the acids are evaporated off the sample. This procedure was enhanced by adding UHQ water to the Teflon vessels and by adjusting the temperature to 120°C. After a few of hours, the precipitate was nearly gone and it was assumed that everything still present dissolves when diluting the samples to 1L. However, ICP-MS analysis (not published in this report) of these samples showed underestimation of the Ba concentrations when compared to calculations, probably caused by incomplete digestion. Therefore this method is rejected for future research.

HF+Perchloric acid

Teflon vessels were filled with approximately 200mg of sample powder and 4mL of HNO_3 and 2mL of HF (both concentrated) were added to the samples. This order was important since HF gave a

strong reaction when directly added to the sample powder. The liquids were kept at room temperature for approximately 4h and were then heated overnight at 235°C. After heating a white precipitate was present in the samples, this might be due to the fact that HF reacts with the REEs to form REEF that precipitates (Brian Alexander, pers comm.). Therefore, the HF was evaporated off the samples and the powder was taken up in some weaker 5mL of 0.5M HNO_3. After complete evaporation it was assumed that the REEF bonds were disconnected and the powder was dissolved in 2.5mL perchloric acid. The samples were further cooked at 220°C until all liquid was evaporated. In order to raise the pH, the remaining solid was then taken up into 0.5M 9mL perchloric (1 sample was taken up into +- 10mL HNO3, but a precipitate directly formed). The perchloric containing samples still show precipitate and to enhance dissolution, 2mL of concentrated perchloric acid was added together with an increase in temperature to 180 degrees C. After complete evaporation at a temperature of 180 degrees Celsius, minor precipitate was observed in some samples and therefore this method was rejected.

H_2SO_4

7 samples of 60,50,40,30,20,10 and 0 mg BaSO4 (98% pure) were dissolved in approximately 25mL H_2SO_4 (10,8M) and cooked at 120degrees C overnight. It should be noted that $BaSO_4$ is soluble in concentrated H_2SO_4, but that the pH of the final solution will be too low for measurements using the ICP-MS. Therefore, the pH of the solution is adjusted by A) adding a few ml UHQ and B) driving off the sulfur by heating the samples on a hotplate in Teflon vessels. It is found that directly precipitate forms when UHQ is added and that after more than several weeks of evaporation, still a lot of H_2SO_4 is present due to its high boiling point. This digestion method is rejected because it is time-consuming and precipitate forms during the slightest dilution with UHQ.

APPENDIX 2

REE preconcentration with Ion Exchange Chromatography—Lab Scheme

Requisites.

- 500mL volumetric flask with 6M HCl for cleaning purposes (can be recycled)
- 500mL volumetric flask with UHQ for cleaning purposes
- 500 mL volumetric flask with 0.01M HCl for cleaning
- 500mL volumetric flask with 6M ultrapure HCl for eluation
- Bis-(2-ethylhexyl) phosphoric acid, stored in dark environment
- 1 L Nalgene bottles for sample solution
- 50mL Greiners for eluate collection
- C18 Sep-Pak cartridges, 360mg solvent
- Tygon tubing (id. 4.8/od. 8.0/wall 1.6mm)
- Parafilm
- Beaker glasses to collect waist

Safety warning.

Note that pressure can build up in the tubing if the ester-filled cartridge is attached and that the cartridge can come off at high speed, releasing 6M HCl violently. Safety goggles and gloves must be worn all the time.

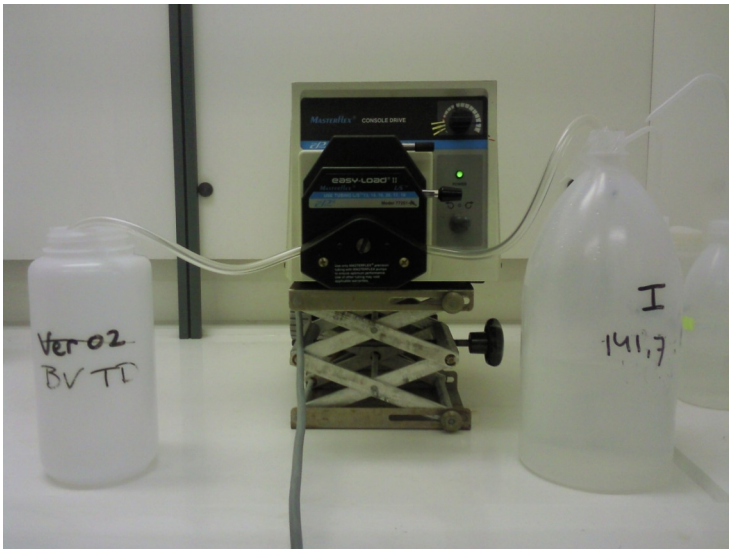

Cartridges (Sep-pak c18, 360mg, Waters) are prepared by running the following steps.

1. clean each cartridge with **10 mL 6M HCl** (ultrapure) at a speed of **3ml/min**
2. bring back to neutral by rinsing them with **7ml UHQ** at a speed of **3ml/min**
3. add approximately **0.375ml (at least 300mg, see Shabani, 1992)** of *bis-(2-ethylhexyl) phosphoric acid* (until the cartridge is nearly filled) at a speed of **3ml/min**
   - use other tube, 1 at a time
4. clean cartridge with **6ml 6M HCl** at a speed of **3ml/min**
5. bring back to neutral by flushing with **40ml UHQ** at a speed of **9ml/min** (still drops needed)
6. protect the samples with **parafilm** during the process and if not used directly; wrap in parafilm and store at a secure place.

Columnar extraction - preconcentration.

1. Stick 4 tubes (numbered) into the pump.
2. Rinse the outsides of the tubes (10cm on each side) and the insides with a **few ml 6M HCl** followed by a **few ml UHQ**.
3. Put the tubes on the left side in the 1L bottles that contain the sample (halfway).
4. Close the bottle off and attach the tube firmly with parafilm.
5. Collect 10mL of the Original Sample before attaching the cartridge.
6. Write a number on each prepared cartridge that is corresponding to the sample and wash the ends of the cartridge with **0.01M HCl**.
7. Attach the cartridges to the 4 tubes at the right side of the pump and let them hang into waste bottles (bottles **must** be numbered and weighted, weight is written on each bottle).
8. Let the sample liquid run through at a speed of **13ml/min**, this will take approximately 1hour for 1L.
9. Check regularly and adjust the depth at which the tubes are hanging in the bottles.
10. After the bottles are empty, remove the cartridges, wrap them in parafilm and store in the refrigerator.
11. Clean the tubes with **6M HCl Cleaning liquid (500ml**) and then with **500ml UHQ.**
12. Weigh the waste bottles that now contain the liquid and send to ICP-OES for Ba concentra tion check.
13. Start the whole process again with new samples and new cartridges.

Eluation of Residue from Cartridges.

1. Rinse the cartridge with **10mL of 0.01M HCl** at a speed of **3mL/min**.
2. Eluate the content of the cartridge in a **50mL PVC bottle** with **40mL 6M HCl** at a speed of **13mL/min.**
3. The sample can be stored away now.

Note: different tubing should be used for flowing with HCl+UHQ, bis-(2-ethylhexyl) orthophos-phoric acid and sample. In between different samples, the tubing can be rinsed by passing through 50mL 6M Cleaning HCl followed by 50mL UHQ at flow speeds of 13mL/min.

APPENDIX 3

X-ray Diffraction analysis

This Appendix shows the results for every single barite sample of the XRD analysis. A plot with the combined results can be found in the Results section earlier in this report.

FOSS BARITE

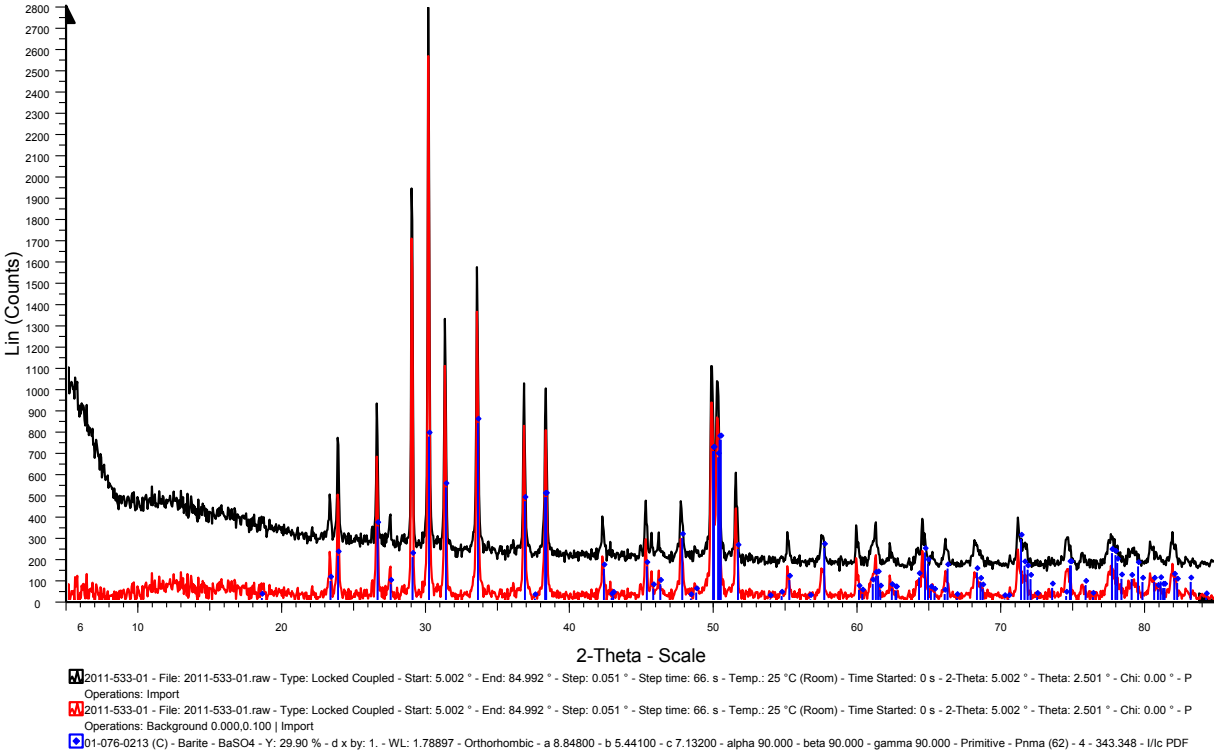

VER01D

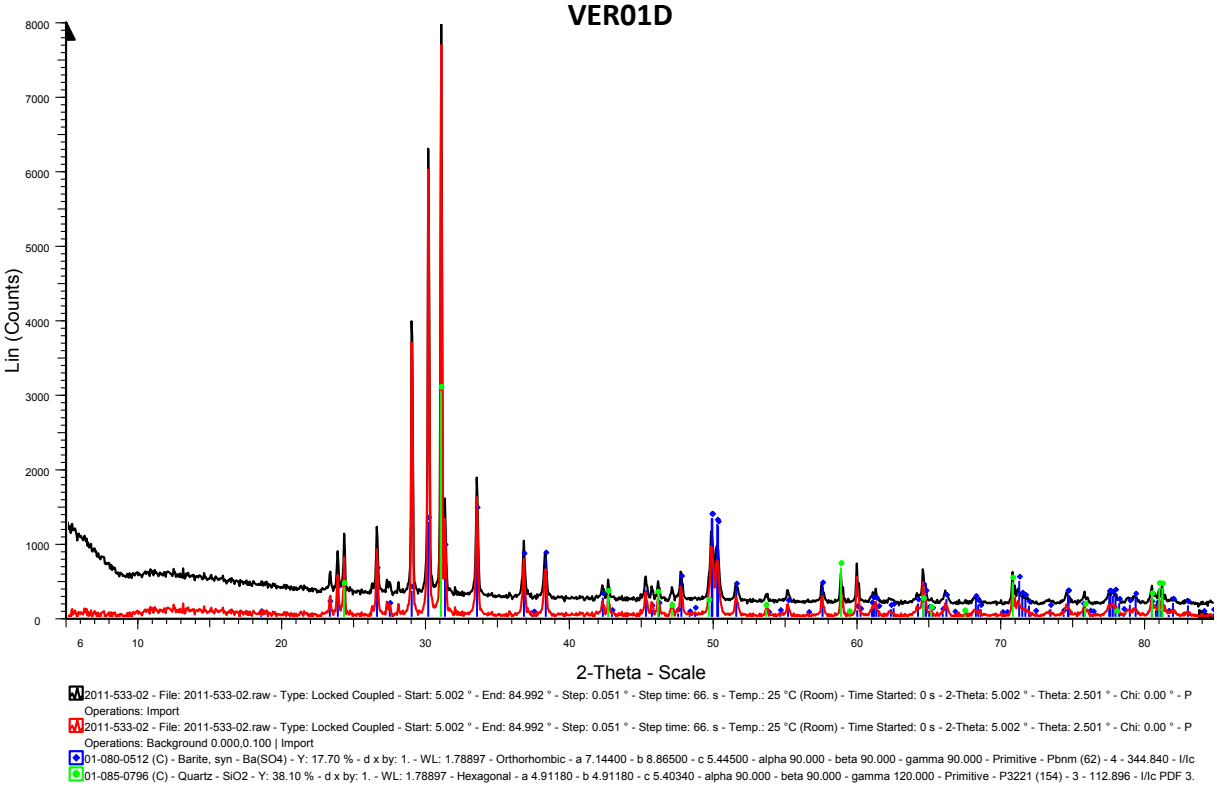

APPENDIX 3-continued

X-ray Diffraction analysis

VER02

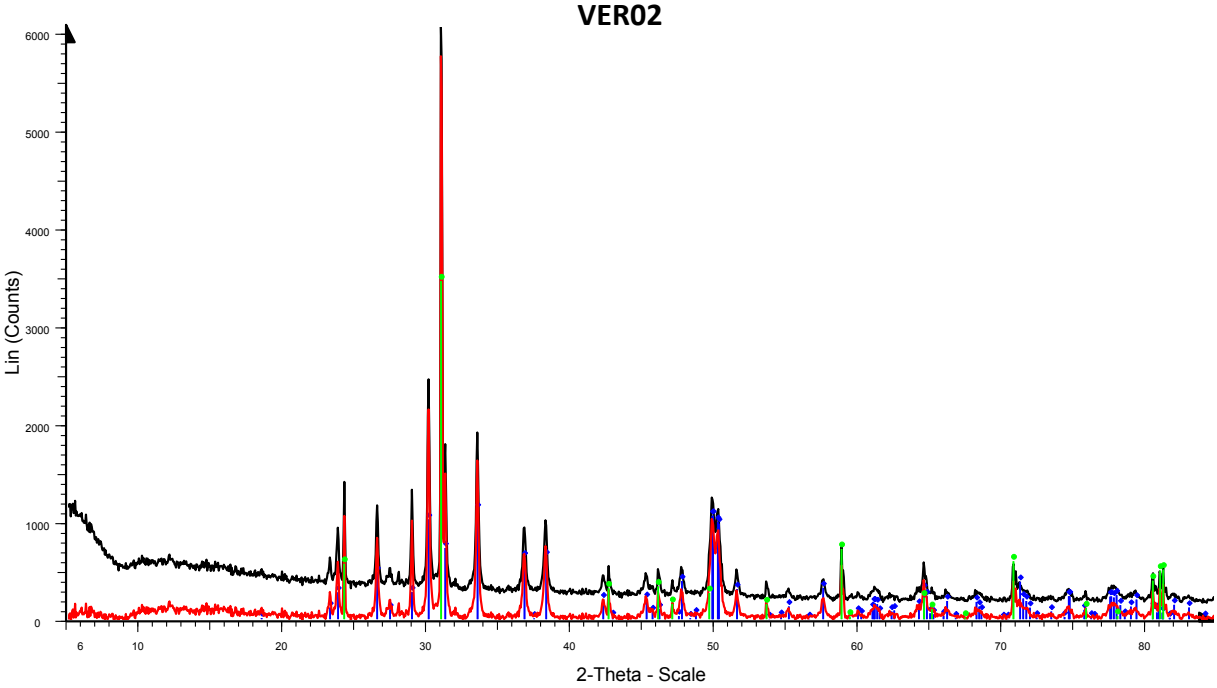

2011-533-03 - File: 2011-533-03.raw - Type: Locked Coupled - Start: 5.002 ° - End: 84.992 ° - Step: 0.051 ° - Step time: 66. s - Temp.: 25 °C (Room) - Time Started: 0 s - 2-Theta: 5.002 ° - Theta: 2.501 ° - Chi: 0.00 ° - P
Operations: Import
2011-533-03 - File: 2011-533-03.raw - Type: Locked Coupled - Start: 5.002 ° - End: 84.992 ° - Step: 0.051 ° - Step time: 66. s - Temp.: 25 °C (Room) - Time Started: 0 s - 2-Theta: 5.002 ° - Theta: 2.501 ° - Chi: 0.00 ° - P
Operations: Background 0.000,0.100 | Import
01-080-0512 (C) - Barite, syn - Ba(SO4) - Y: 18.59 % - d x by: 1. - WL: 1.78897 - Orthorhombic - a 7.14400 - b 8.86500 - c 5.44500 - alpha 90.000 - beta 90.000 - gamma 90.000 - Primitive - Pbnm (62) - 4 - 344.840 - I/Ic
01-085-0504 (C) - Quartz - SiO2 - Y: 57.09 % - d x by: 1. - WL: 1.78897 - Hexagonal - a 4.91280 - b 4.91280 - c 5.40420 - alpha 90.000 - beta 90.000 - gamma 120.000 - Primitive - P3221 (154) - 3 - 112.959 - I/Ic PDF 3.

08-BV-01

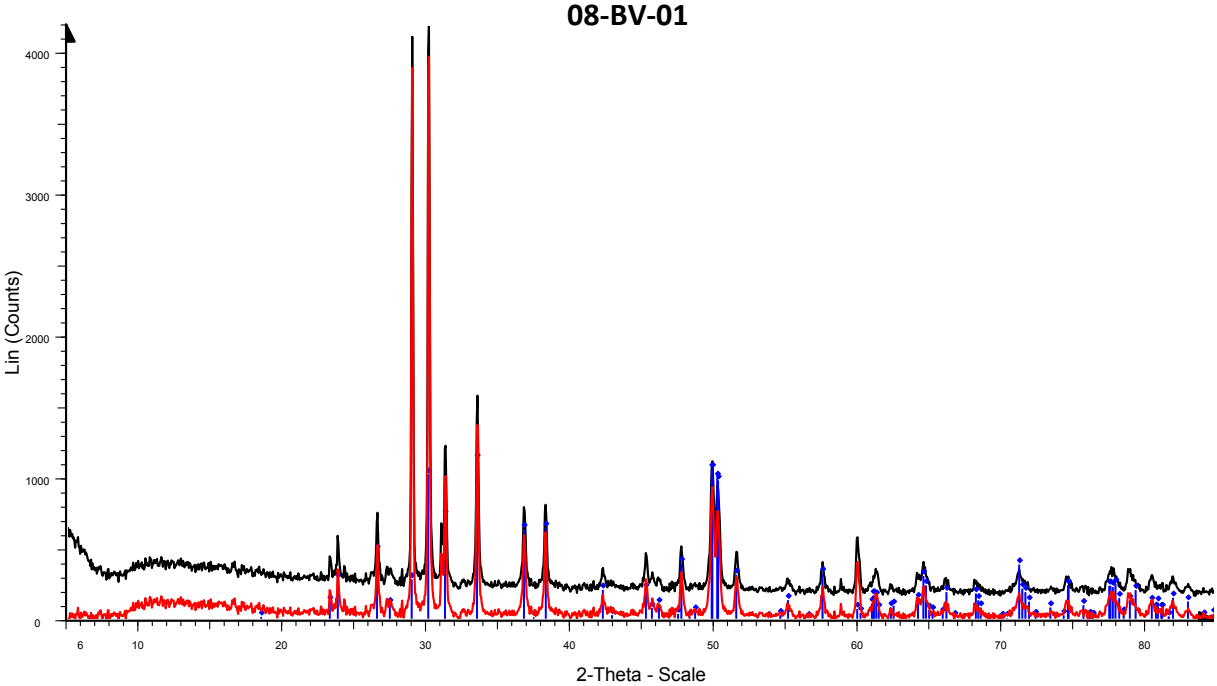

2011-533-04 - File: 2011-533-04.raw - Type: Locked Coupled - Start: 5.002 ° - End: 84.992 ° - Step: 0.051 ° - Step time: 66. s - Temp.: 25 °C (Room) - Time Started: 0 s - 2-Theta: 5.002 ° - Theta: 2.501 ° - Chi: 0.00 ° - P
Operations: Import
2011-533-04 - File: 2011-533-04.raw - Type: Locked Coupled - Start: 5.002 ° - End: 84.992 ° - Step: 0.051 ° - Step time: 66. s - Temp.: 25 °C (Room) - Time Started: 0 s - 2-Theta: 5.002 ° - Theta: 2.501 ° - Chi: 0.00 ° - P
Operations: Background 0.000,0.100 | Import
01-080-0512 (C) - Barite, syn - Ba(SO4) - Y: 26.87 % - d x by: 1. - WL: 1.78897 - Orthorhombic - a 7.14400 - b 8.86500 - c 5.44500 - alpha 90.000 - beta 90.000 - gamma 90.000 - Primitive - Pbnm (62) - 4 - 344.840 - I/Ic

APPENDIX 3-continued

X-ray Diffraction analysis

TR041

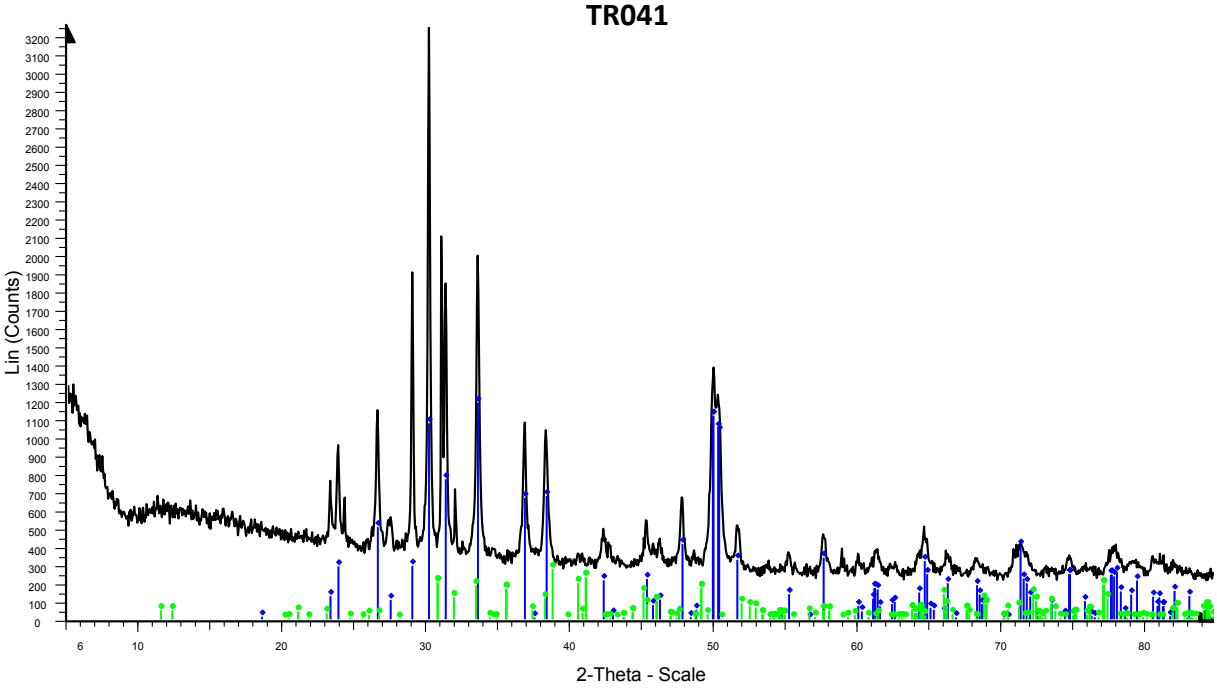

2011-533-05 - File: 2011-533-05.raw - Type: Locked Coupled - Start: 5.002 ° - End: 84.992 ° - Step: 0.051 ° - Step time: 66. s - Temp.: 25 °C (Room) - Time Started: 0 s - 2-Theta: 5.002 ° - Theta: 2.501 ° - Chi: 0.00 ° - P
Operations: Import
01-080-0512 (C) - Barite, syn - Ba(SO4) - Y: 36.55 % - d x by: 1. - WL: 1.78897 - Orthorhombic - a 7.14400 - b 8.86500 - c 5.44500 - alpha 90.000 - beta 90.000 - gamma 90.000 - Primitive - Pbnm (62) - 4 - 344.840 - I/Ic
01-085-1559 (C) - Pargasite, syn - (Na0.96Ca0.13)(Ca1.51Mn0.49)(Mg3.47Mn0.73Al0.8)(Al2.05Si5.95)O2 - Y: 8.47 % - d x by: 1. - WL: 1.78897 - Monoclinic - a 9.81200 - b 17.92600 - c 5.30800 - alpha 90.000 - beta 10

DB5

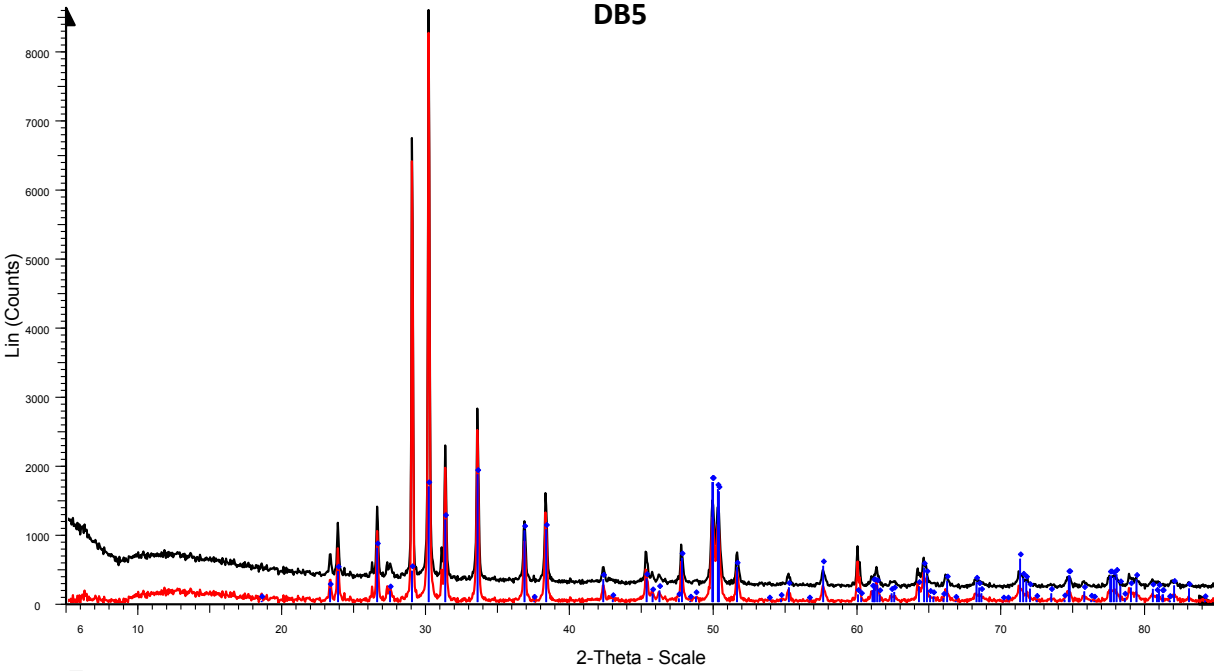

2011-533-06 - File: 2011-533-06.raw - Type: Locked Coupled - Start: 5.002 ° - End: 84.992 ° - Step: 0.051 ° - Step time: 66. s - Temp.: 25 °C (Room) - Time Started: 0 s - 2-Theta: 5.002 ° - Theta: 2.501 ° - Chi: 0.00 ° - P
Operations: Import
2011-533-06 - File: 2011-533-06.raw - Type: Locked Coupled - Start: 5.002 ° - End: 84.992 ° - Step: 0.051 ° - Step time: 66. s - Temp.: 25 °C (Room) - Time Started: 0 s - 2-Theta: 5.002 ° - Theta: 2.501 ° - Chi: 0.00 ° - P
Operations: Background 0.000,0.100 | Import
01-080-0512 (C) - Barite, syn - Ba(SO4) - Y: 21.59 % - d x by: 1. - WL: 1.78897 - Orthorhombic - a 7.14400 - b 8.86500 - c 5.44500 - alpha 90.000 - beta 90.000 - gamma 90.000 - Primitive - Pbnm (62) - 4 - 344.840 - I/Ic

APPENDIX 3—continued

X-ray Diffraction analysis

1880-318

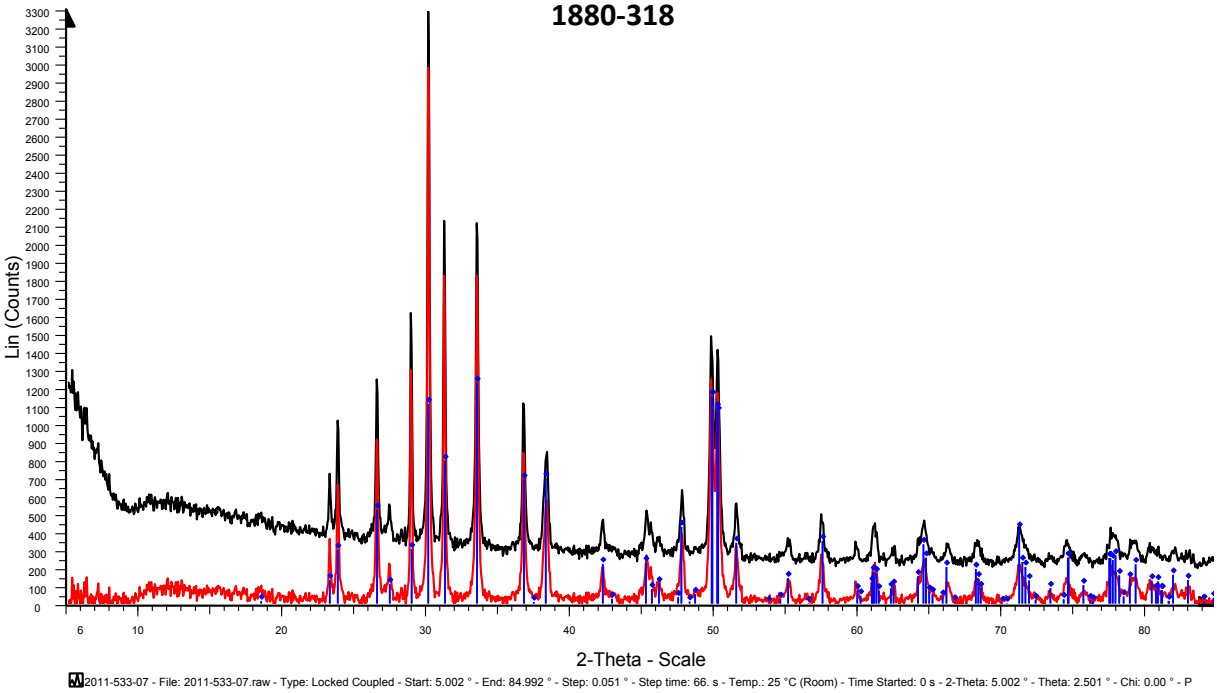

1896-45

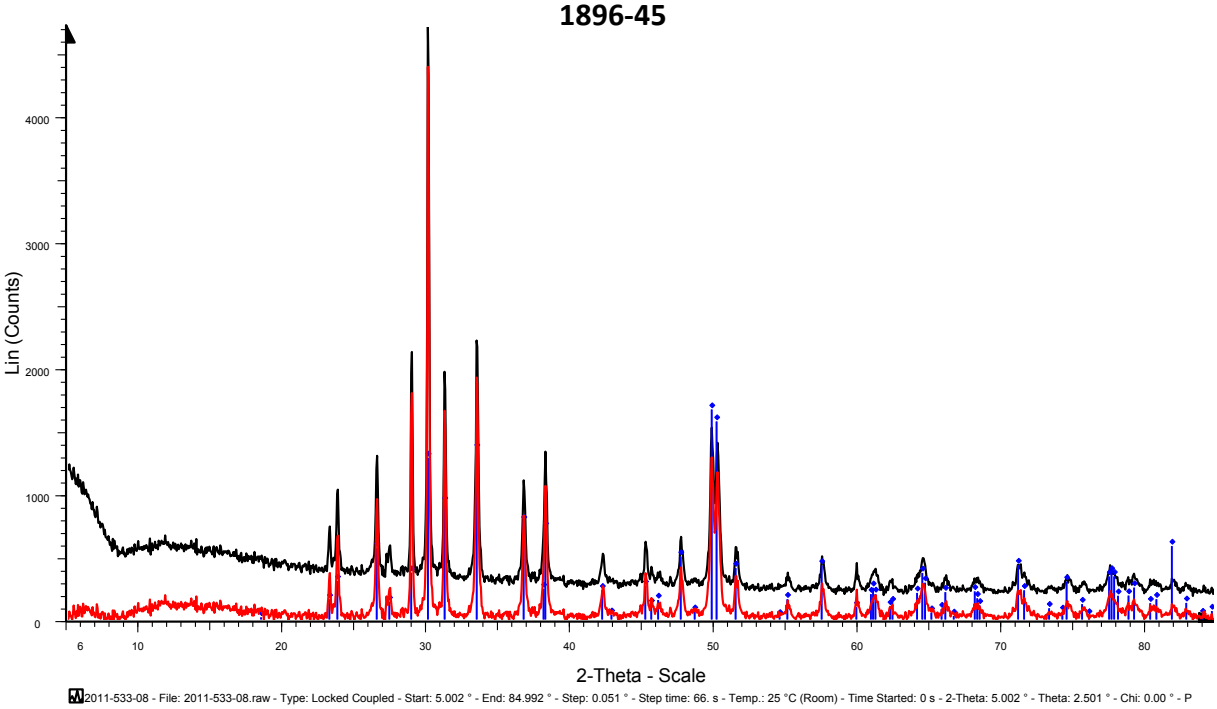

APPENDIX 3-continued

X-ray Diffraction analysis

1923-19

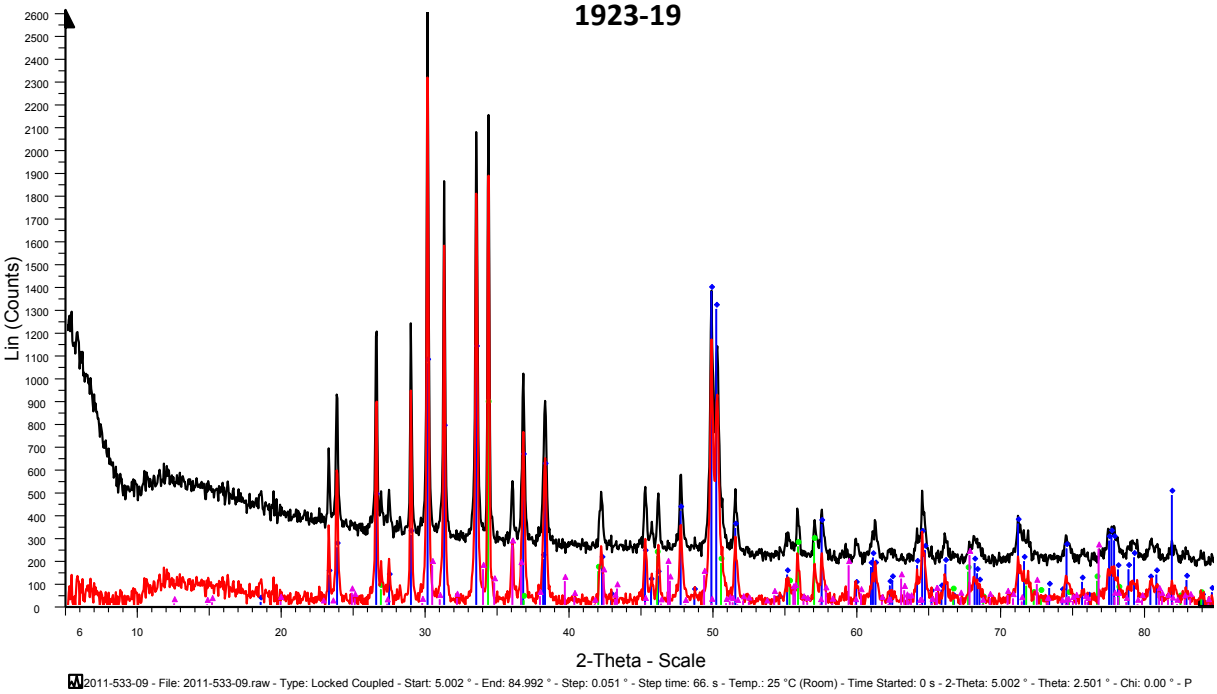

2011-533-09 - File: 2011-533-09.raw - Type: Locked Coupled - Start: 5.002 ° - End: 84.992 ° - Step: 0.051 ° - Step time: 66. s - Temp.: 25 °C (Room) - Time Started: 0 s - 2-Theta: 5.002 ° - Theta: 2.501 ° - Chi: 0.00 ° - P
Operations: Import
2011-533-09 - File: 2011-533-09.raw - Type: Locked Coupled - Start: 5.002 ° - End: 84.992 ° - Step: 0.051 ° - Step time: 66. s - Temp.: 25 °C (Room) - Time Started: 0 s - 2-Theta: 5.002 ° - Theta: 2.501 ° - Chi: 0.00 ° - P
Operations: Background 0.000,0.100 | Import
00-024-1035 (*) - Barite, syn - BaSO4 - Y: 52.90 % - d x by: 1. - WL: 1.78897 - Orthorhombic - a 7.15650 - b 8.88110 - c 5.45410 - alpha 90.000 - beta 90.000 - gamma 90.000 - Primitive - Pbnm (62) - 4 - 346.649 - I/Ic P
01-072-1652 (C) - Calcite - CaCO3 - Y: 33.60 % - d x by: 1. - WL: 1.78897 - Rhombo.H.axes - a 4.99000 - b 4.99000 - c 17.00200 - alpha 90.000 - beta 90.000 - gamma 120.000 - Primitive - R-3c (167) - 6 - 366.633 - I/Ic
01-086-1571 (C) - Davidite - Ti12.67Fe6.15La0.91Ca0.20U0.33Y0.30Mg0.24Cr0.21Sr0.09O38 - Y: 10.12 % - d x by: 1. - WL: 1.78897 - Rhombo.R.axes - a 9.19000 - b 9.19000 - c 9.19000 - alpha 68.730 - beta 68.730 -

1986-1321

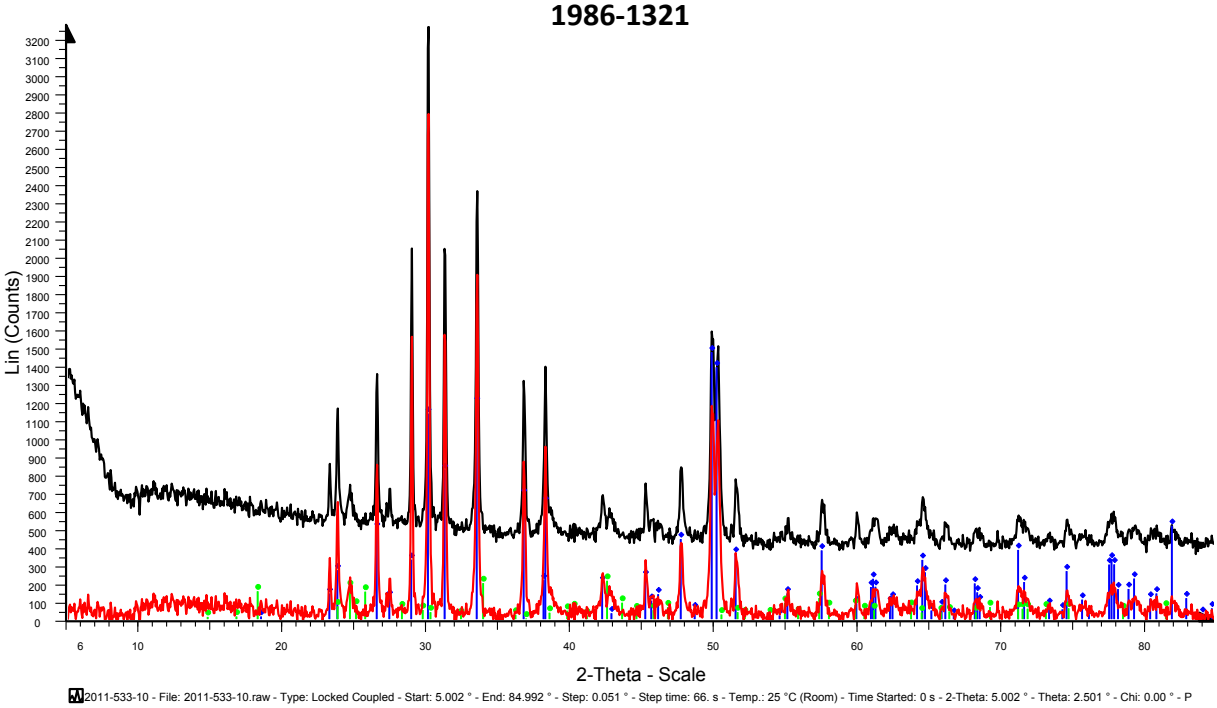

2011-533-10 - File: 2011-533-10.raw - Type: Locked Coupled - Start: 5.002 ° - End: 84.992 ° - Step: 0.051 ° - Step time: 66. s - Temp.: 25 °C (Room) - Time Started: 0 s - 2-Theta: 5.002 ° - Theta: 2.501 ° - Chi: 0.00 ° - P
Operations: Import
2011-533-10 - File: 2011-533-10.raw - Type: Locked Coupled - Start: 5.002 ° - End: 84.992 ° - Step: 0.051 ° - Step time: 66. s - Temp.: 25 °C (Room) - Time Started: 0 s - 2-Theta: 5.002 ° - Theta: 2.501 ° - Chi: 0.00 ° - P
Operations: Background 0.000,0.100 | Import
00-024-1035 (*) - Barite, syn - BaSO4 - Y: 45.08 % - d x by: 1. - WL: 1.78897 - Orthorhombic - a 7.15650 - b 8.88110 - c 5.45410 - alpha 90.000 - beta 90.000 - gamma 90.000 - Primitive - Pbnm (62) - 4 - 346.649 - I/Ic P
00-025-1489 (I) - Anthoinite - AlWO3(OH)3 - Y: 6.47 % - d x by: 1. - WL: 1.78897 - Triclinic - a 9.51000 - b 9.23000 - c 13.05000 - alpha 93.330 - beta 120.000 - gamma 88.330 - Primitive - P*,-1 (2) - 10 - 990.352 - I/Ic P

X-ray Diffraction analysis

1986-1334

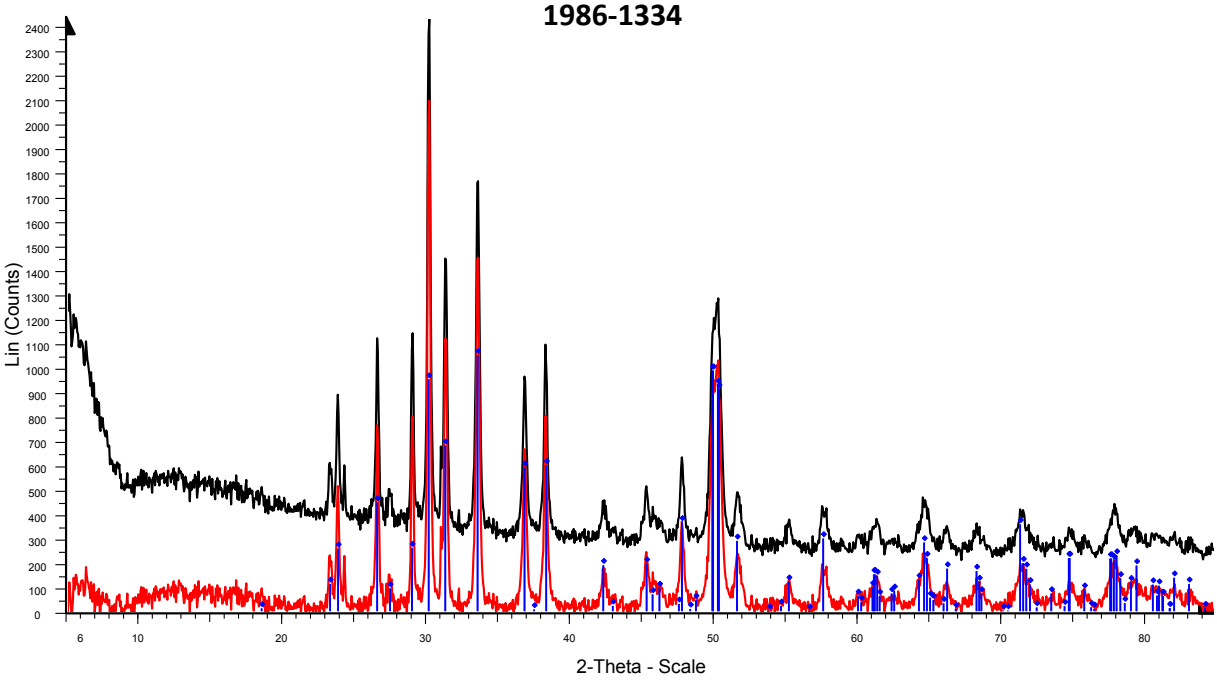

2011-533-11 - File: 2011-533-11.raw - Type: Locked Coupled - Start: 5.002 ° - End: 84.992 ° - Step: 0.051 ° - Step time: 66. s - Temp.: 25 °C (Room) - Time Started: 0 s - 2-Theta: 5.002 ° - Theta: 2.501 ° - Chi: 0.00 ° - P
Operations: Import
2011-533-11 - File: 2011-533-11.raw - Type: Locked Coupled - Start: 5.002 ° - End: 84.992 ° - Step: 0.051 ° - Step time: 66. s - Temp.: 25 °C (Room) - Time Started: 0 s - 2-Theta: 5.002 ° - Theta: 2.501 ° - Chi: 0.00 ° - P
Operations: Background 0.000,0.100 | Import
01-080-0512 (C) - Barite, syn - Ba(SO4) - Y: 43.27 % - d x by: 1. - WL: 1.78897 - Orthorhombic - a 7.14400 - b 8.86500 - c 5.44500 - alpha 90.000 - beta 90.000 - gamma 90.000 - Primitive - Pbnm (62) - 4 - 344.840 - I/Ic

08-LON-01

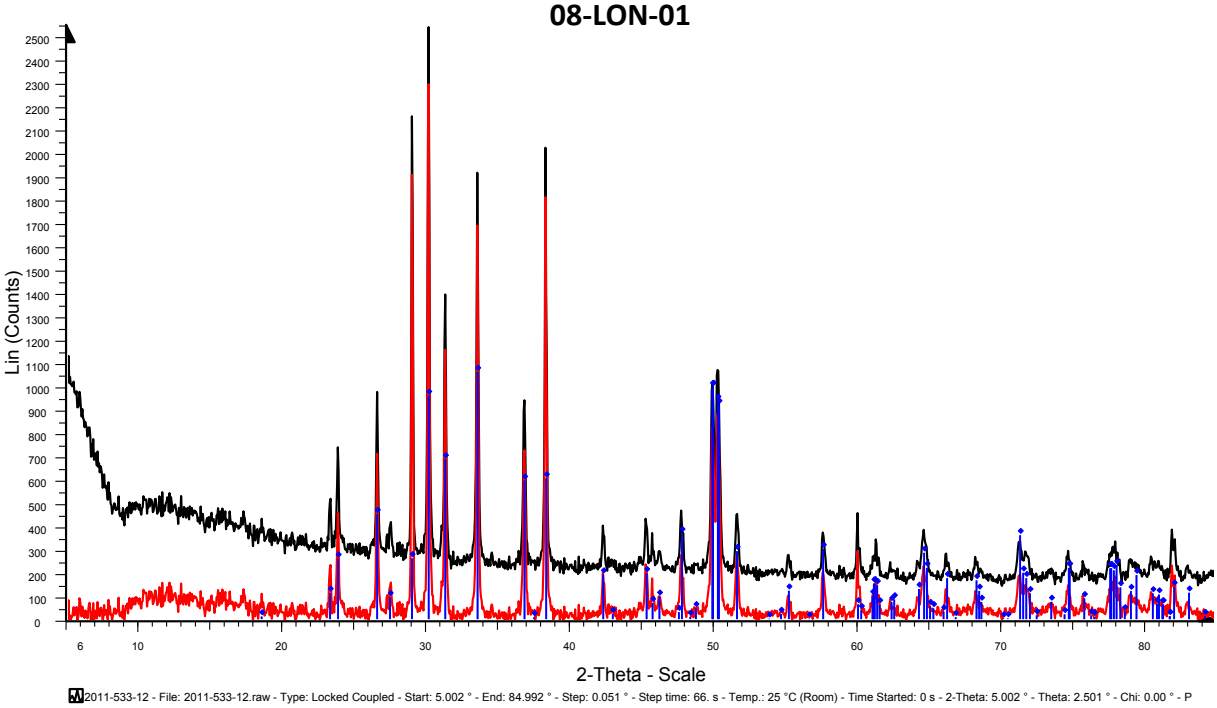

2011-533-12 - File: 2011-533-12.raw - Type: Locked Coupled - Start: 5.002 ° - End: 84.992 ° - Step: 0.051 ° - Step time: 66. s - Temp.: 25 °C (Room) - Time Started: 0 s - 2-Theta: 5.002 ° - Theta: 2.501 ° - Chi: 0.00 ° - P
Operations: Import
2011-533-12 - File: 2011-533-12.raw - Type: Locked Coupled - Start: 5.002 ° - End: 84.992 ° - Step: 0.051 ° - Step time: 66. s - Temp.: 25 °C (Room) - Time Started: 0 s - 2-Theta: 5.002 ° - Theta: 2.501 ° - Chi: 0.00 ° - P
Operations: Background 0.000,0.100 | Import
01-080-0512 (C) - Barite, syn - Ba(SO4) - Y: 41.76 % - d x by: 1. - WL: 1.78897 - Orthorhombic - a 7.14400 - b 8.86500 - c 5.44500 - alpha 90.000 - beta 90.000 - gamma 90.000 - Primitive - Pbnm (62) - 4 - 344.840 - I/Ic

APPENDIX 4

Barium elution curves

The elution curves below show the amount (mg) of barium as passed through the C18 Sep-Pak cartridge. The concentration is constant, the total amount corresponds with amounts of Ba^{2+} present in solution as calculated. The error bars in the elution graphs indicate a 10% error that was derived from the ICP-OES since the concentration Ba^{2+} was too high to accurately measure. The blue dot in the graph (at 50mL) indicates the original concentration of Ba^{2+} (in mg) as measured before the c18 cartridge was attached to the tube.

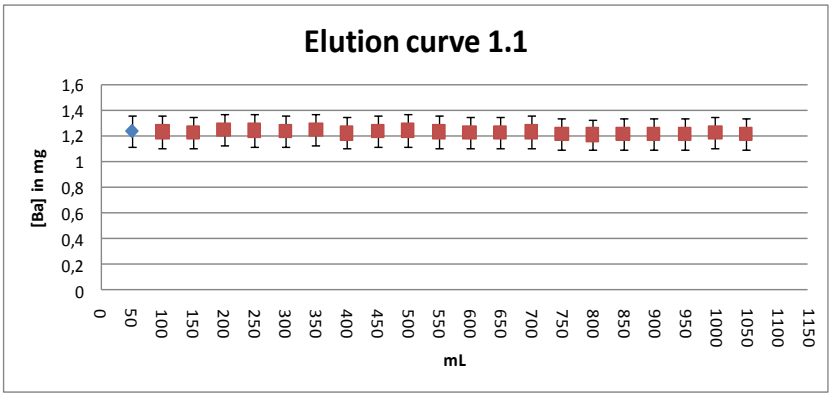

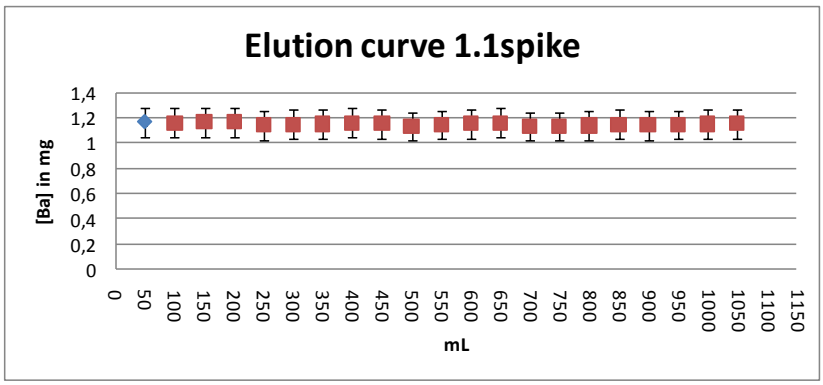

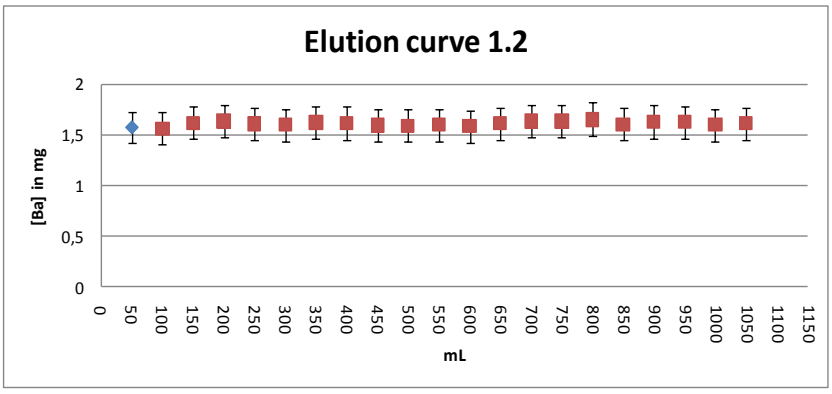

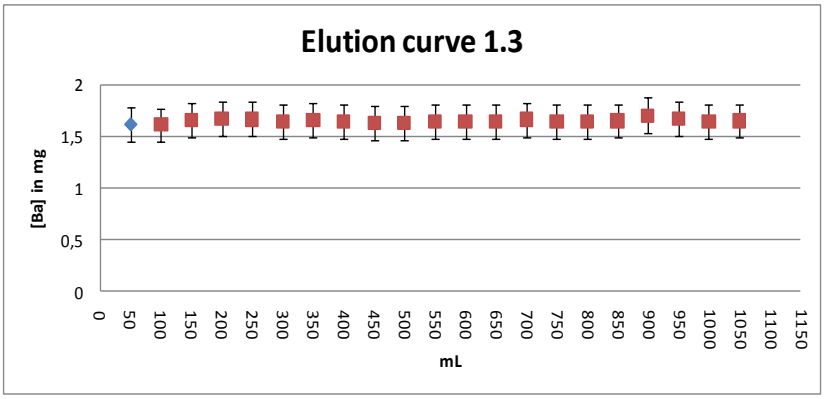

APPENDIX 5A

Barite powder—REE elution curves - 5ug spike

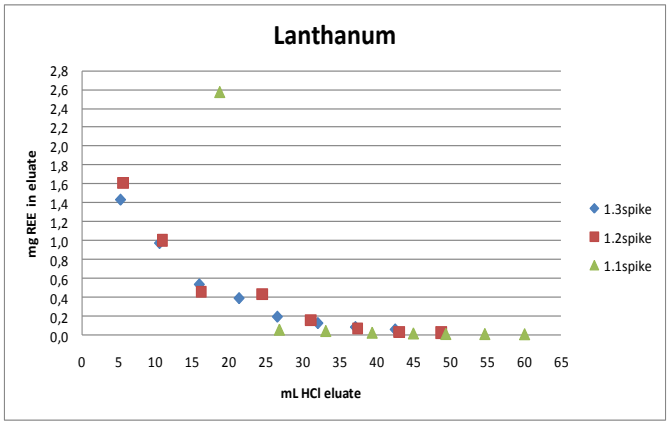

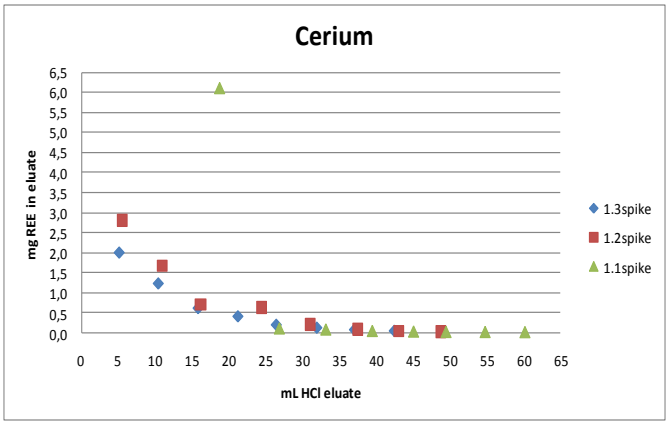

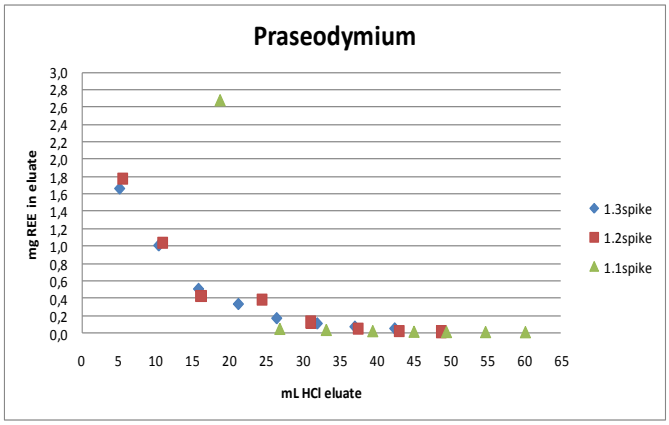

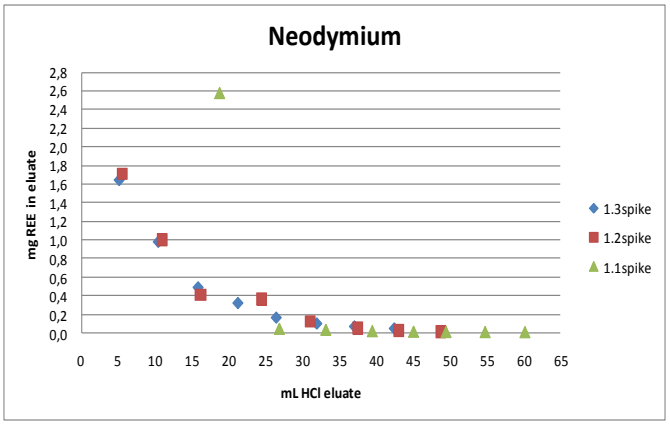

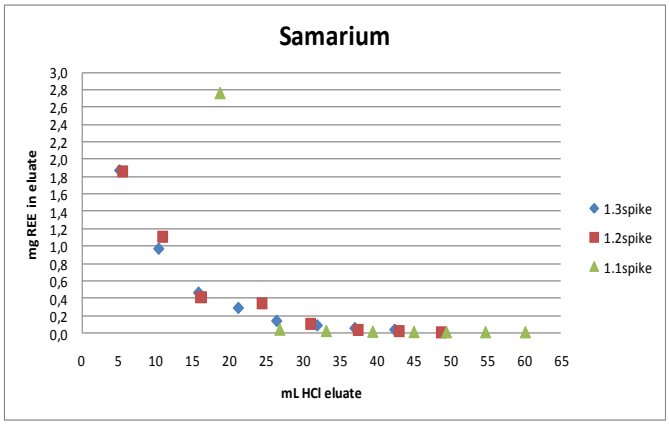

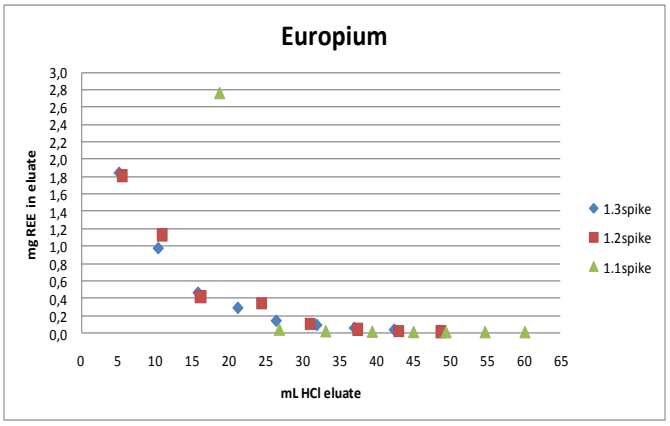

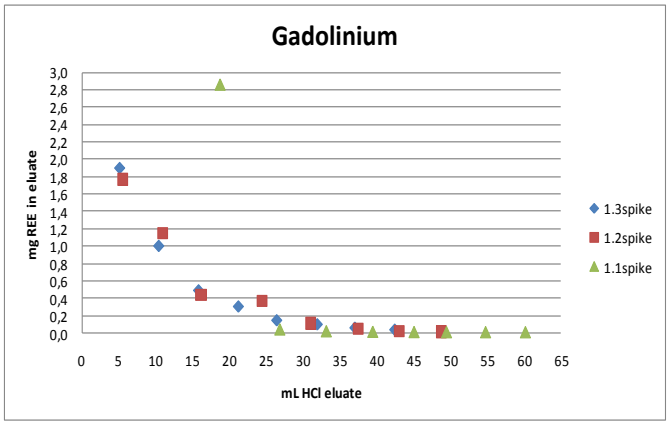

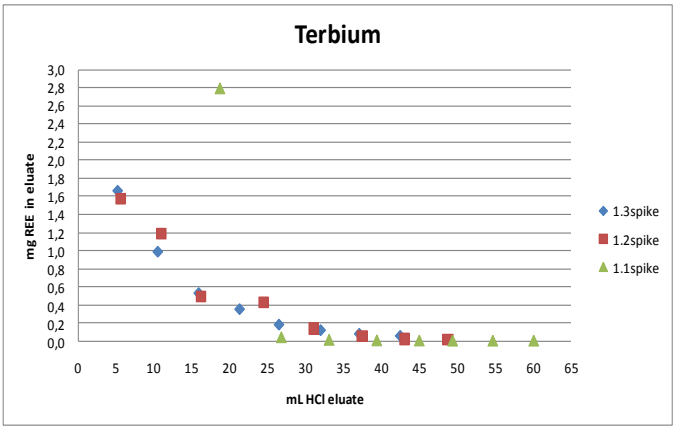

APPENDIX 5A– continued

Barite powder—REE elution curves - 5ug spike

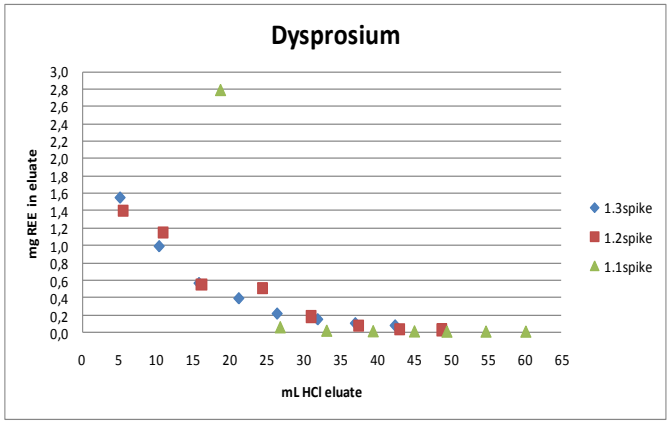

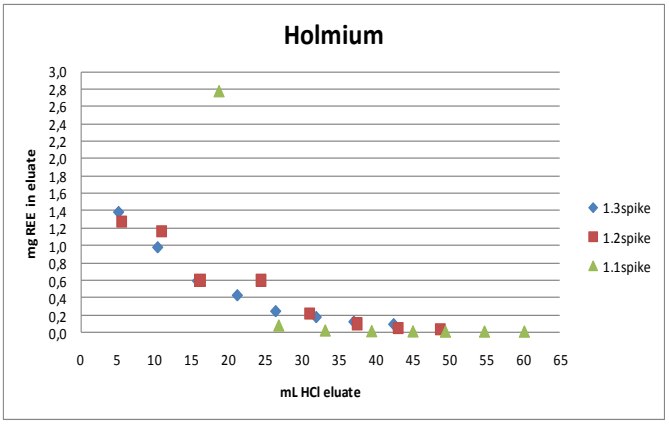

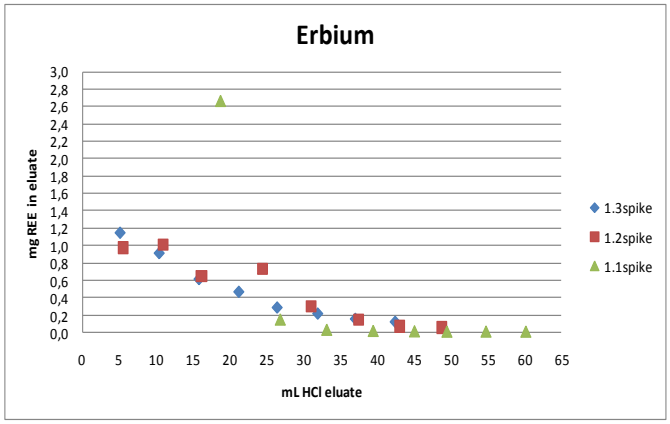

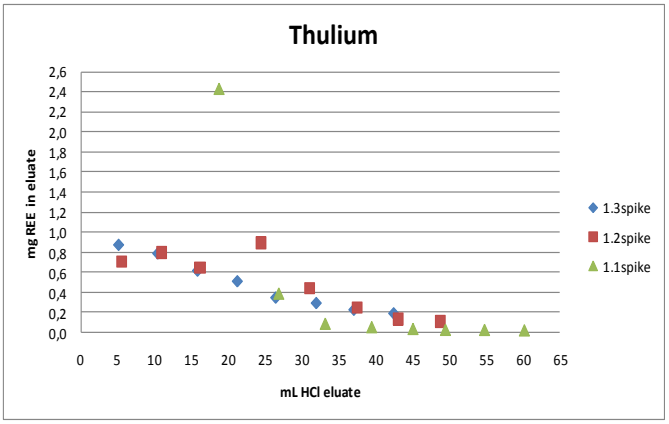

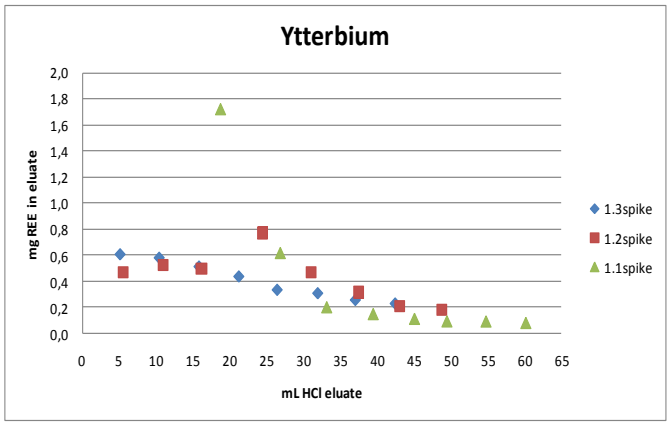

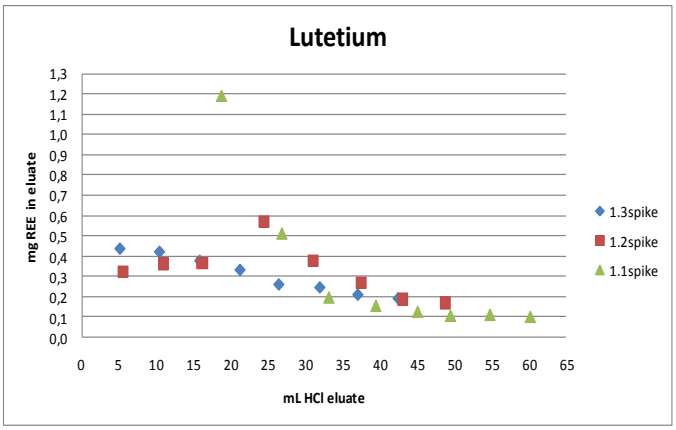

APPENDIX 5B

REE elution curves - 2.5ug spike

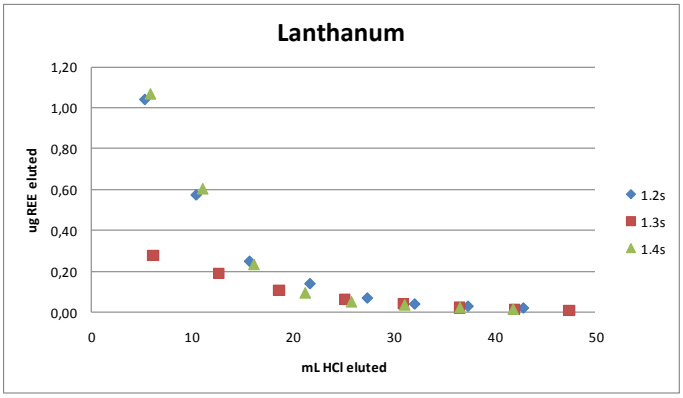

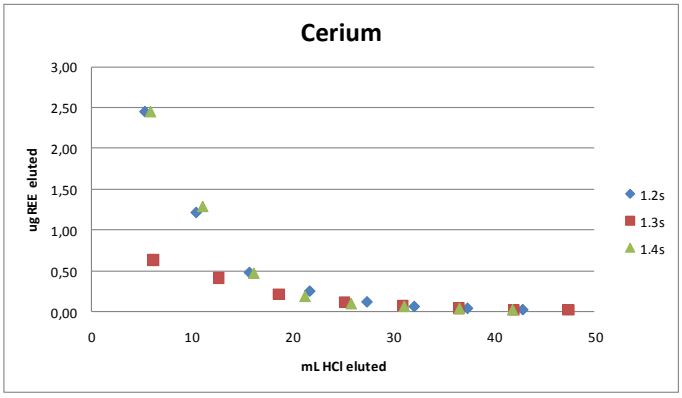

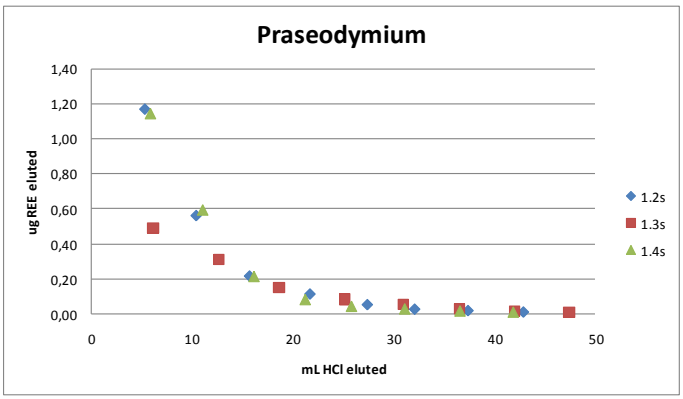

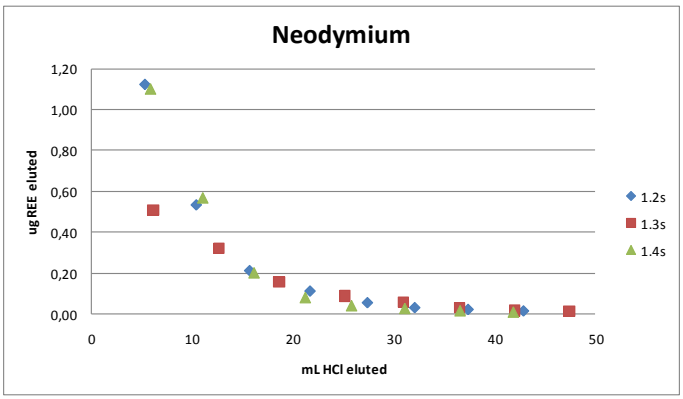

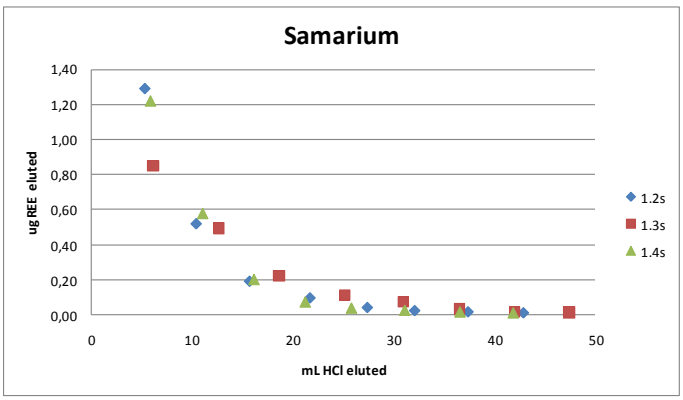

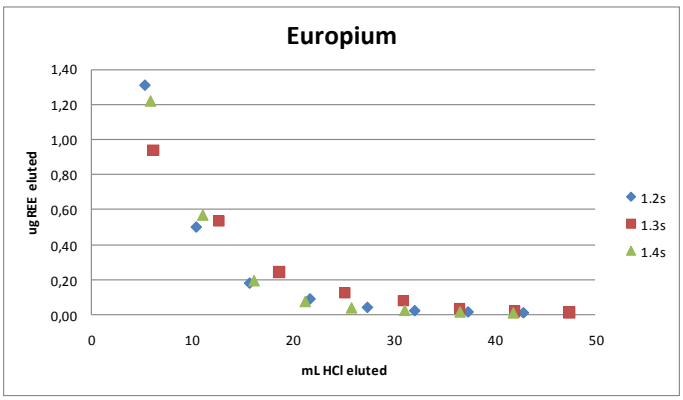

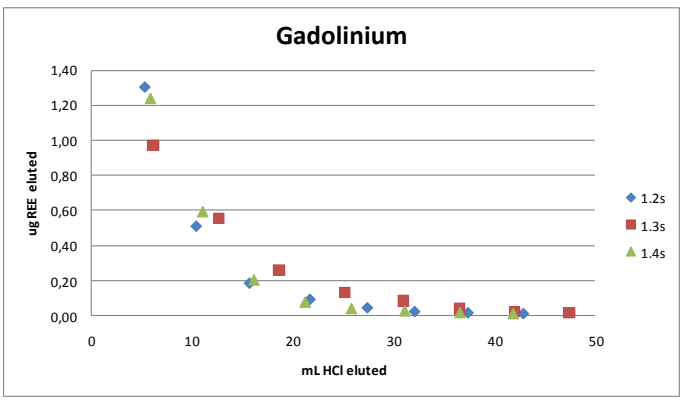

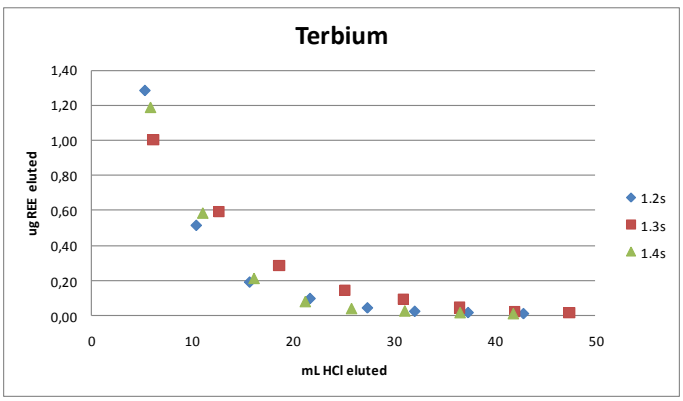

APPENDIX 5B

REE elution curves - 2.5ug spike

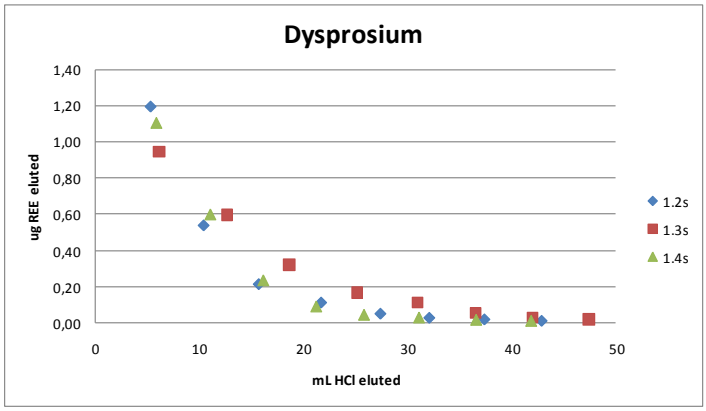

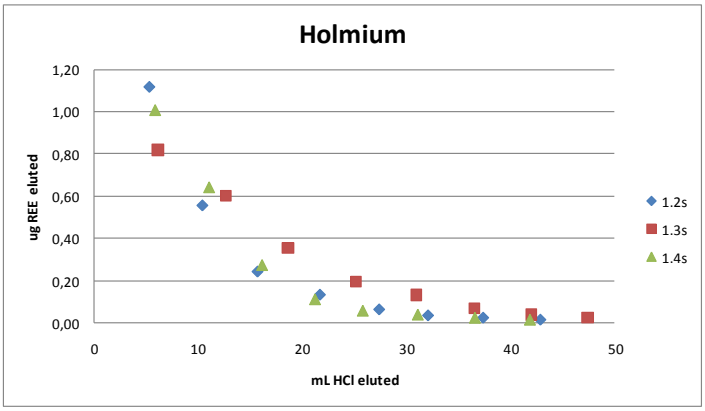

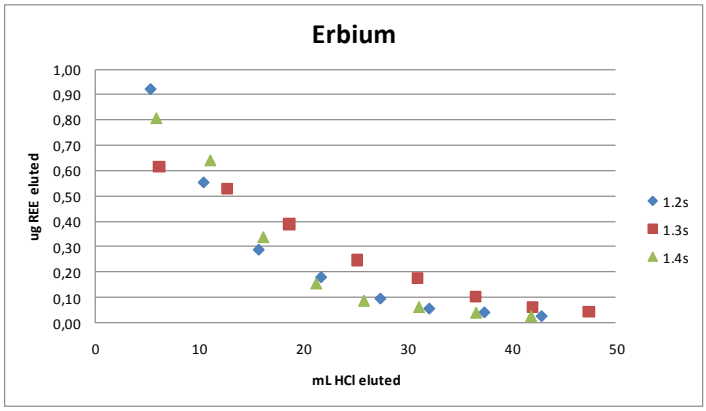

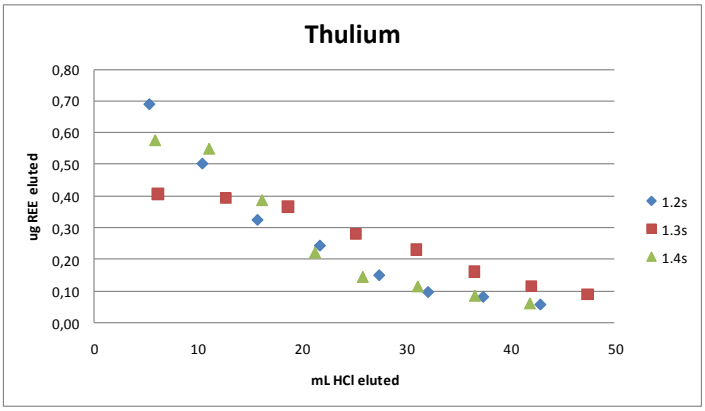

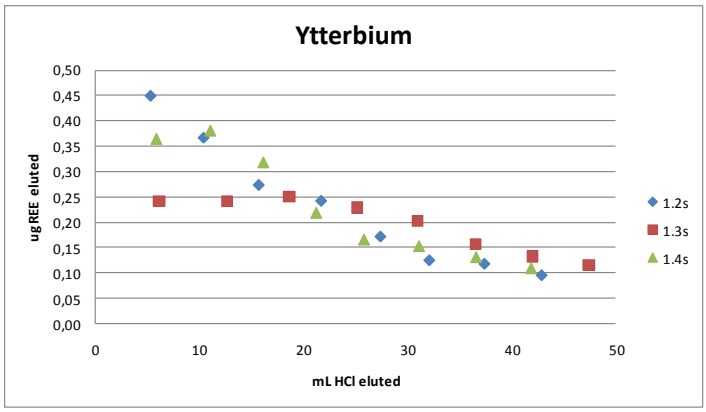

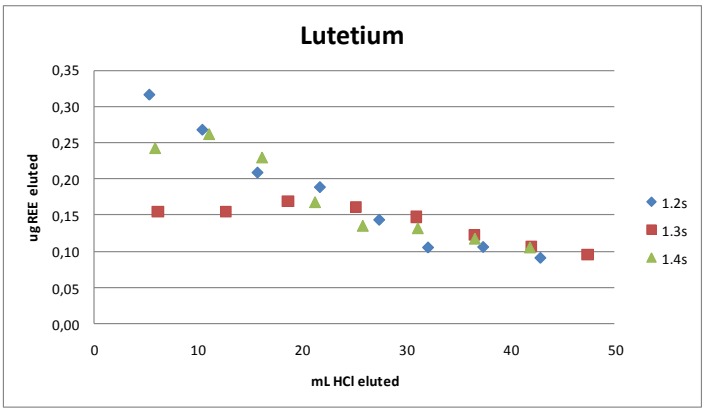

APPENDIX 6

High Resolution Mass Spectrum scan.

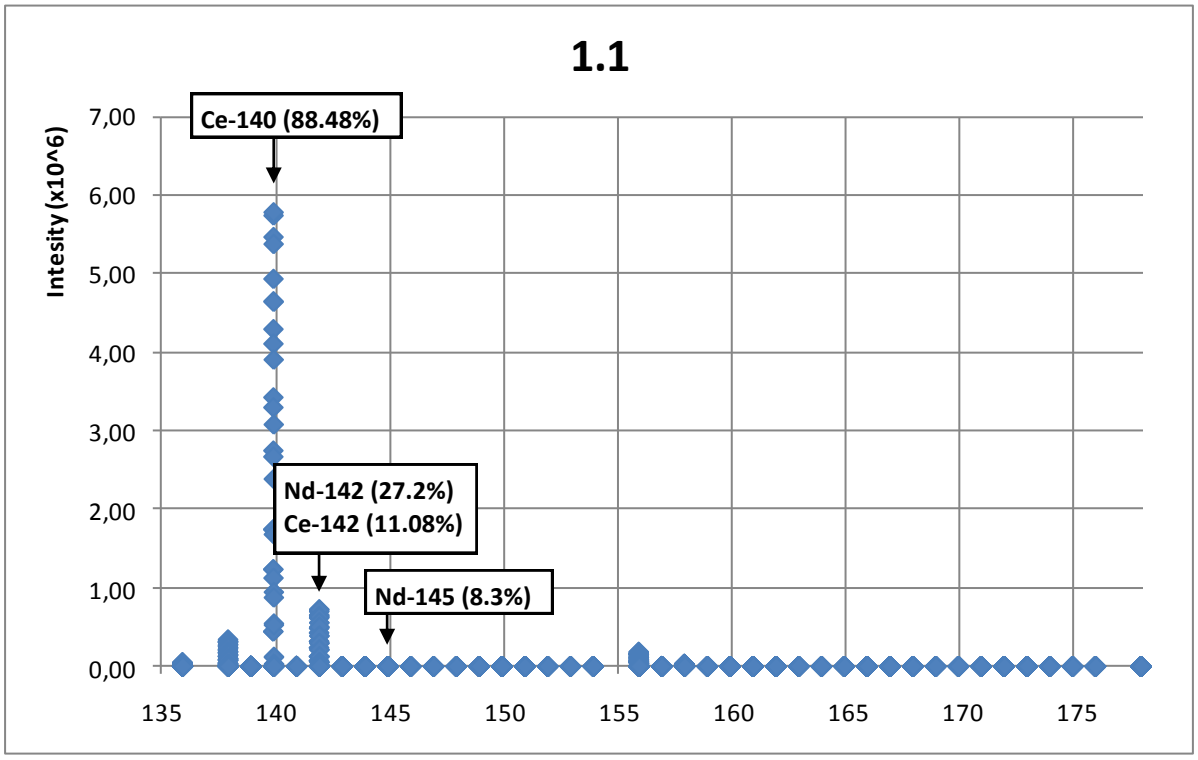

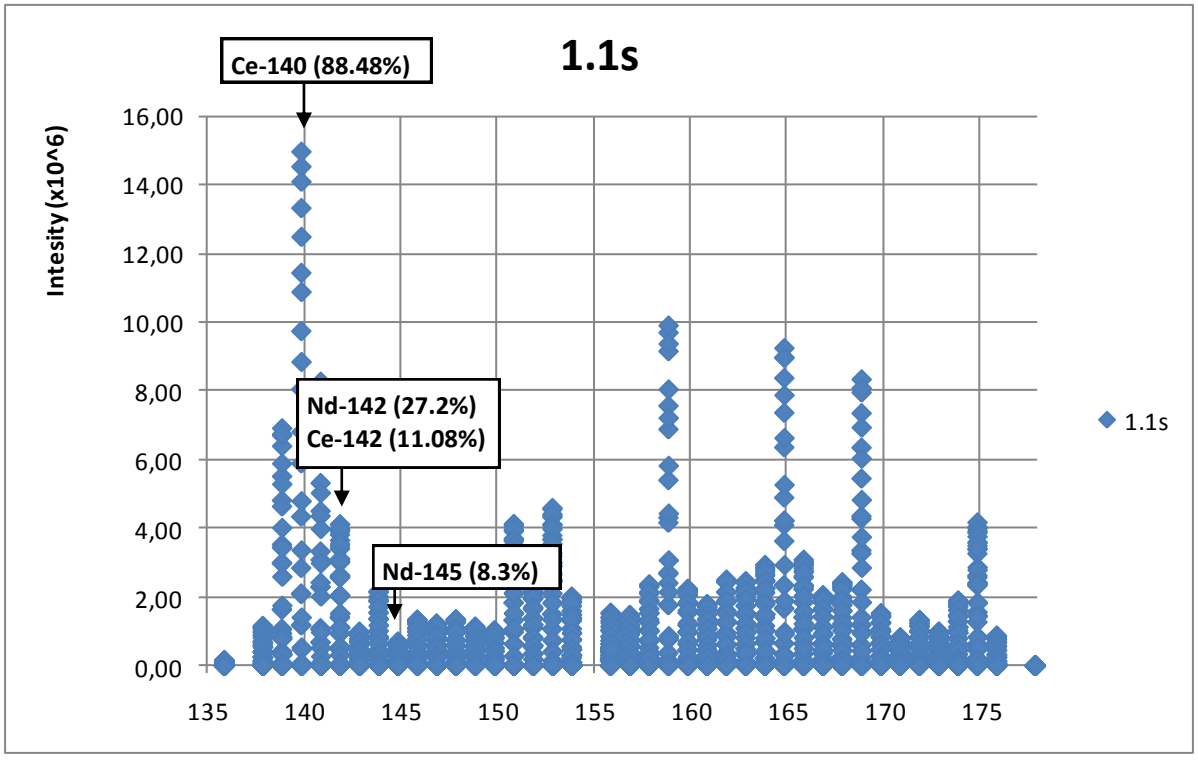

APPENDIX 6—continued

High Resolution Mass Spectrum scan.

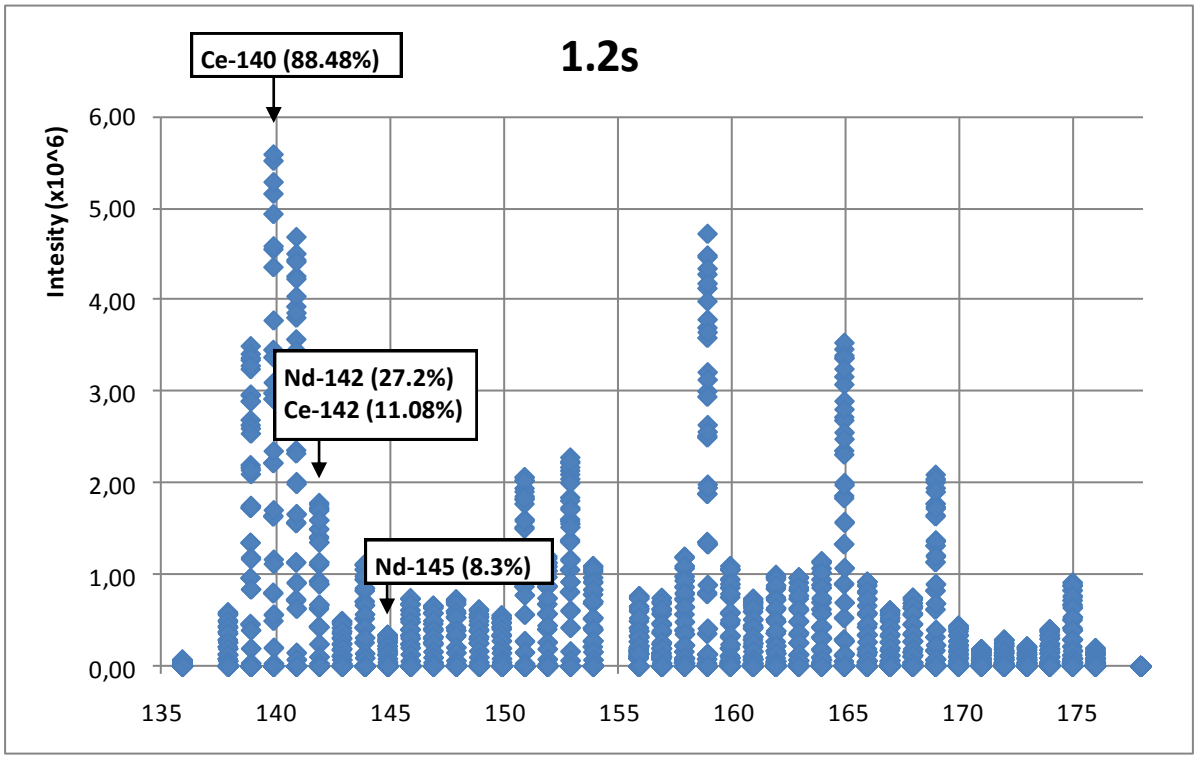

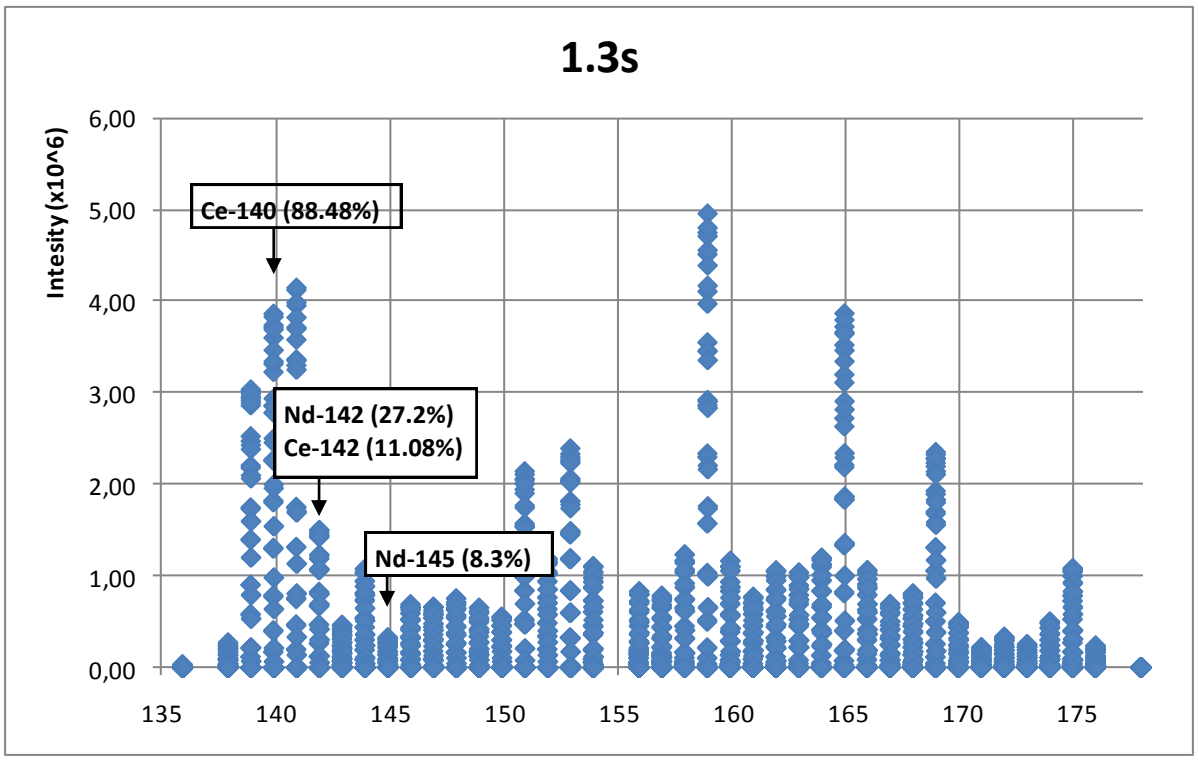

APPENDIX 6—continued

High Resolution Mass Spectrum scan.

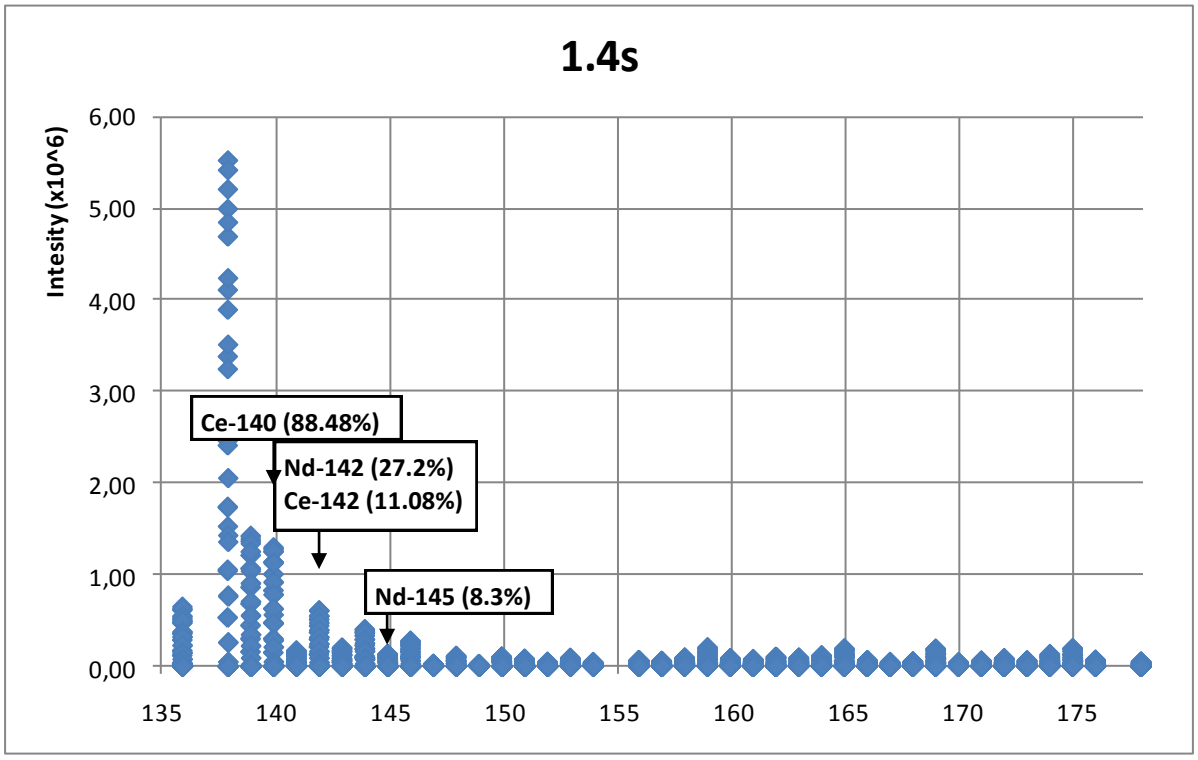

APPENDIX 7

REE elution curves for ICP-MS analysis after Ion Exchange Chromatography for sample TR041

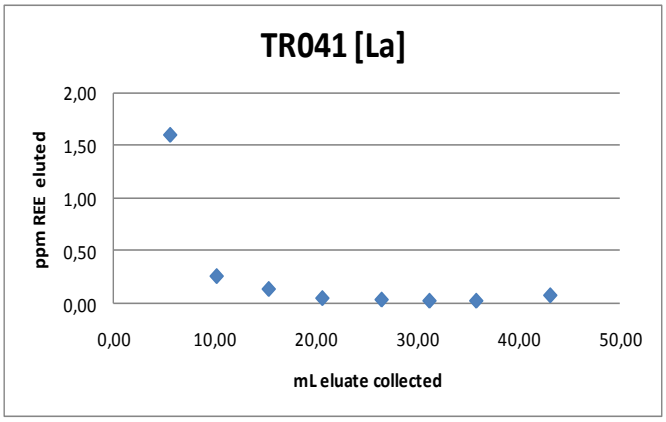

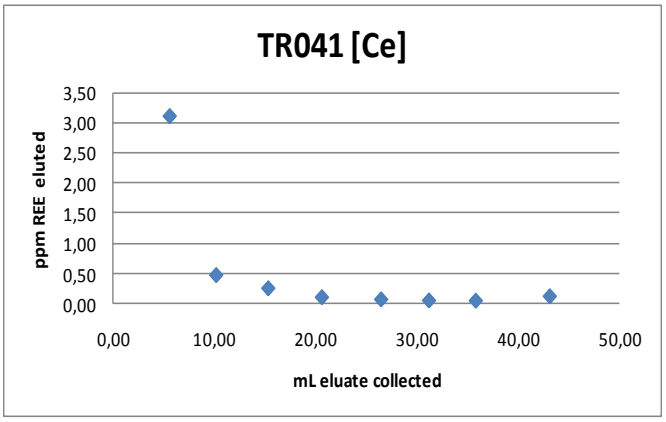

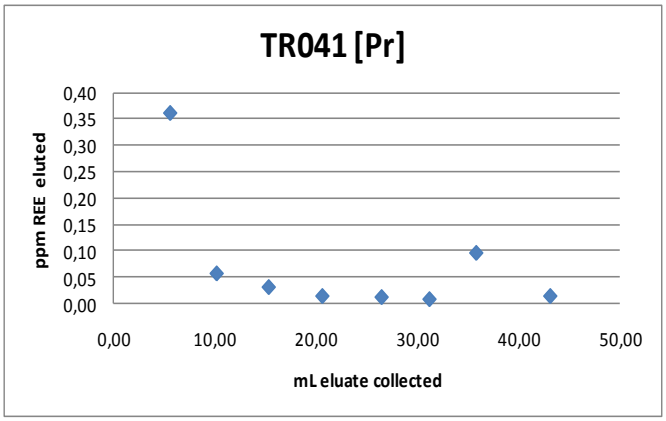

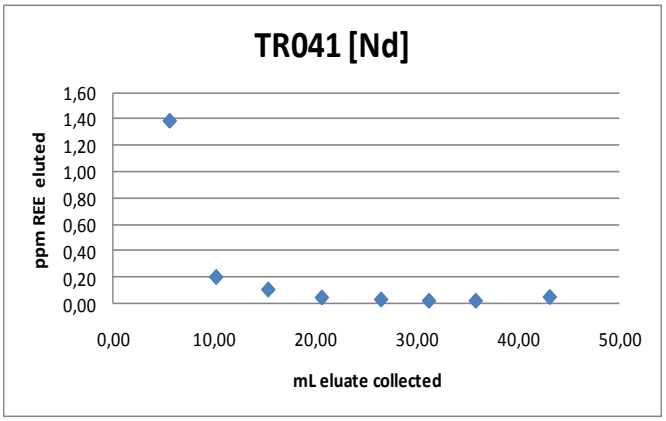

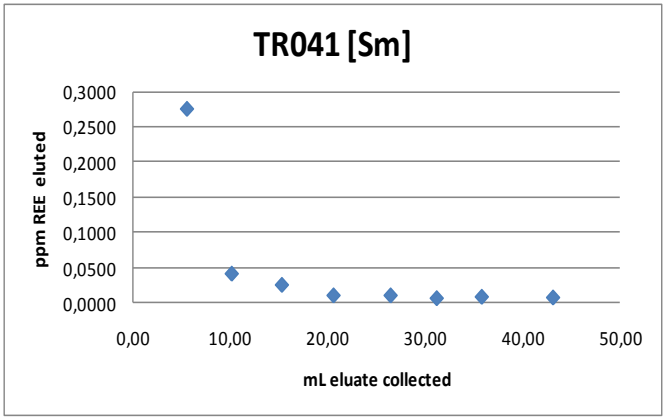

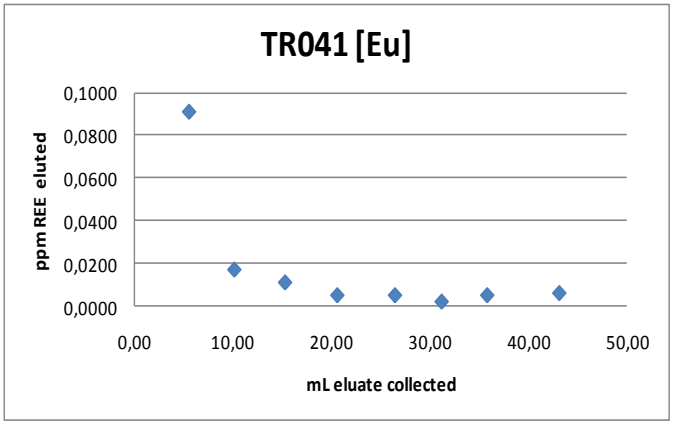

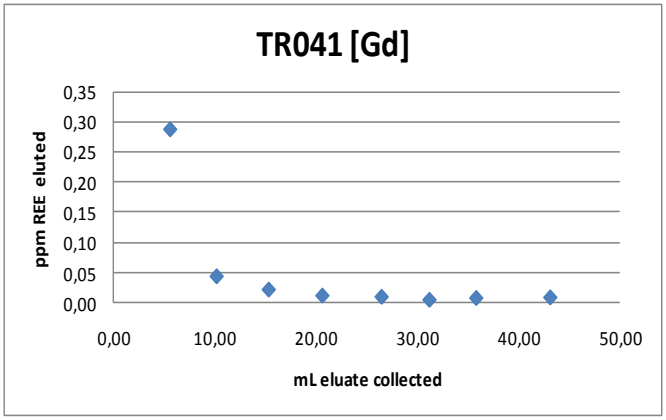

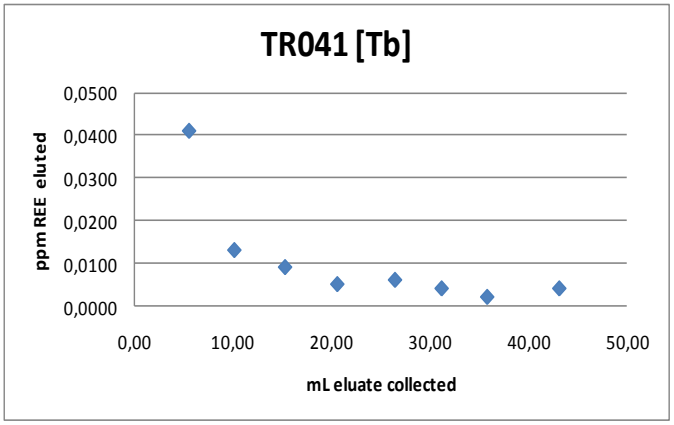

APPENDIX 7—continued

REE elution curves for ICP-MS analysis after Ion Exchange Chromatography for sample TR041

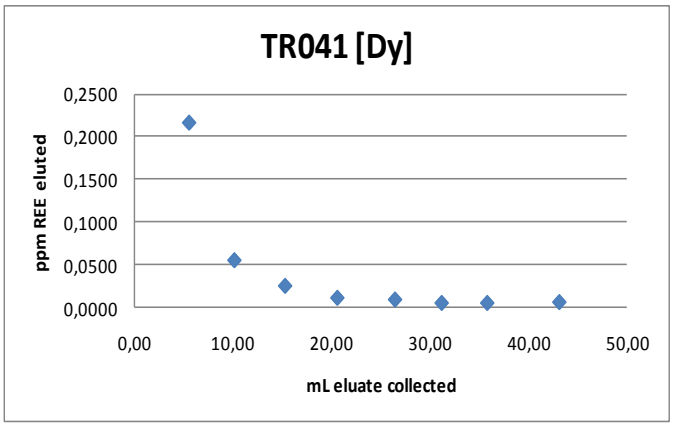

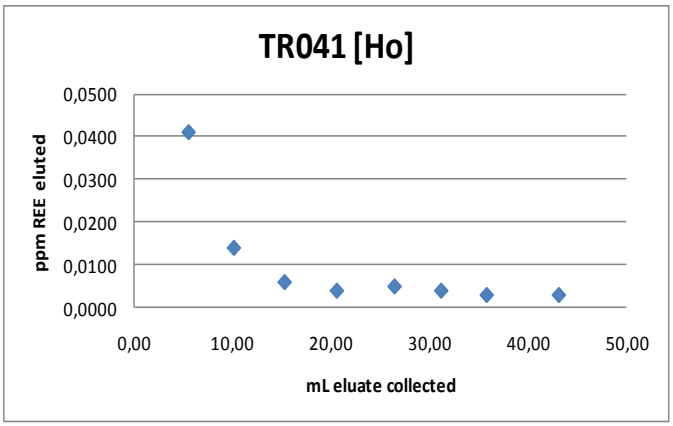

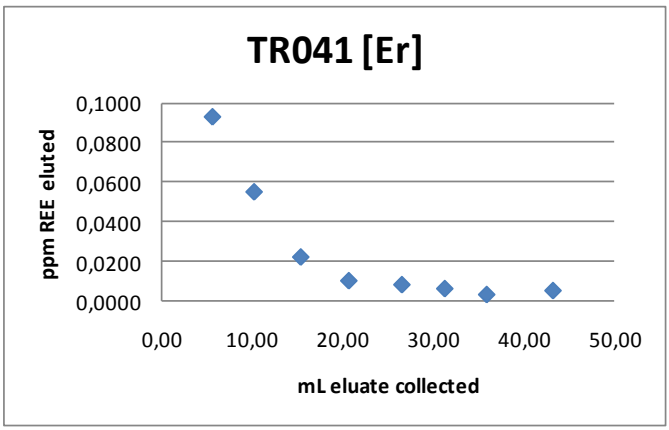

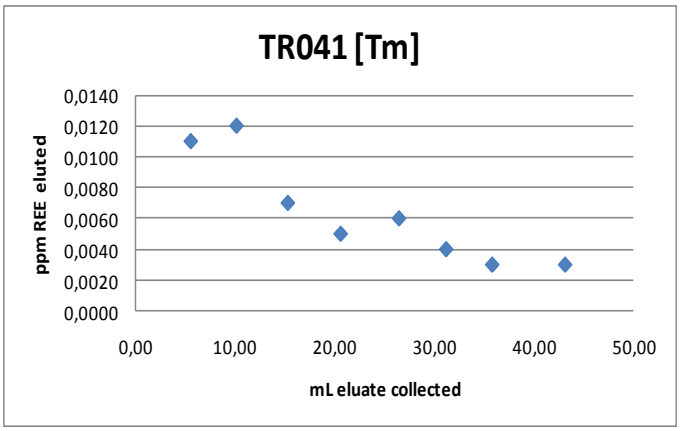

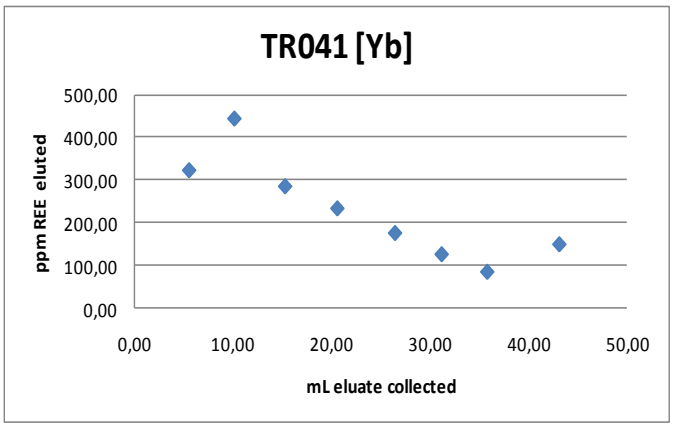

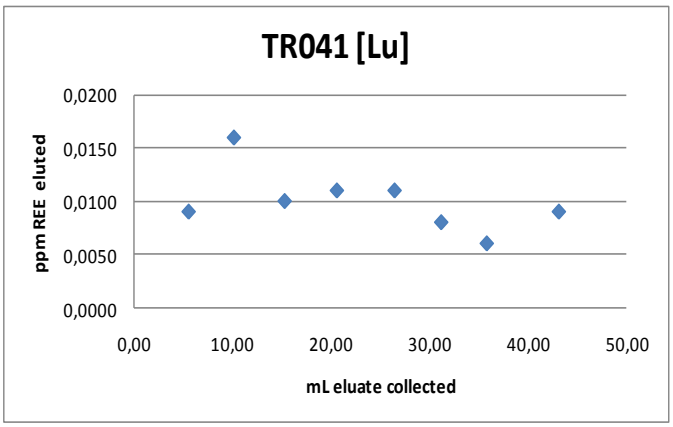

APPENDIX 8A

PAAS normalized REE graphs for Ion Exchange Chromatography method.

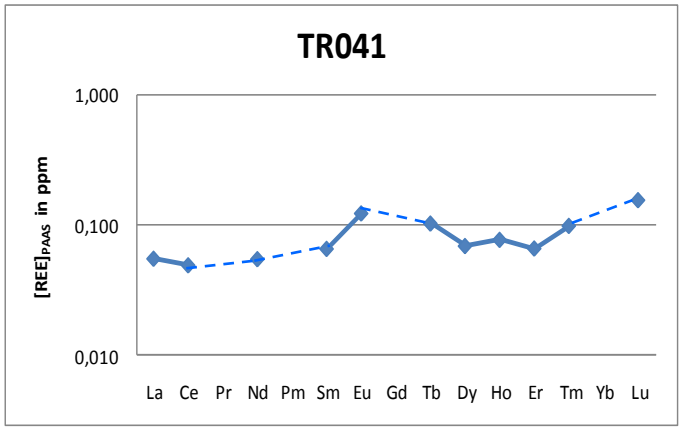

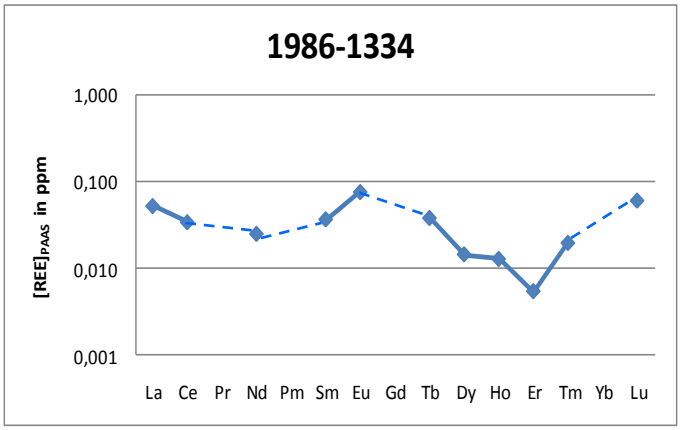

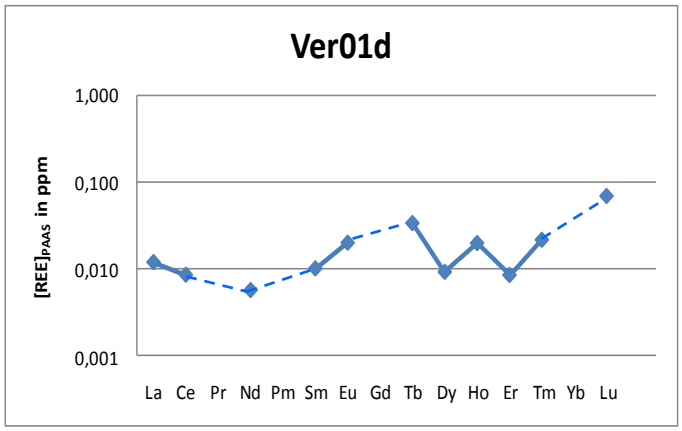

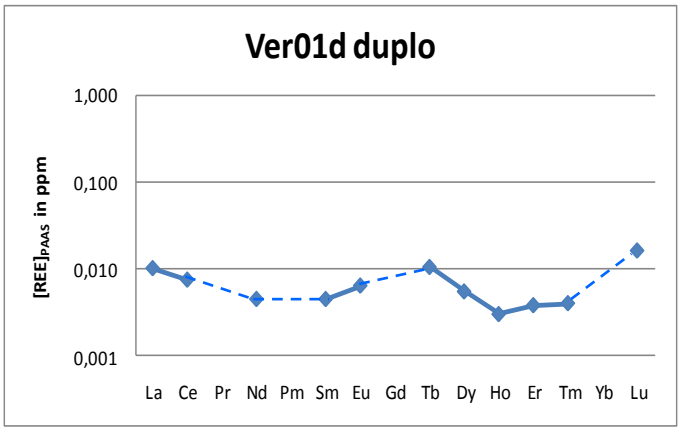

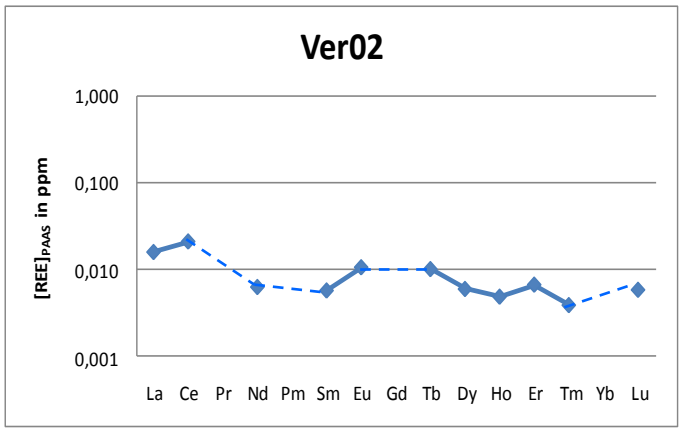

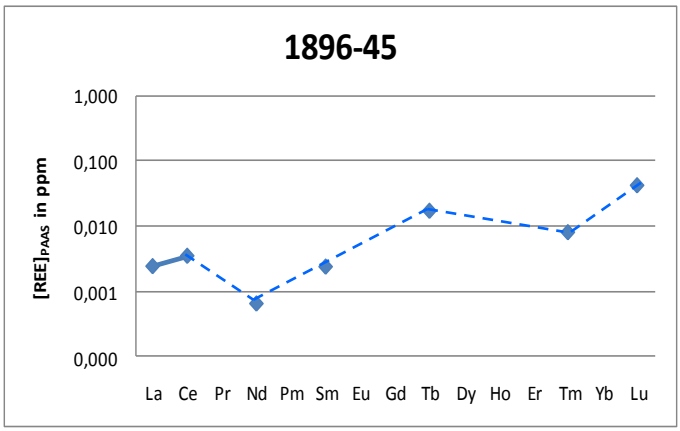

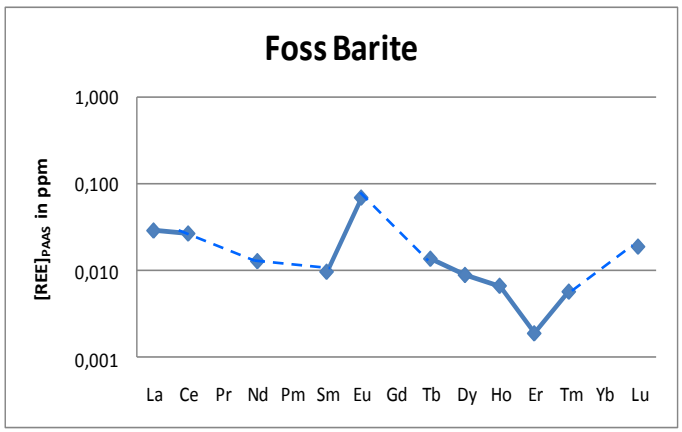

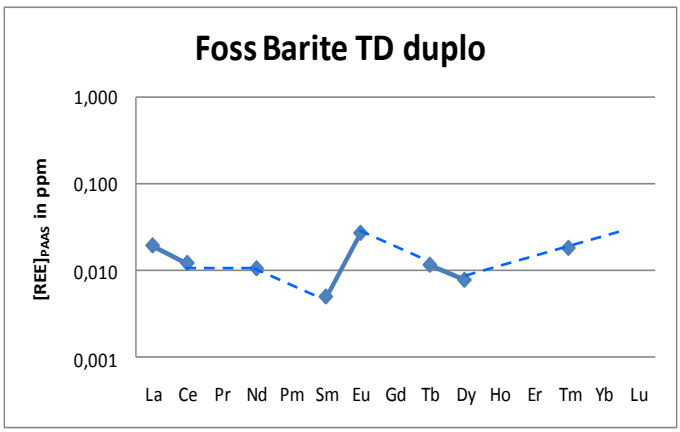

APPENDIX 8A—continued

PAAS normalized REE graphs for Ion Exchange Chromatography method.

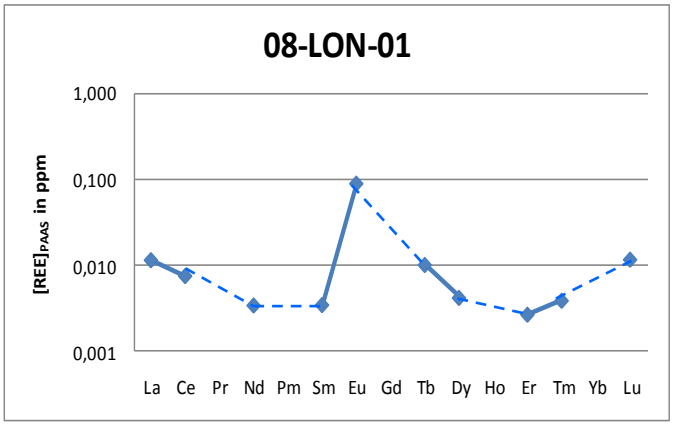

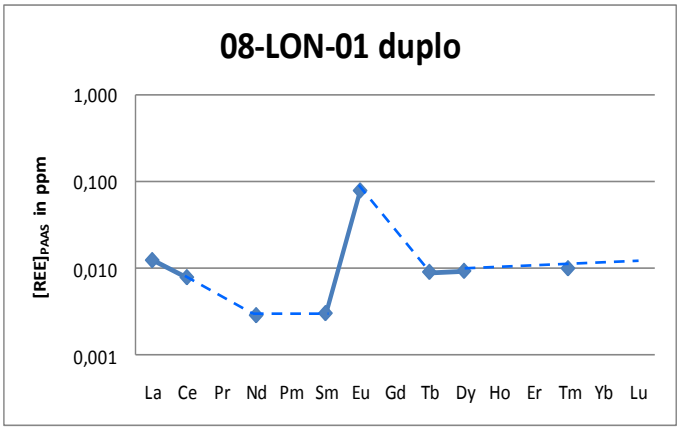

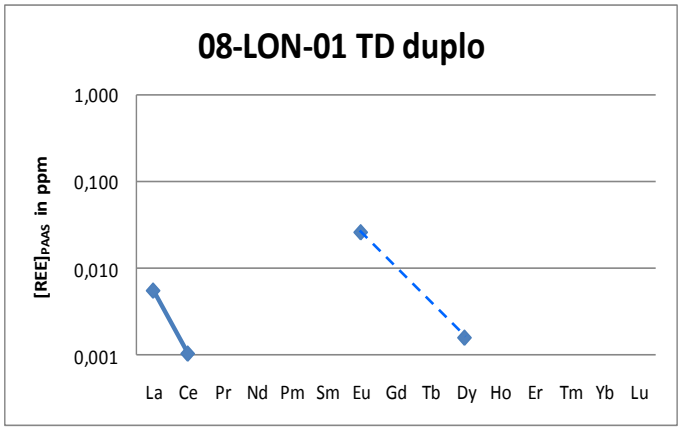

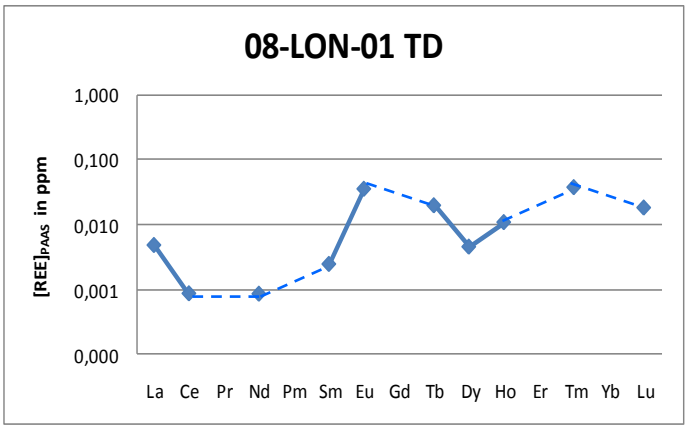

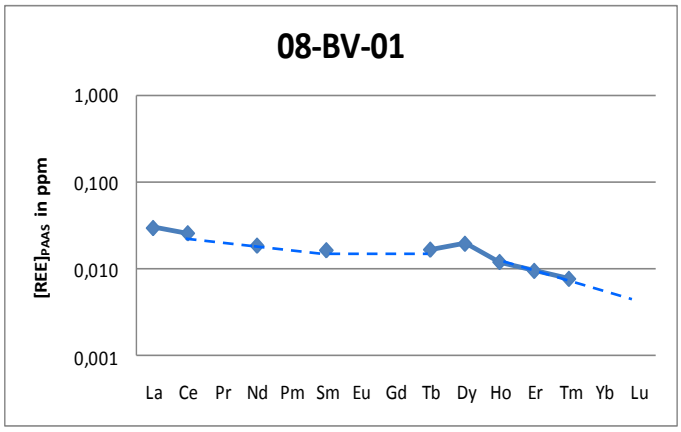

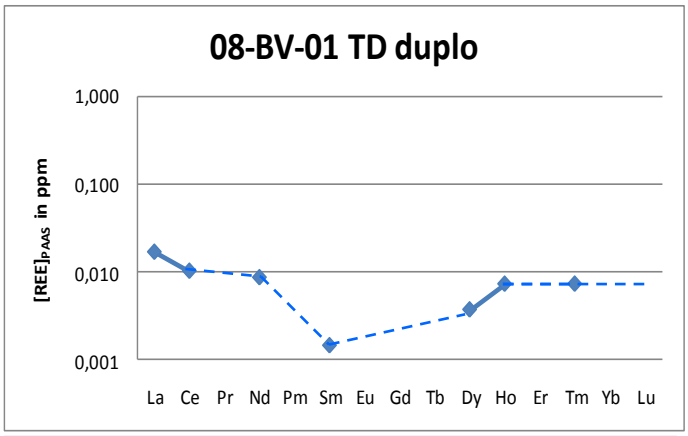

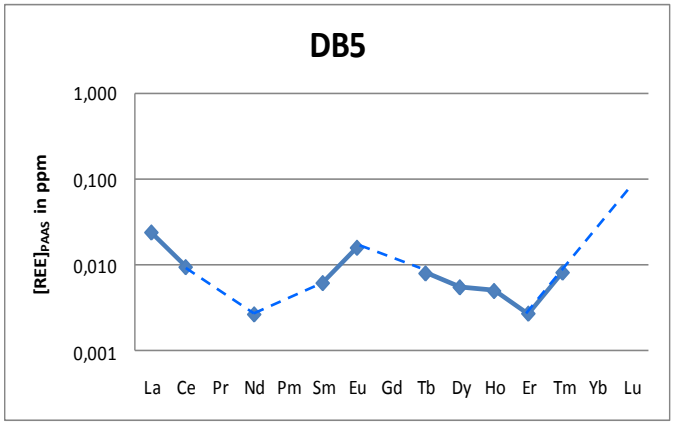

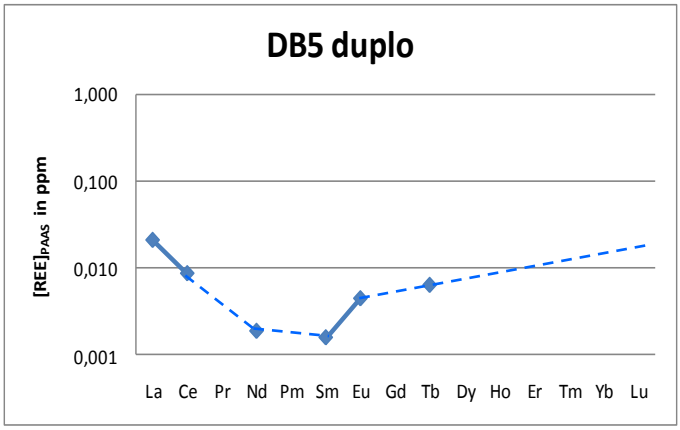

APPENDIX 8A—continued

PAAS normalized REE graphs for Ion Exchange Chromatography method.

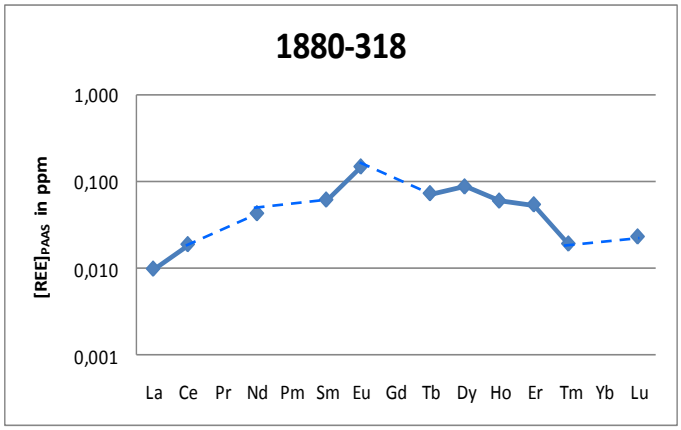

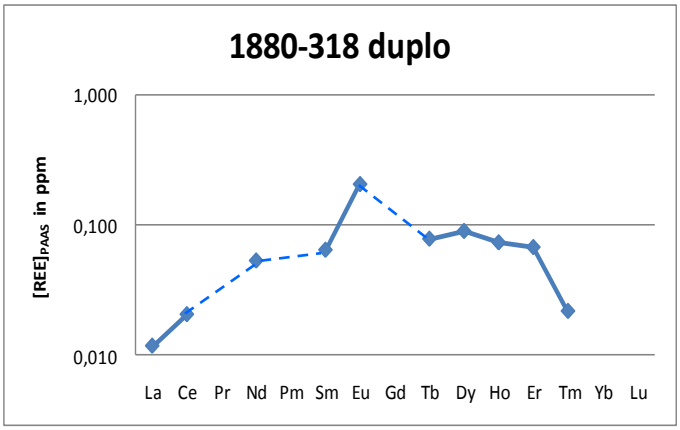

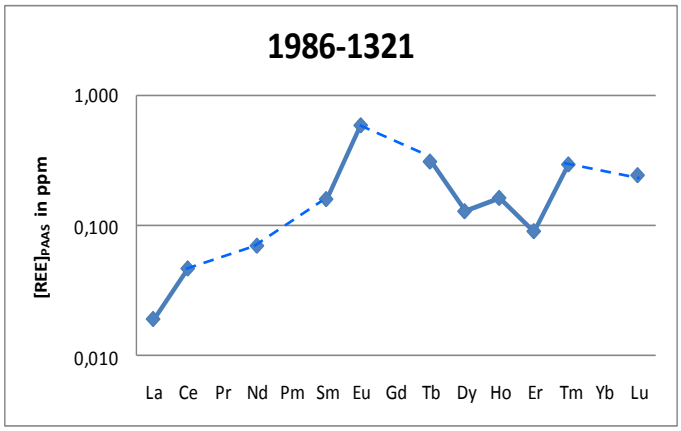

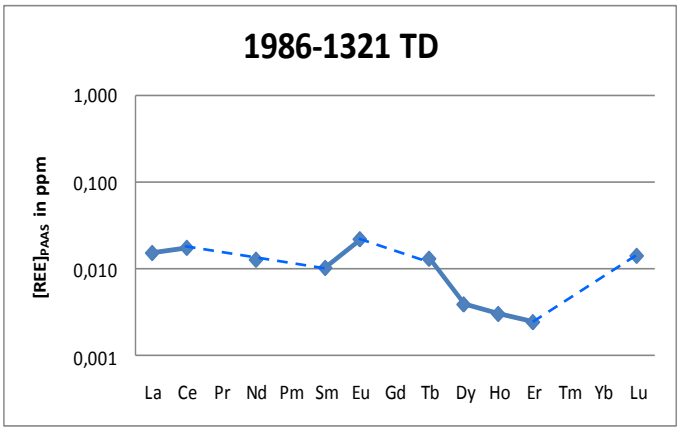

APPENDIX 8B

Chondrite normalized REE graphs for Ion Exchange Chromatography method.

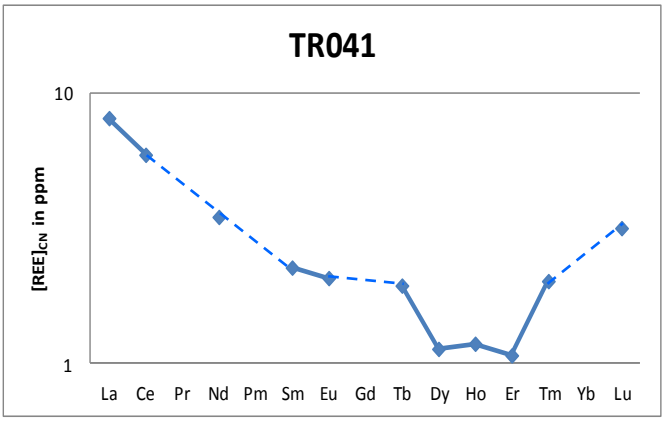

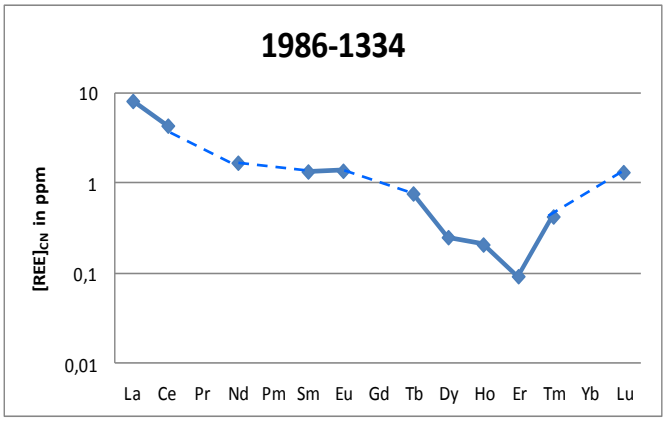

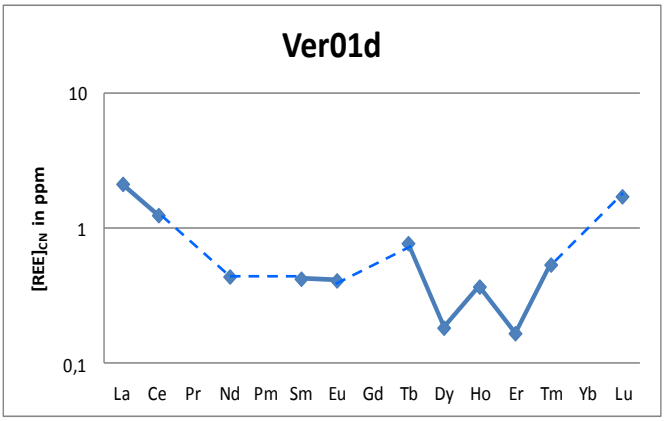

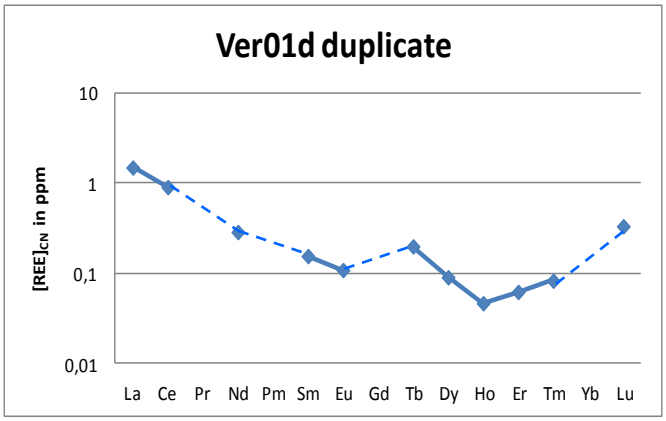

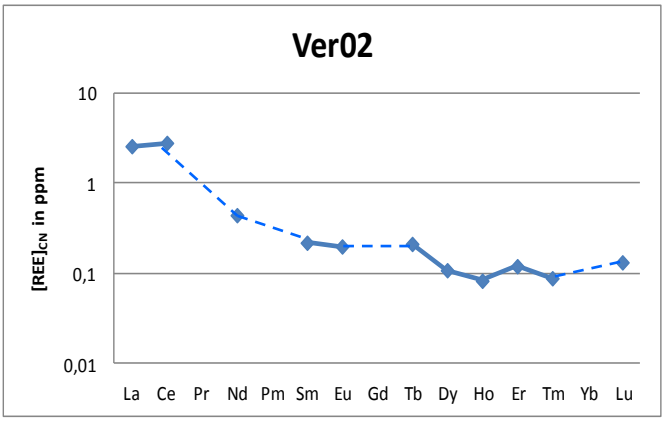

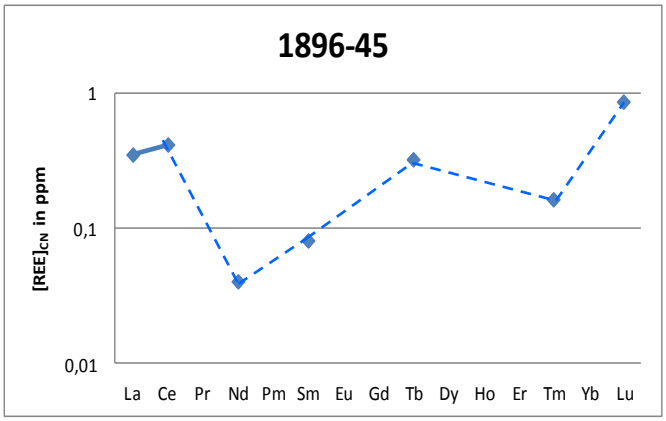

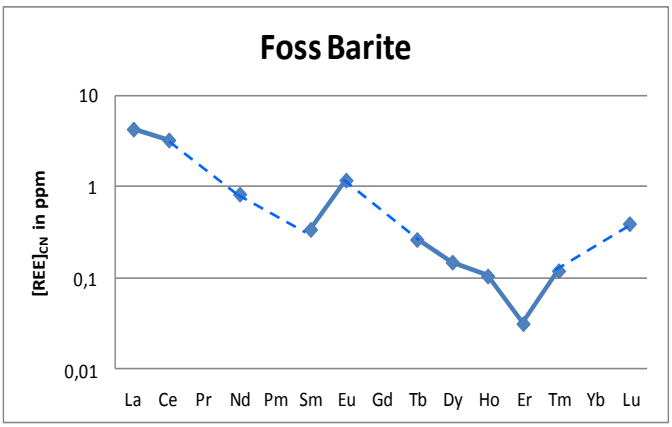

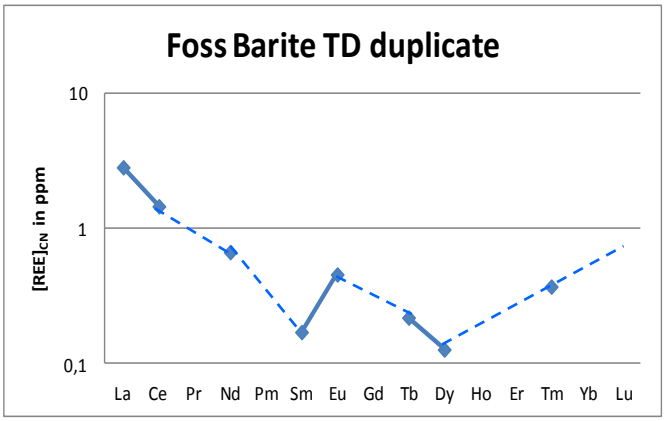

APPENDIX 8B—continued

Chondrite normalized REE graphs for Ion Exchange Chromatography method.

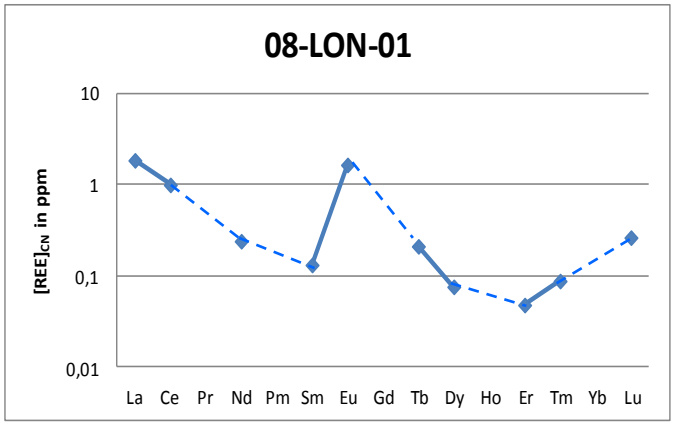

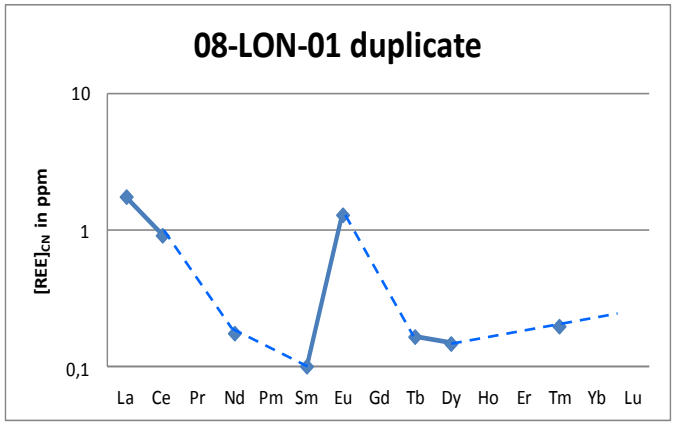

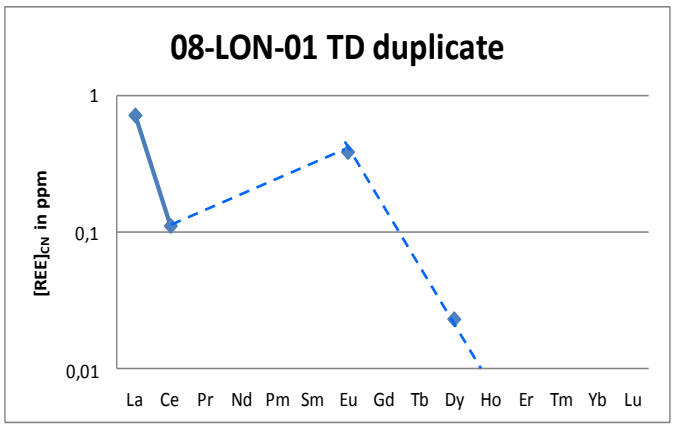

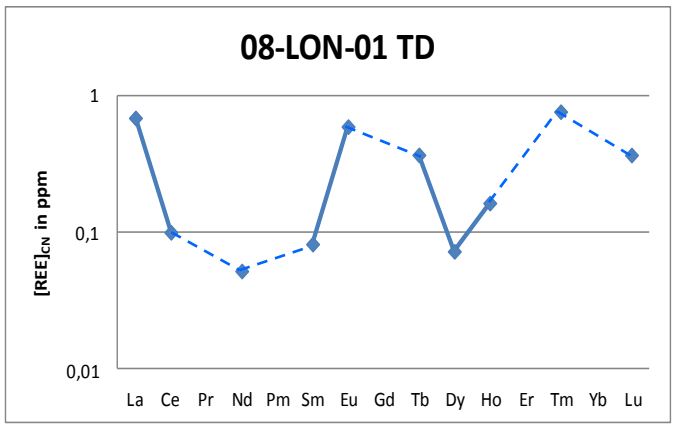

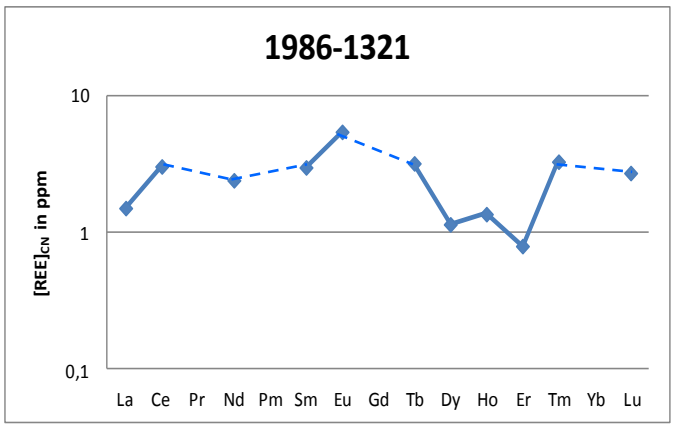

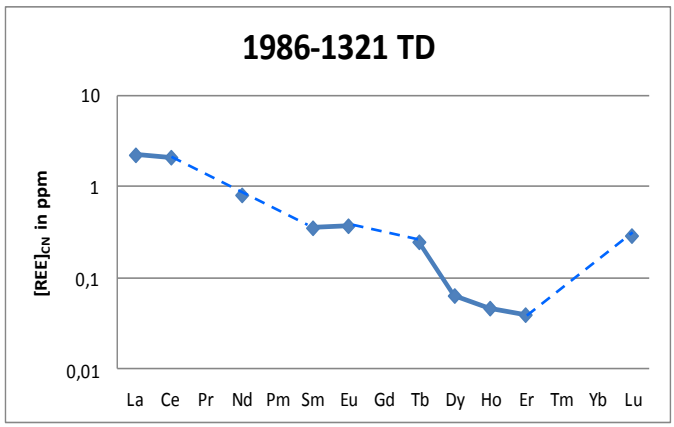

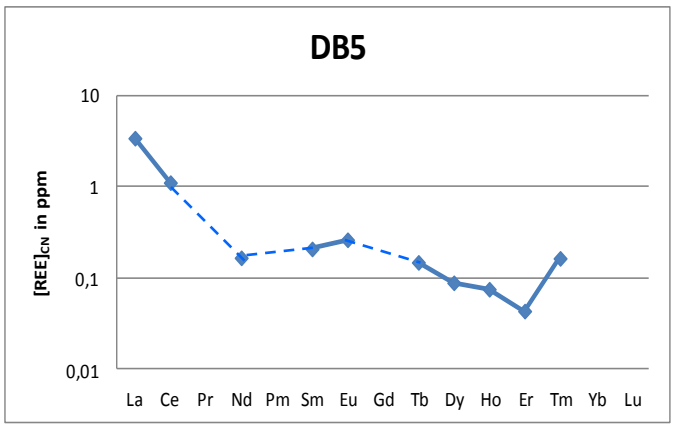

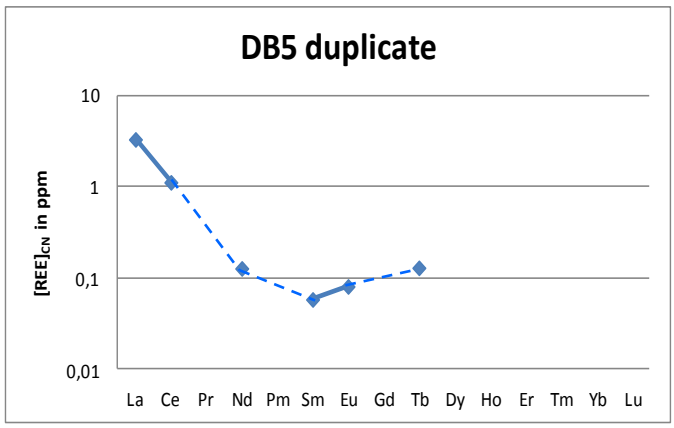

APPENDIX 8B—continued

Chondrite normalized REE graphs for Ion Exchange Chromatography method.

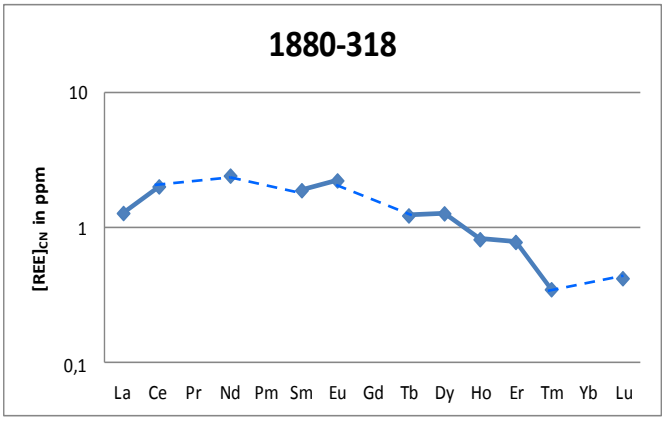

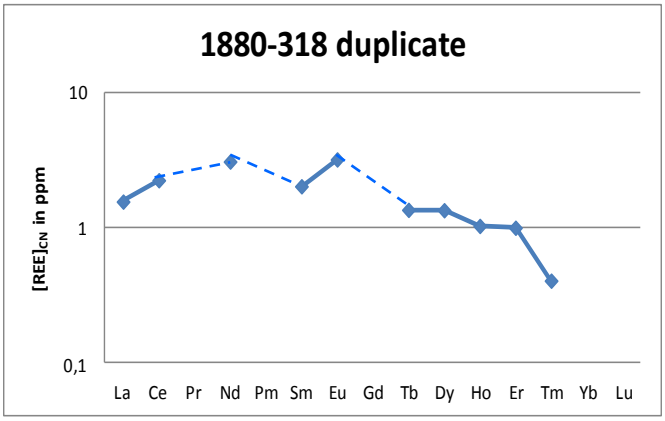

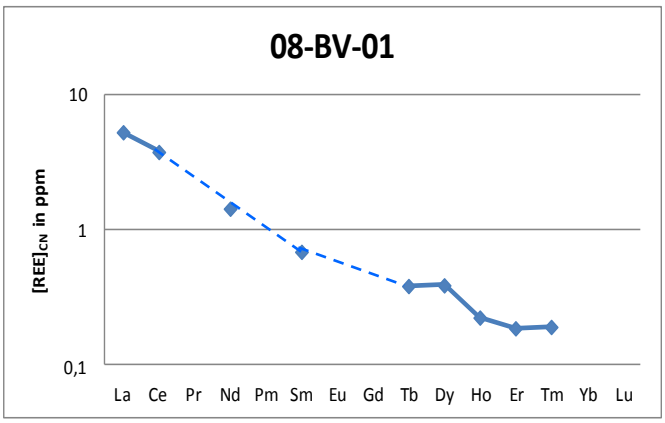

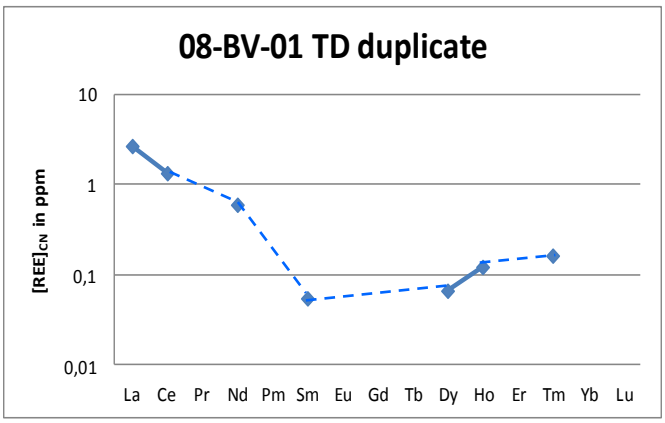

APPENDIX 9A

LA-ICP-MS and ICP-MS data combined—PAAS normalization

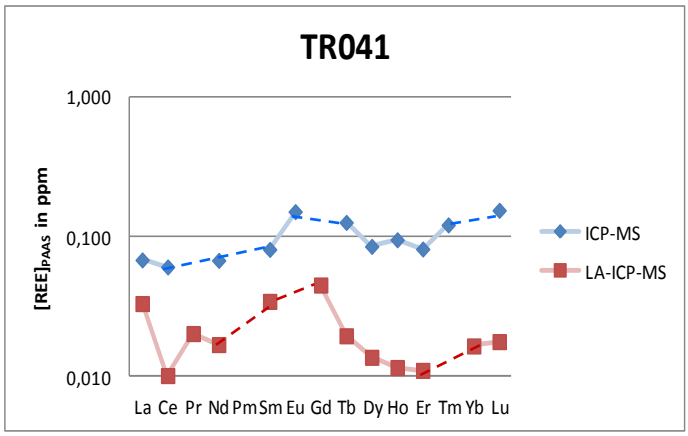

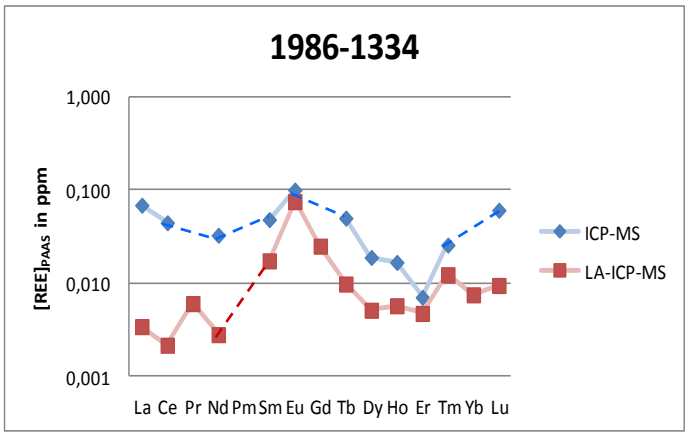

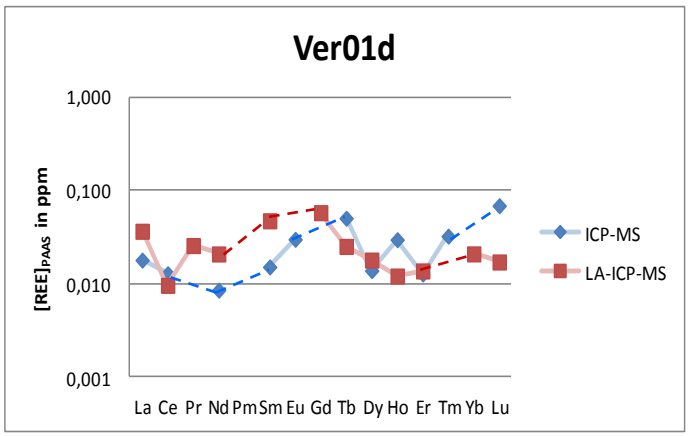

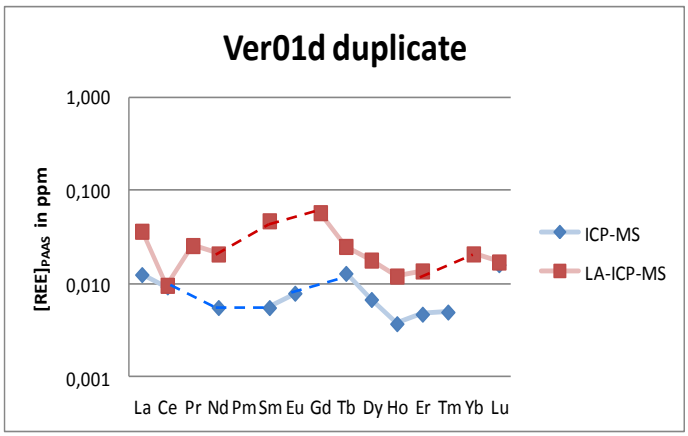

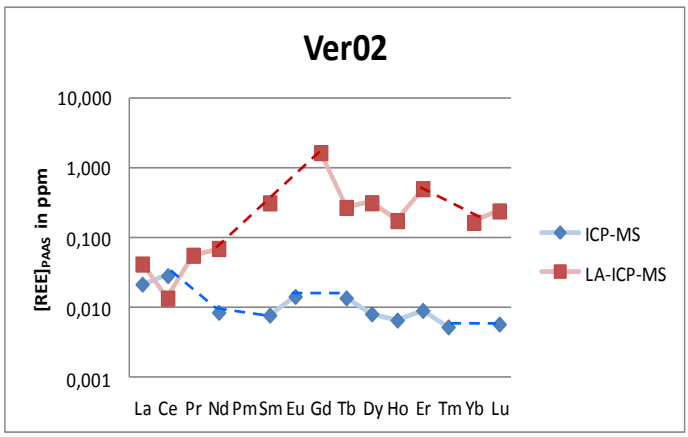

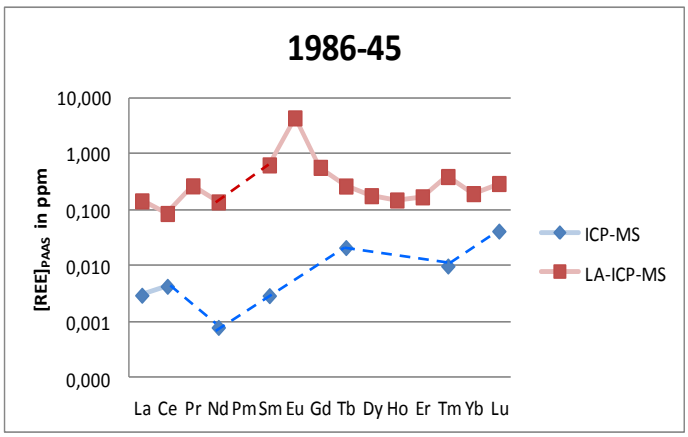

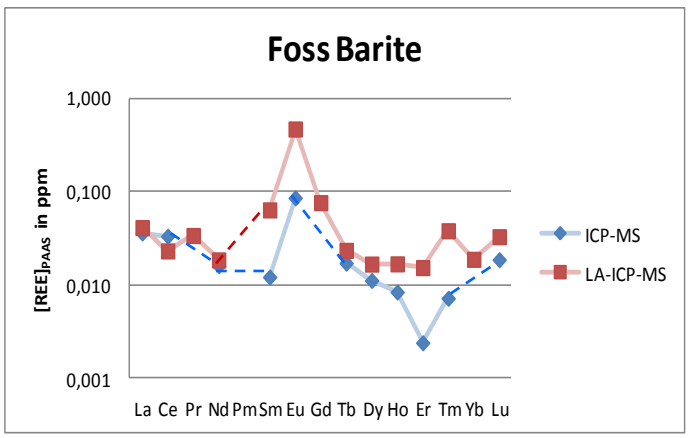

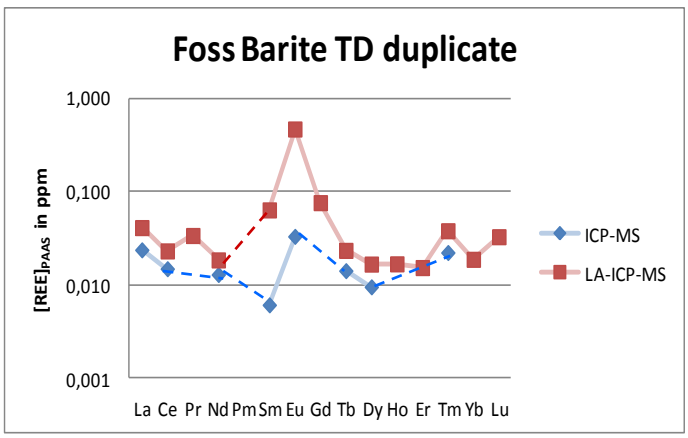

APPENDIX 9A—continued

LA-ICP-MS and ICP-MS data combined—PAAS normalization

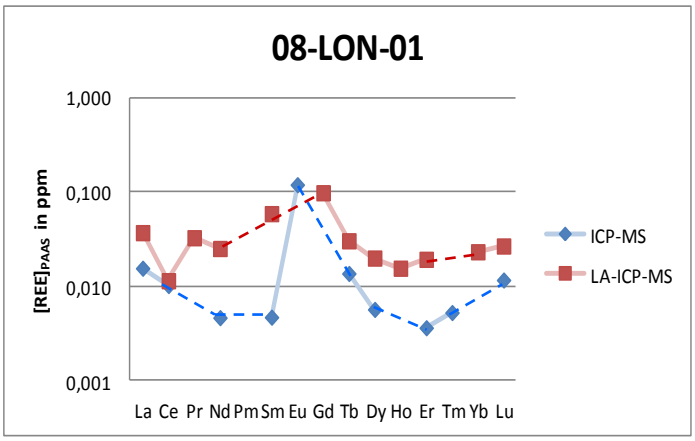

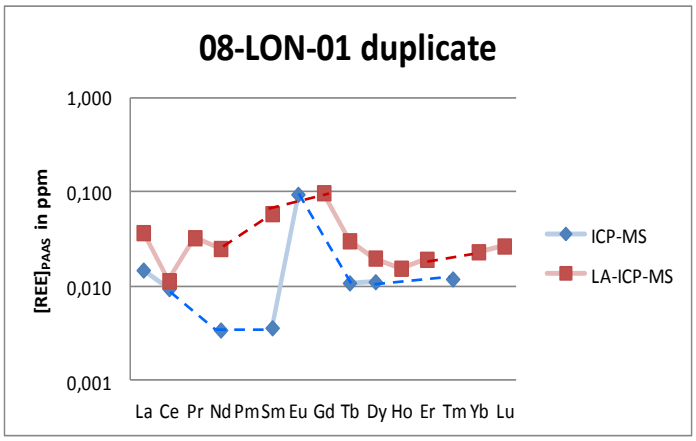

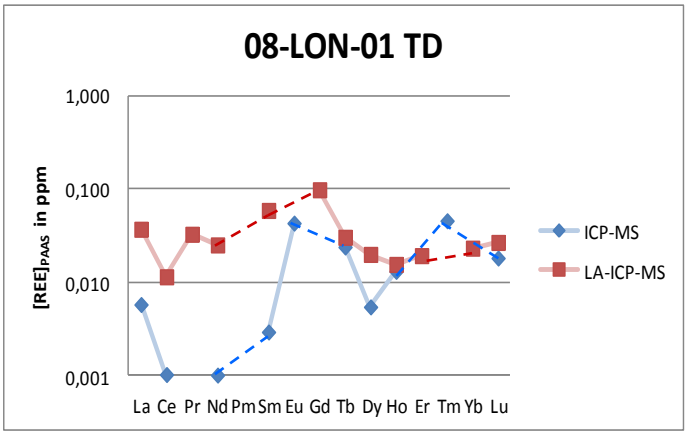

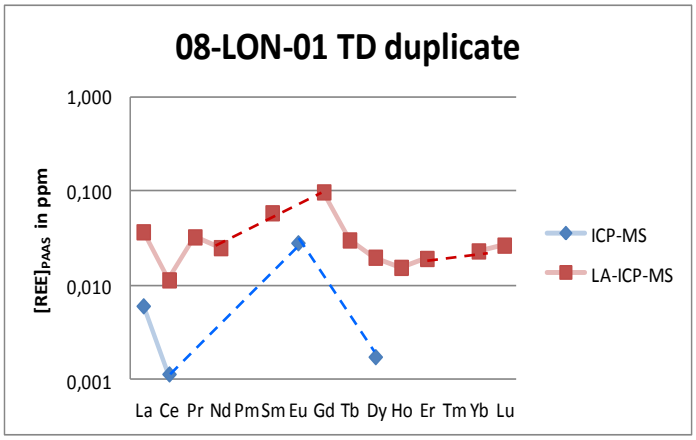

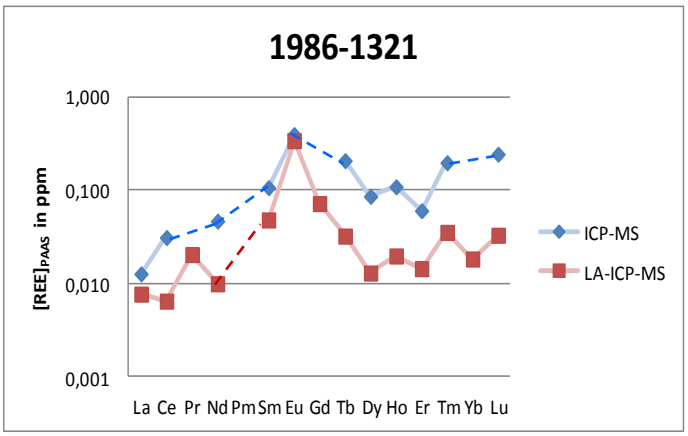

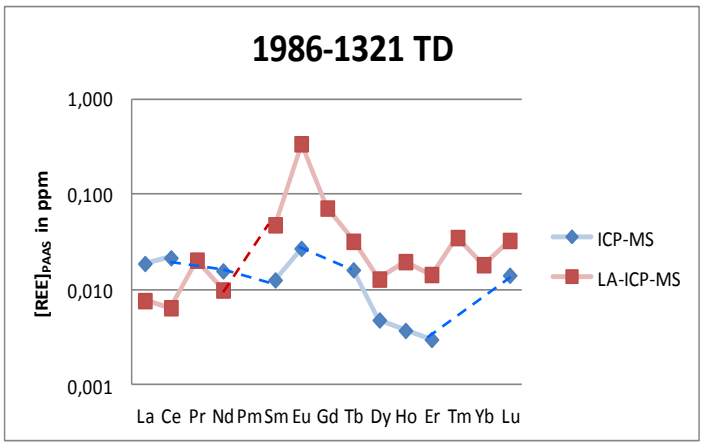

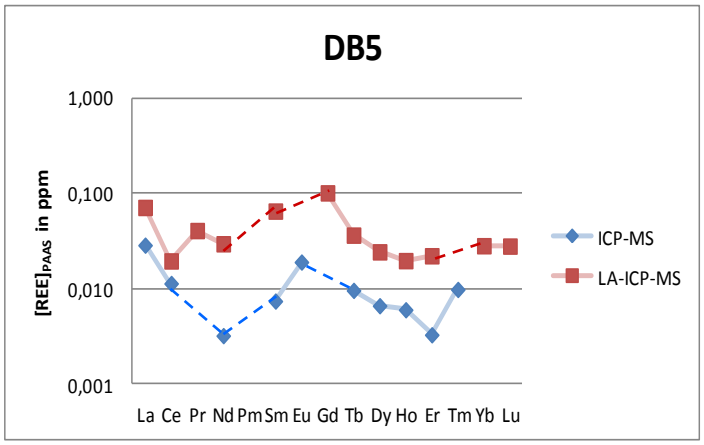

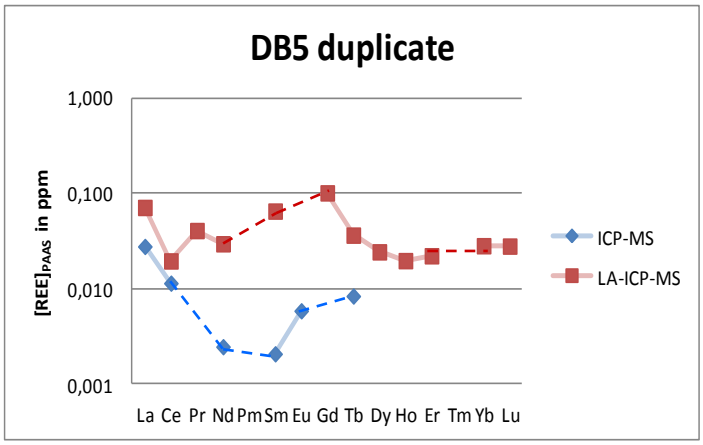

APPENDIX 9A—continued

LA-ICP-MS and ICP-MS data combined—PAAS normalization

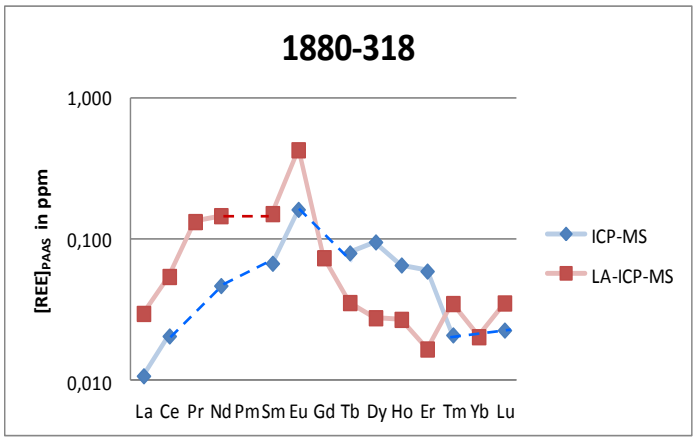

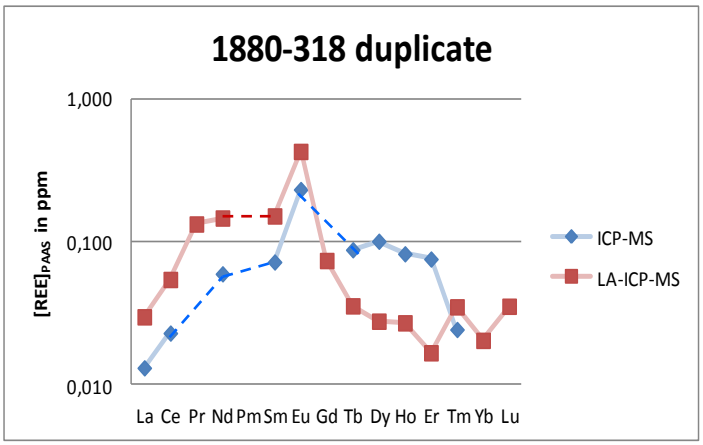

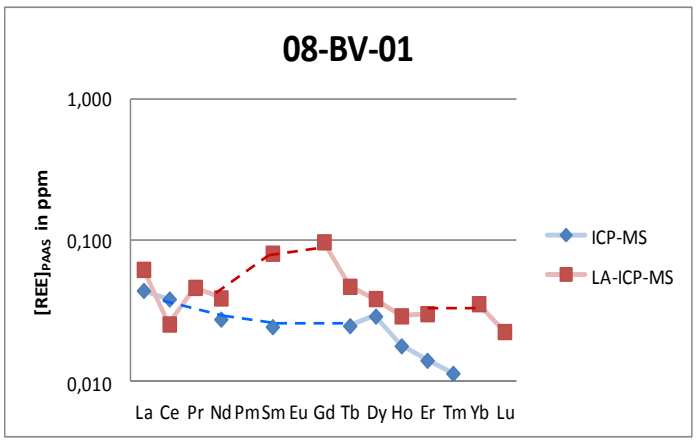

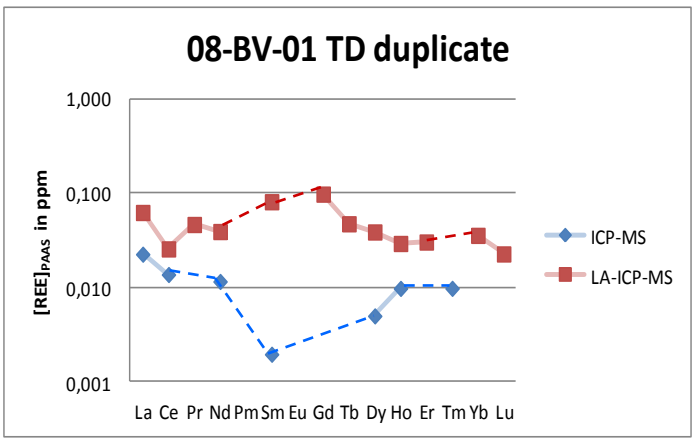

APPENDIX 9B

LA-ICP-MS and ICP-MS data combined—Chondrite normalization

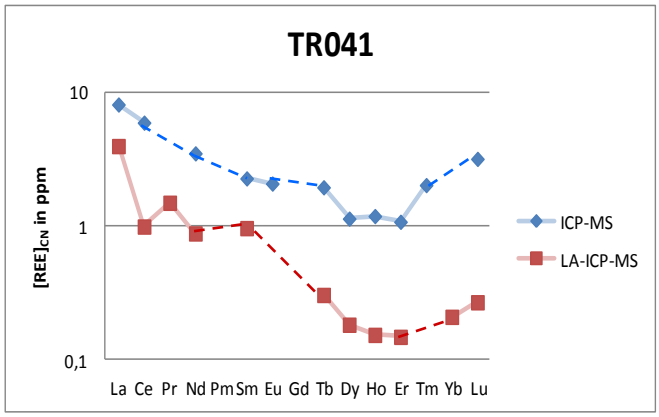

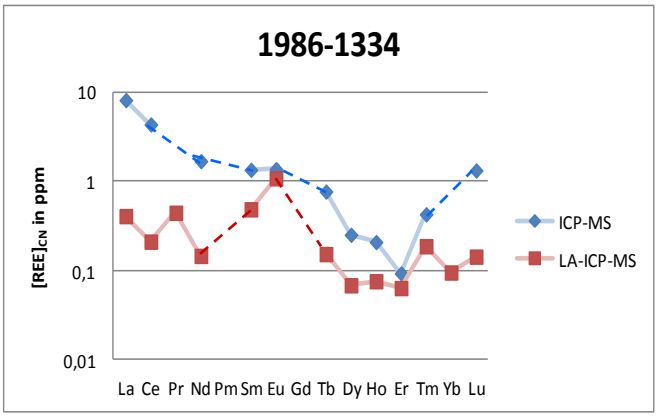

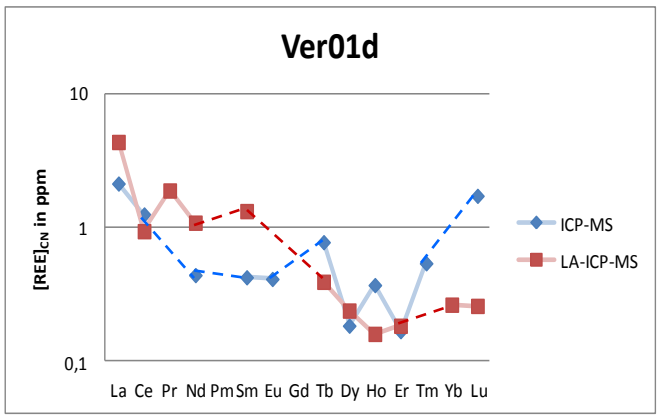

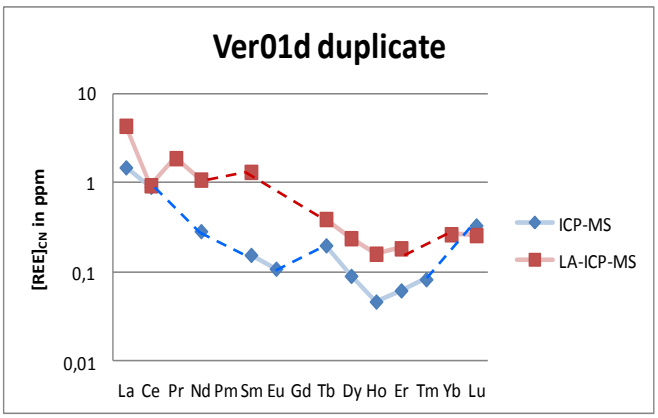

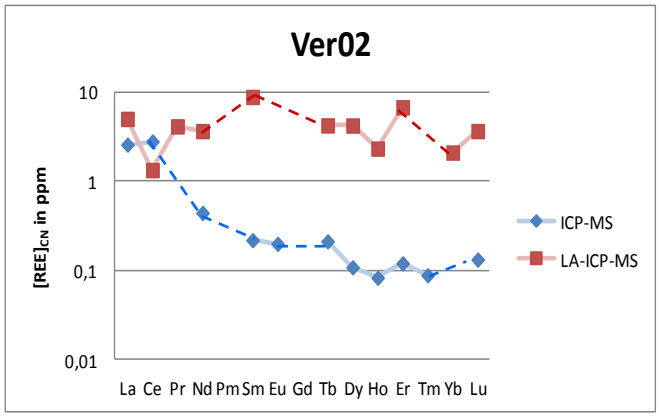

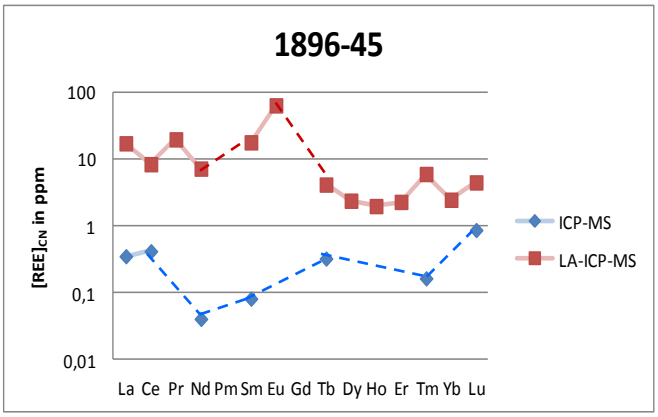

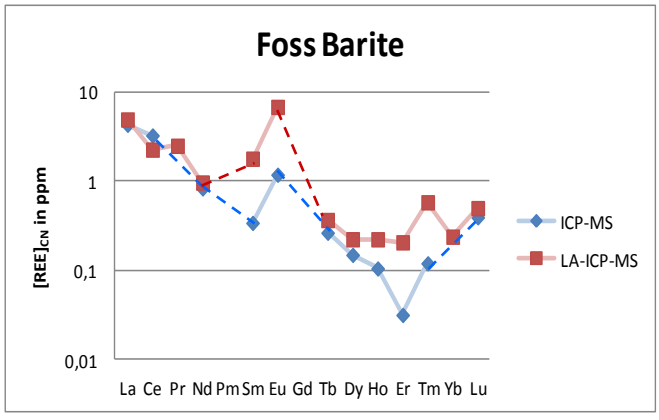

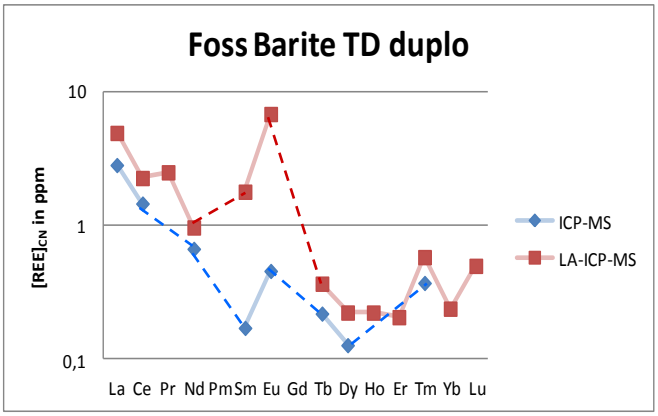

APPENDIX 9B—continued

LA-ICP-MS and ICP-MS data combined—Chondrite normalization

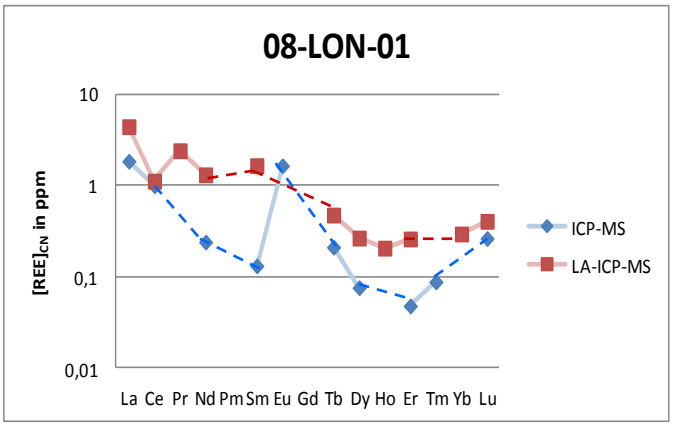

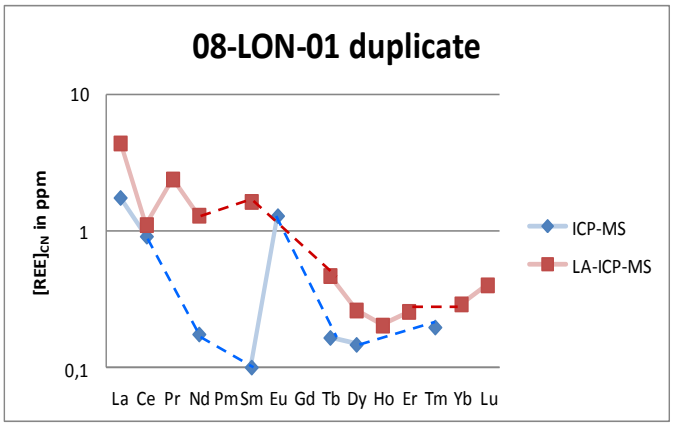

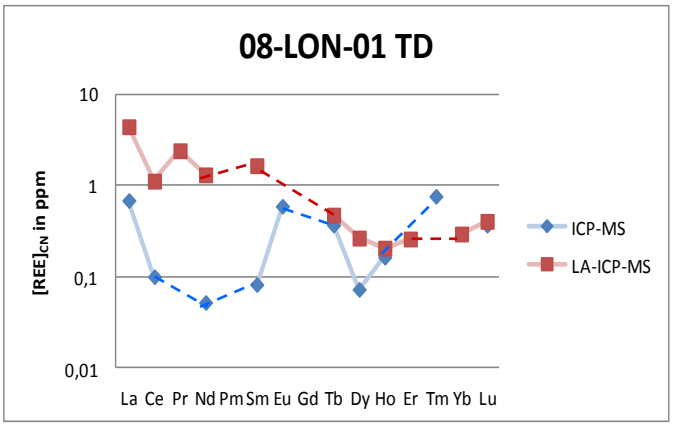

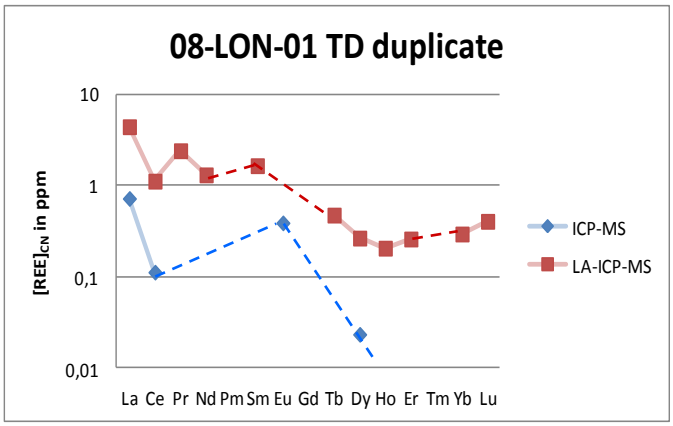

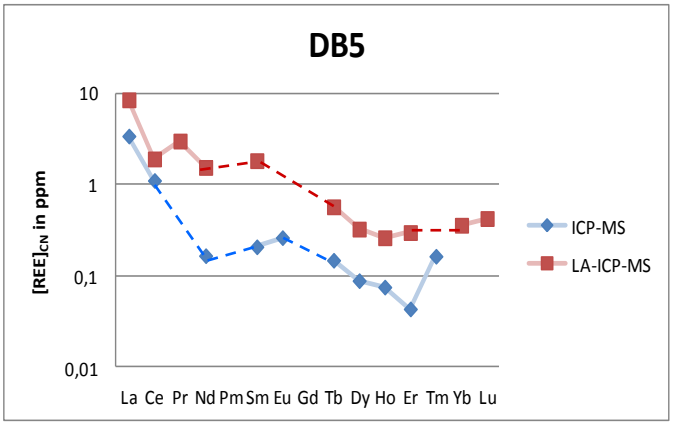

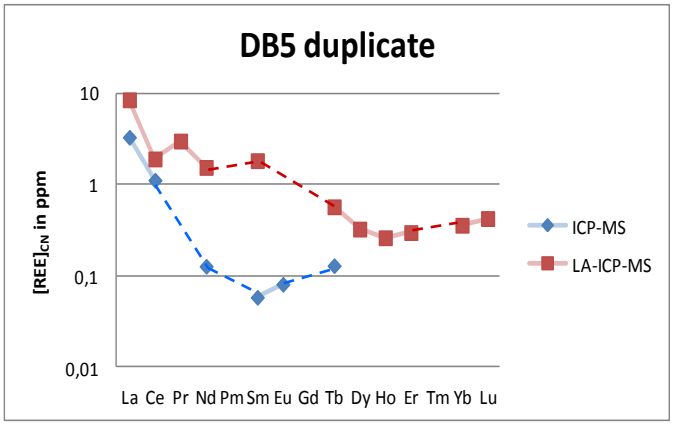

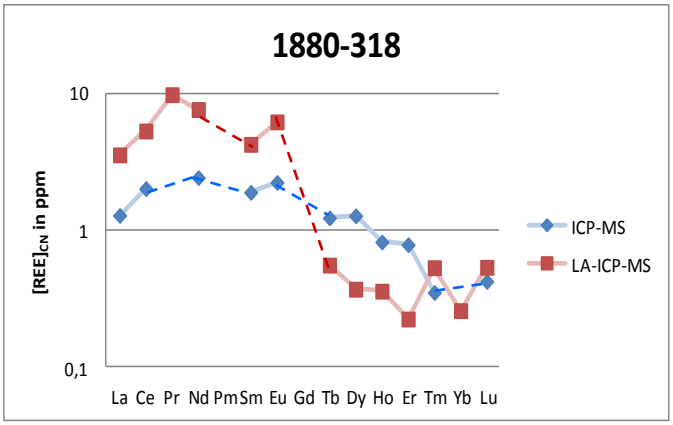

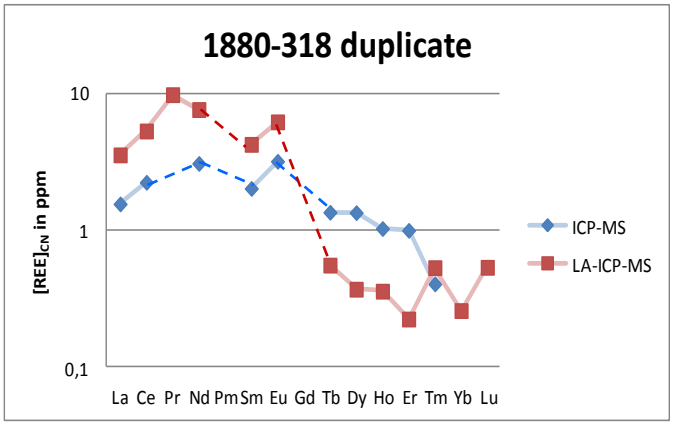

APPENDIX 9B—continued

LA-ICP-MS and ICP-MS data combined—Chondrite normalization

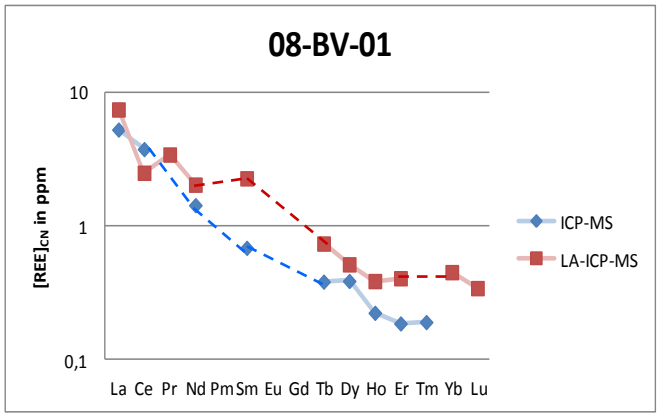

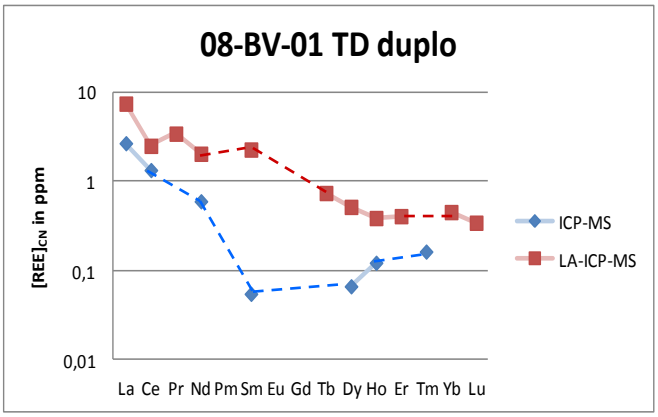

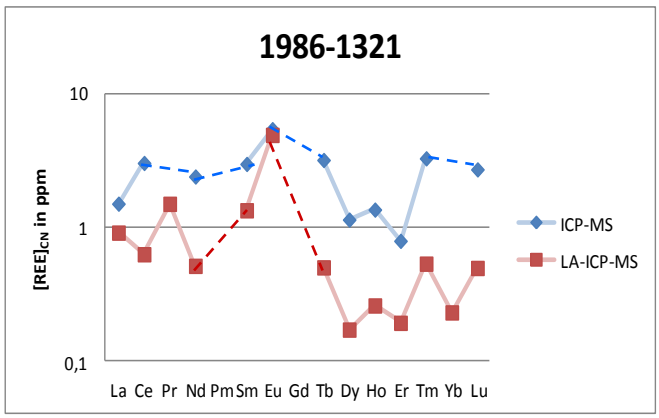

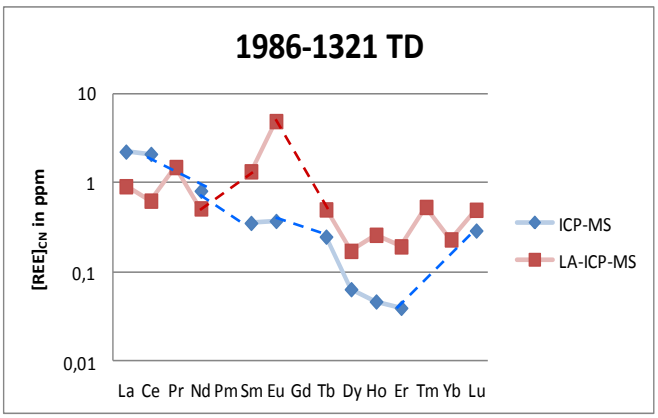

APPENDIX 10A

LA-ICP-MS vs ICP-MS graphs PAAS normalization

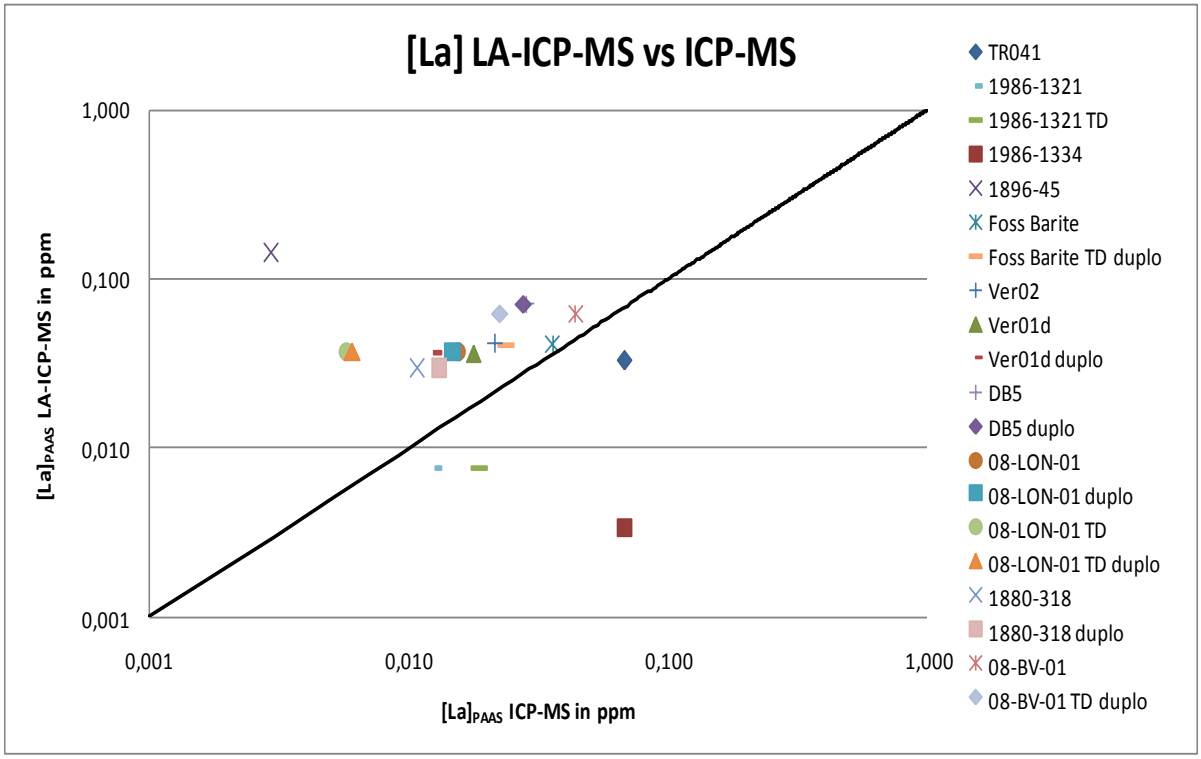

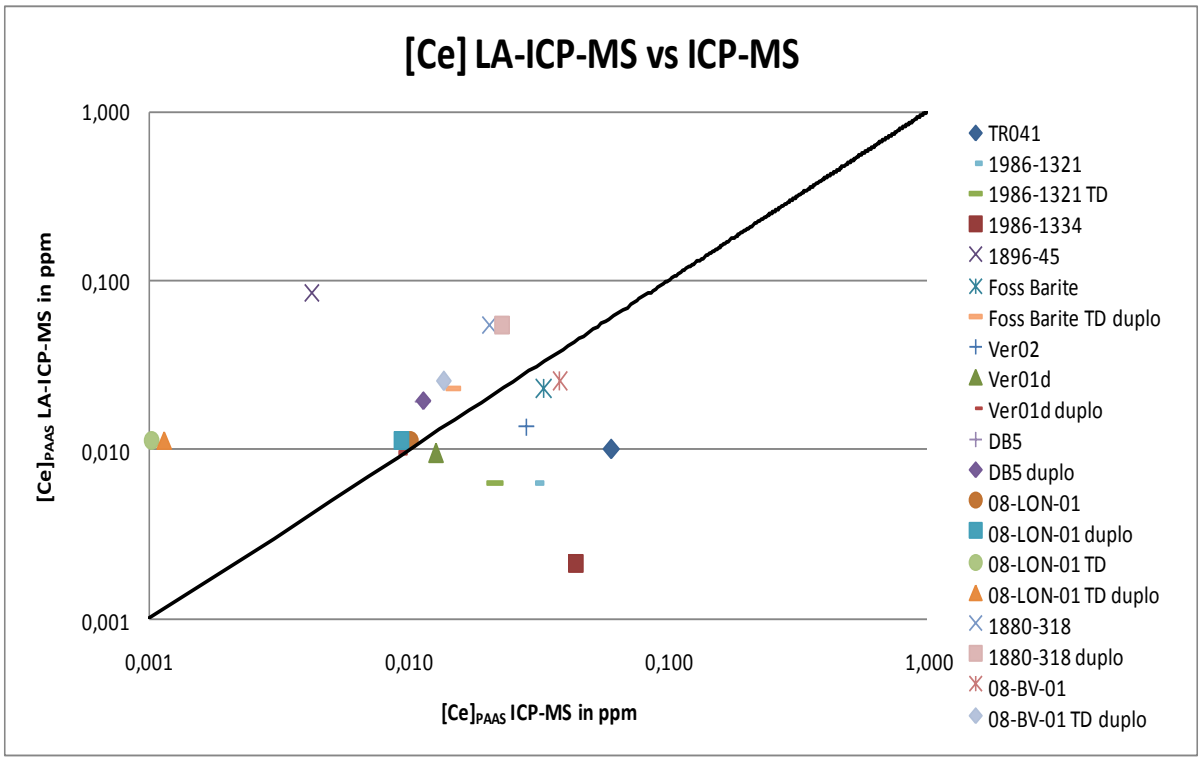

APPENDIX 10A—continued

LA-ICP-MS vs ICP-MS graphs PAAS normalization

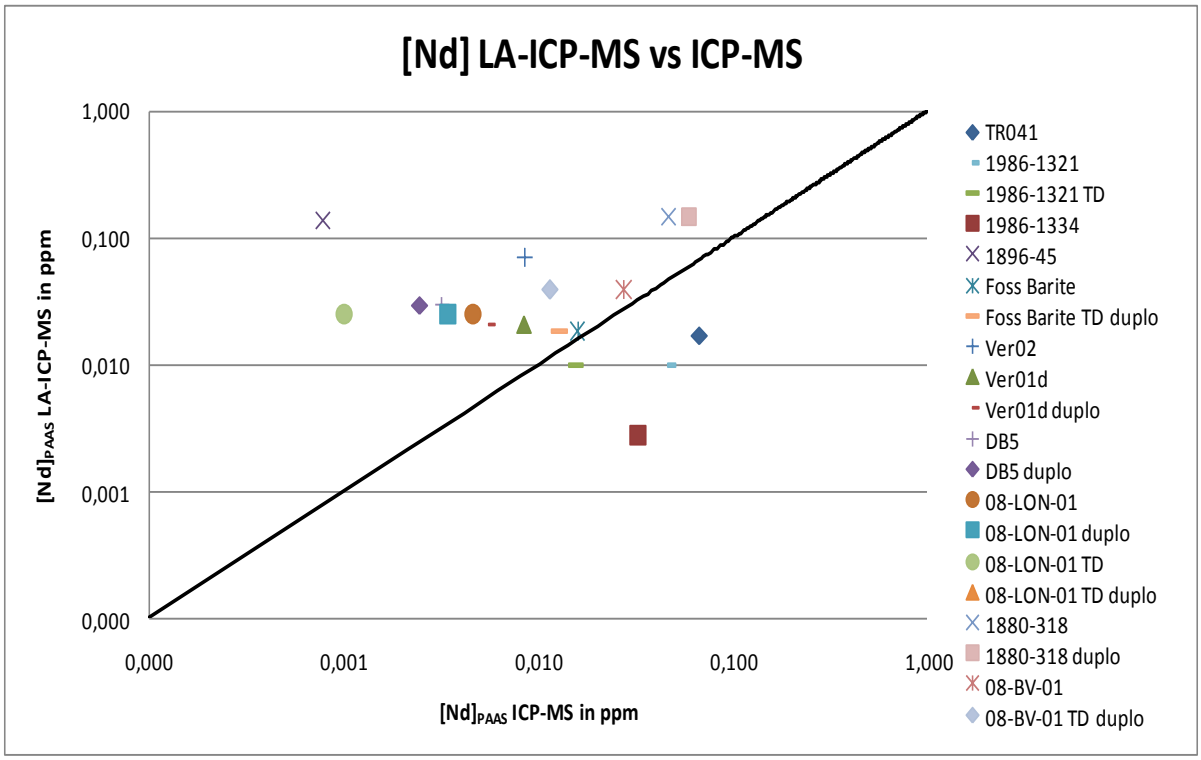

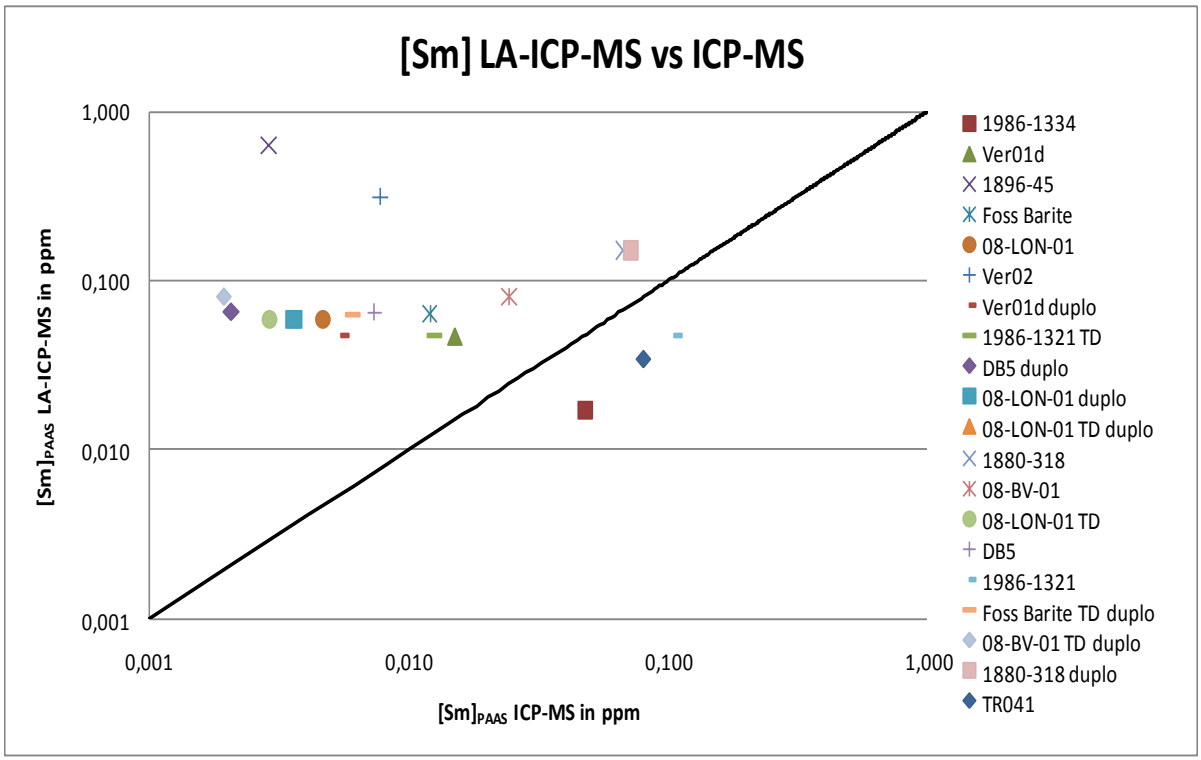

APPENDIX 10A—continued

LA-ICP-MS vs ICP-MS graphs PAAS normalization

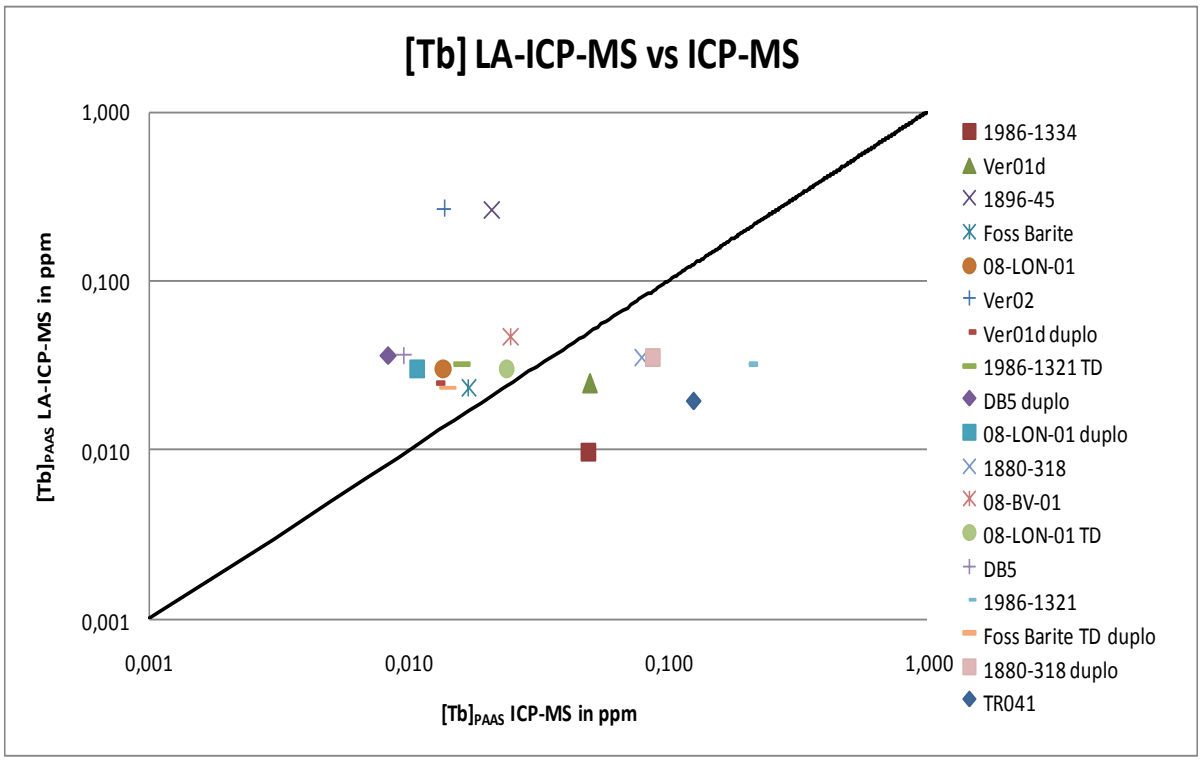

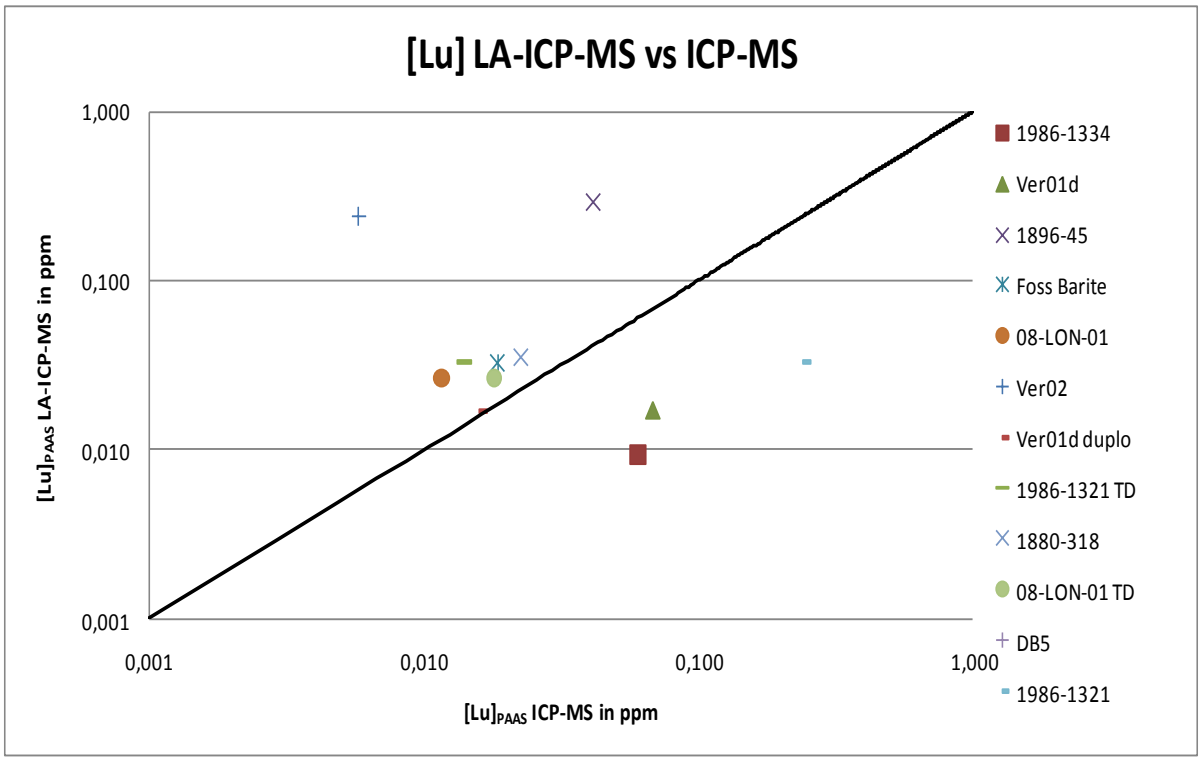

APPENDIX 10A—continued

LA-ICP-MS vs ICP-MS graphs PAAS normalization

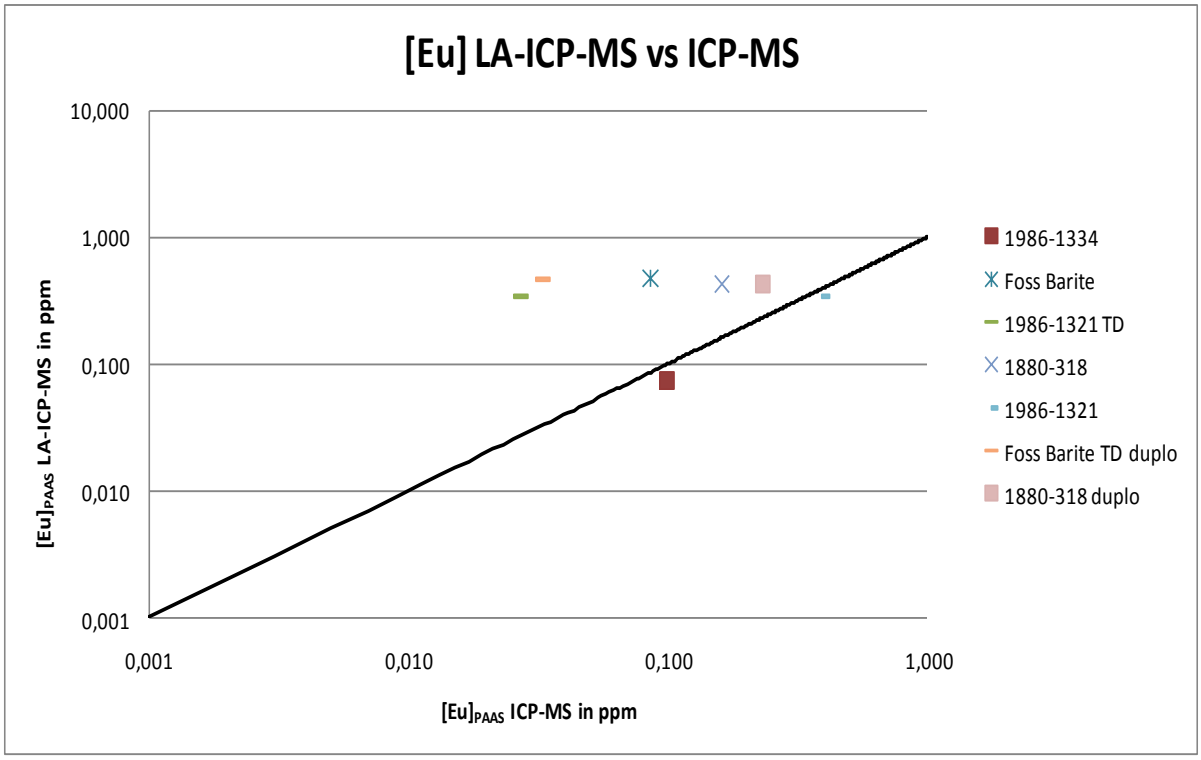

APPENDIX 11A

LA-ICP-MS REE abundance patterns—PAAS normalized

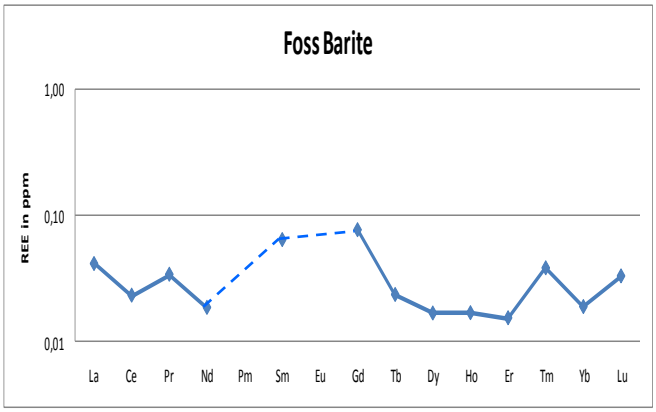

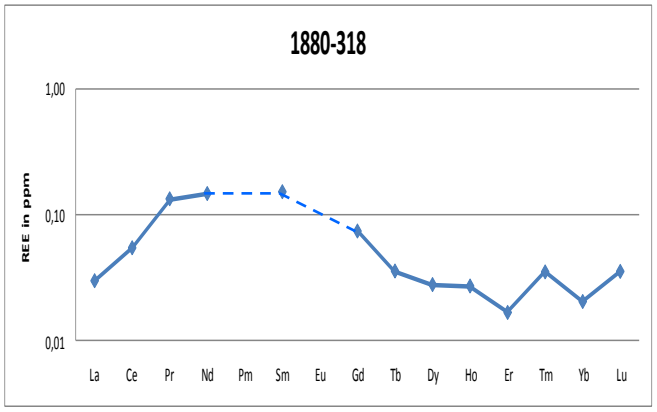

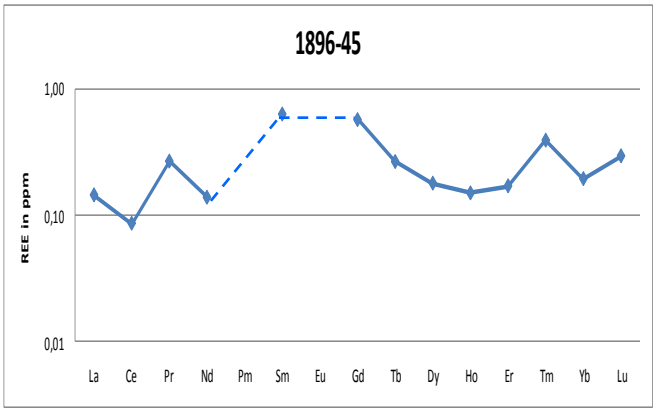

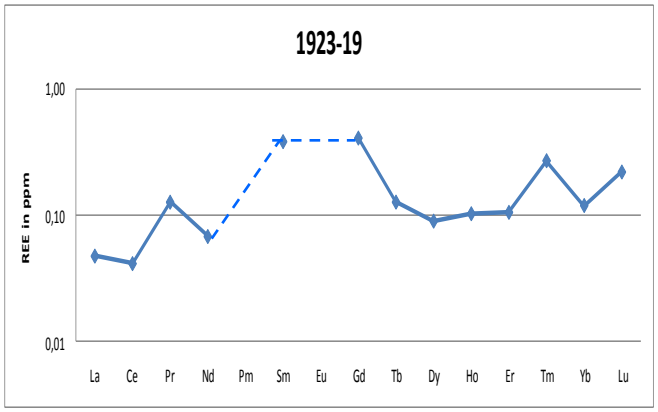

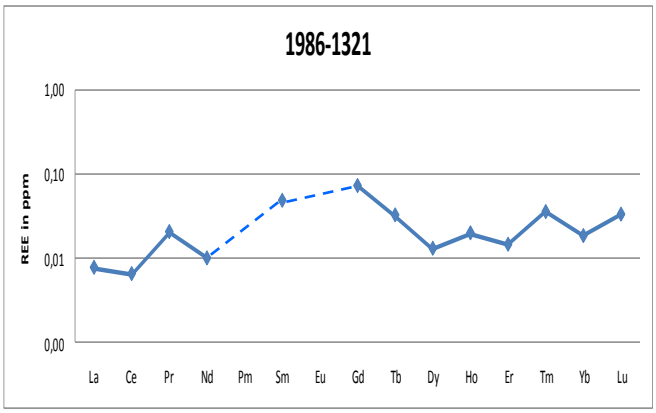

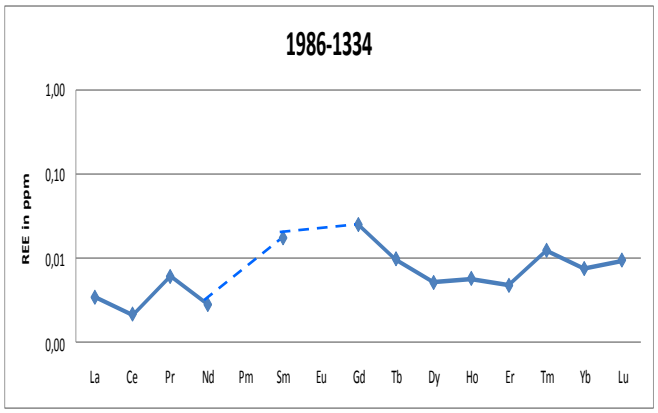

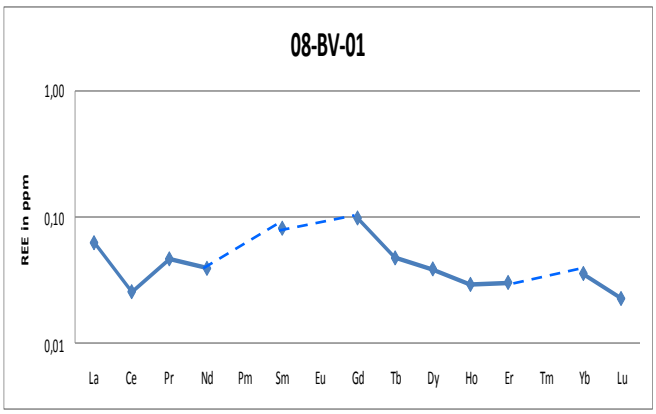

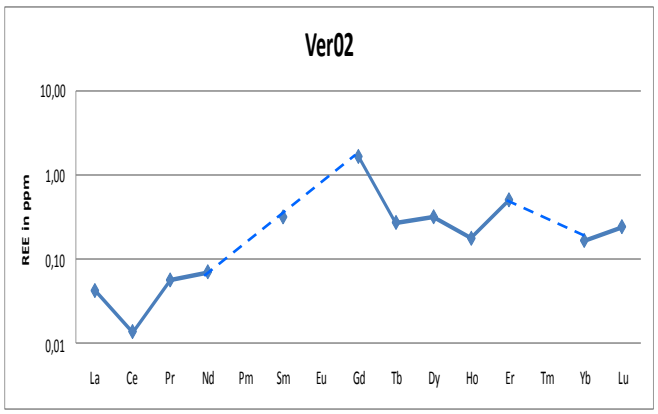

APPENDIX 11A—continued

LA-ICP-MS REE abundance patterns—PAAS normalized

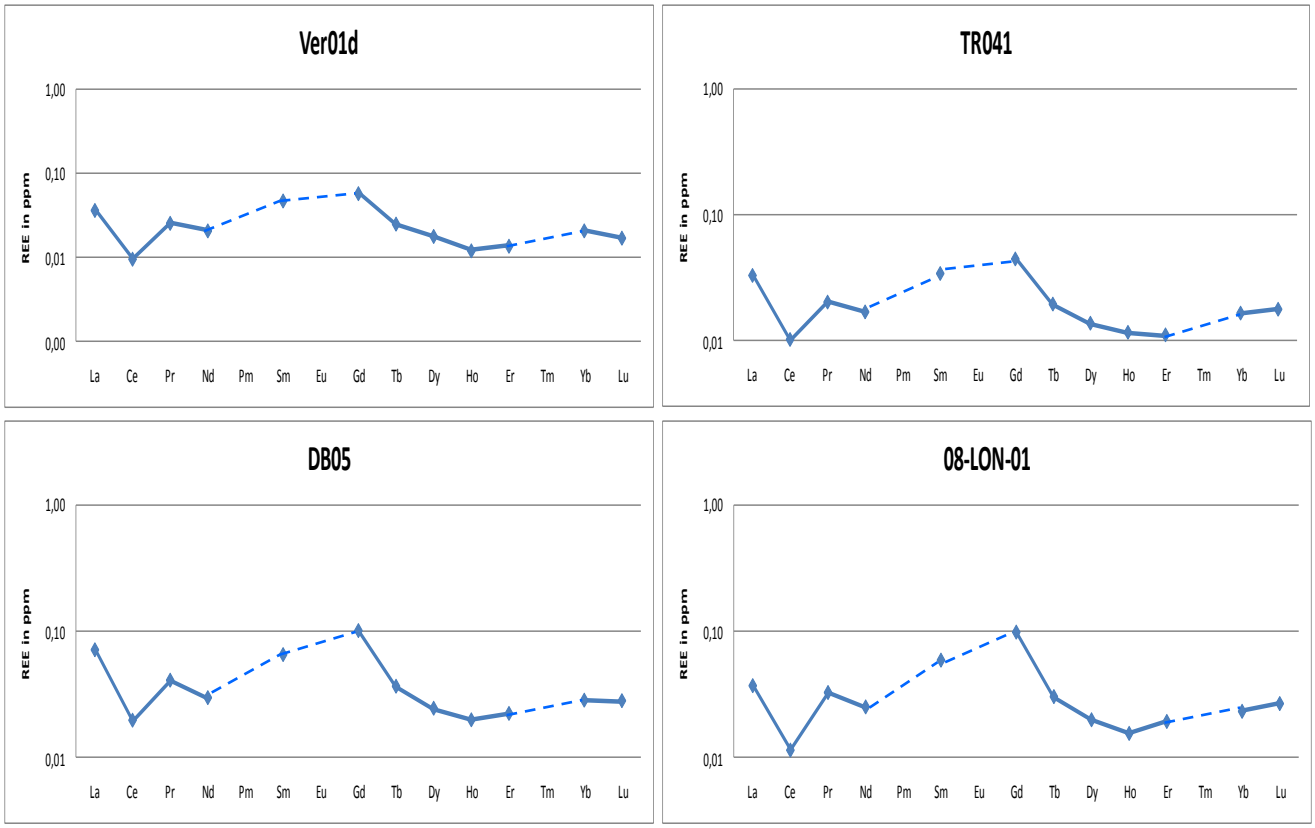

APPENDIX 11B

LA-ICP-MS REE abundance patterns—Chondrite normalized

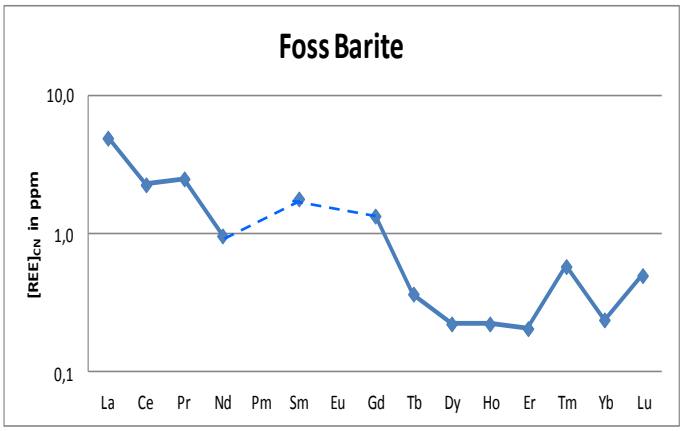

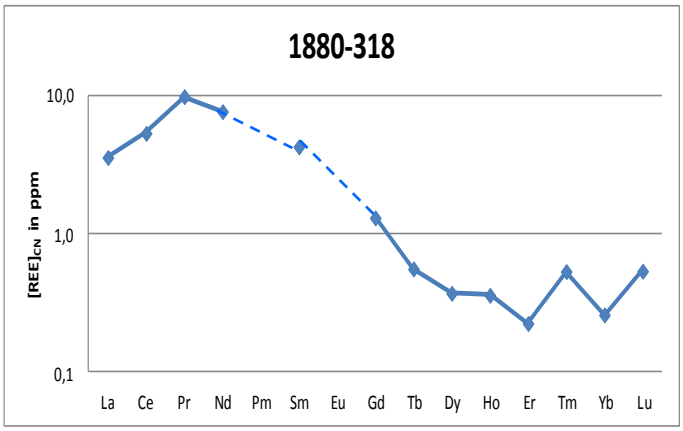

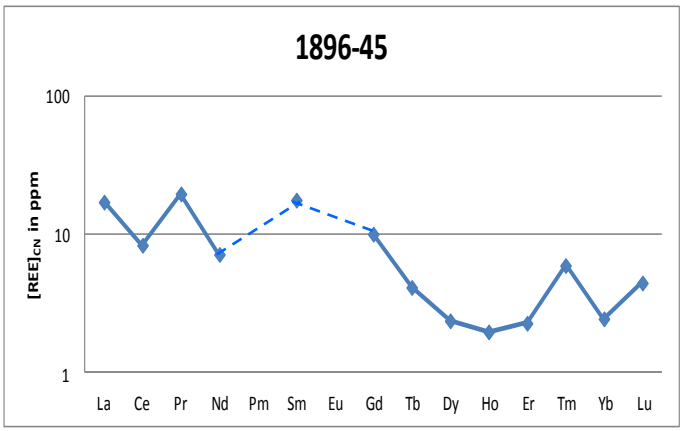

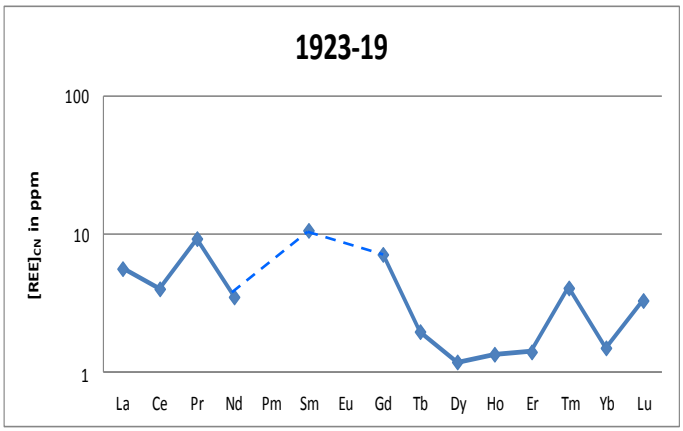

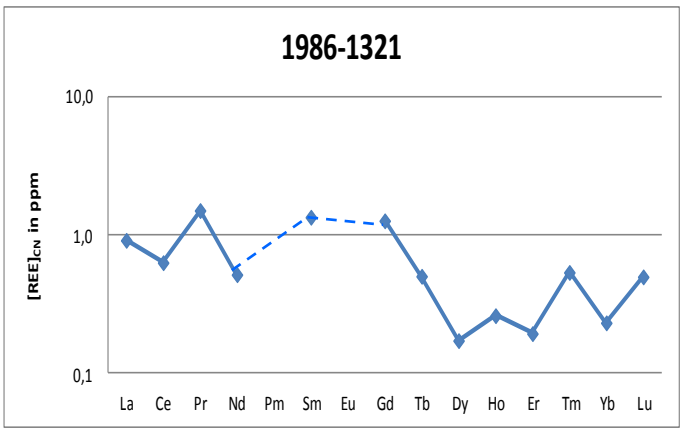

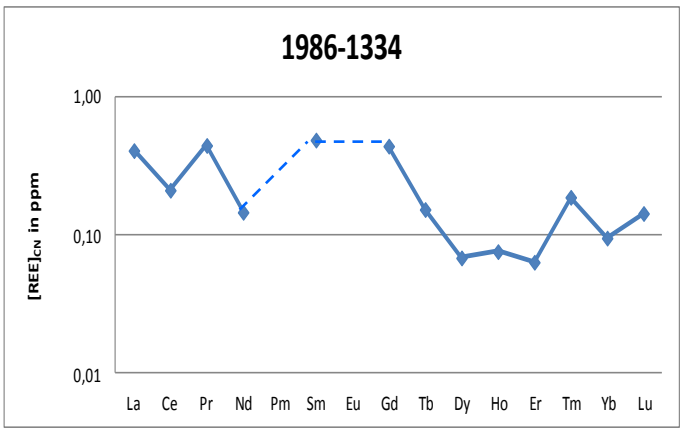

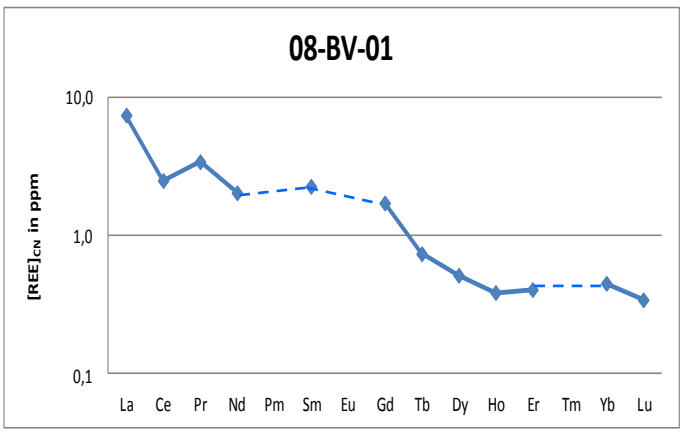

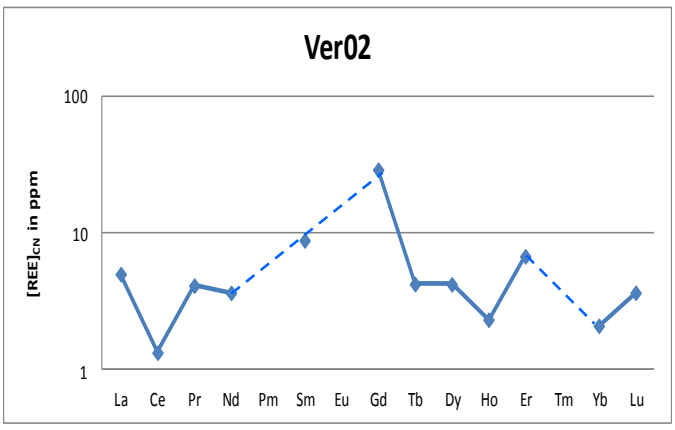

APPENDIX 11B—continued

LA-ICP-MS REE abundance patterns—Chondrite normalized